A Performance Study of a Voltage-fed Reluctance Synchronous Machine

By

ROBERT ALBERT SMITH

Submitted to the Department of Electrical Engineering in Fulfilment of the Requirements for the Magister Technologiae in Electrical Engineering at the

Cape Peninsula
University of Technology

SUPERVISOR: E. VOSS

NOVEMBER 2013

Declaration

I, ROBERT ALBERT SMITH, submit this thesis in fulfilment of the requirements for the degree of Magister Technologiae (MTech) in Electrical Engineering.

I claim that this is my own original work and that it has not been submitted in this or similar form for a degree at any other tertiary institution.

………………………………………………….
Robert Albert Smith
CANDIDATE

16 / 10 / 2013
………………………………………………….
DATE

CPUT, Cape Town Campus
………………………………………………….
PLACE

Acknowledgements

I wish to express my gratitude to those who I believe have assisted me getting to this point in my academic career and therefore with my thesis.

My Heavenly Father

Jesus Christ, without You none of this would have been possible and I thank You for Your guidance, support and endless love You have given me throughout these years.

Mr. Egon Voss

Thank you for your help and supervision throughout the whole research process. I appreciate all the time and effort you put aside for me and all the assistance you have given me. You are an inspiration to many at this institution.

Alstom: SLIM Electromagnetic Engineering

Jonathan and Mark, thank you for all the help and support you have given me. I have gained a great deal of valuable knowledge from you and am truly grateful for that.

CPUT and Centre for Postgraduate Studies

Thank you for the financial support, which gave me the opportunity to achieve my goal.

My university friends

Thanks to my fellow MTech students, Deon, Albertu and Graeme as well as my friends in the heavy current lab, Bernd, Ben and Garret. Your assistance, guidance and support added so much value to this journey.

My family and friends

Thanks to my loving parents for giving me the opportunity of obtaining a tertiary education, doing what I love most, as well as my friends, Dario, Hanrí and Rochelle. Your love, support and belief in me has made all of this possible.

Synopsis

The reluctance synchronous machine (RSM) operates on the principle of magnetic reluctance, which is produced through a careful selection of rotor flux barriers and cut-outs. Magnetic reluctivity is the resistance to magnetic flux and can be directly related to the principles of Ohm's law in electrical circuits.

Although reluctance motors have been known for more than 150 years, researchers lost interest when Nikola Tesla's induction machine (IM) was introduced to industry. Over the last few decades, however, RSMs have shown a lot of potential. They are cheap, robust, reliable, and their rotors can also be used in the stators of IMs. The disadvantage of these machines is an inherently high torque ripple, being the result of its rotor geometry, but the biggest advantage is having a significant reduction in copper losses after the rotor cage has been removed. This advantage drove engineers to investigate, optimise and modify the performance and structure of this machine, which led to the usage of electronic drive systems.

The recent advances in technology have allowed researchers to further investigate and modify the design and performance of this special type of machine, with the integration of Finite Element Analysis (FEA) software also making a contribution to the development of the RSM's current driven systems.

The voltage-fed RSM, driven direct-on-line (DOL) from the utility supply, was left in the shadows as the current-fed RSM took reign, but still is, in the author's opinion, not yet fully analysed. This thesis practically investigates the performance characteristics of the cageless, voltage-fed 3kW RSM in its steady-state operation, under various loads. These performance characteristics are also compared to a RSM driven from a sensorless vector drive (current-fed) to investigate the advantages and disadvantages between the two.

Experiments performed on the test bench immediately reveal a limitation to the voltage-fed RSM's ability to drive higher loads. While the current-fed RSM conveniently reaches 150% of its full-load, the voltage-fed RSM, due to its cageless

structure, only reaches 110% of its full-load power. Despite this discovery, the voltage-fed RSM proves to have a lower core loss, harmonic content and torque ripple. Using a FE software package with an integrated source-code, additional parameters such as the dq-axis inductances and currents are also compared and analysed in terms of its reaction to an increase in load. The eddy-current, hysteresis and excess losses are also analysed as well as the harmonic components caused by the geometry of the RSM.

For academic purposes, a fair amount of emphasis is placed on the approach to the problem. The preparation for the FE simulation is explained in detail, providing insight into the FE mathematical model as well as parameter acquisition. These parameters include current angle, friction and windage losses, stator resistance, end-winding leakage reactance, core loss and inertia. The results obtained by the FE model are compared to that of the measured results and is found to have an error of only 0.52%. Furthermore, this study attempts to find the feasibility of the voltage-fed RSM's practicality in modern-day industry. The conclusion is drawn that the voltage-fed RSM could be used as a more elegant alternative to an otherwise over-complicated and over-priced installation.

Table of Contents

List of Figures and Tables

Figure	Title	Page

List of Symbols and Abbreviations

Roman alphabet

$\vec{A}$	magnetic vector potential (Wb/m)
$\vec{A}_{avg}$	average magnetic vector potential in a slot (Wb/m)
$\vec{A}_{mi}$	magnetic vector potential of node i at element m (Wb/m)
$\bar{a}_s$	slot area (m^2)
A_{cu}	total active copper area in stator slots (m^2)
$\bar{a}_r$	rotor area (m^2)
A_z	magnetic vector potential in the z-plane (Wb/m)
$\vec{B}$	magnetic flux density (T)
c	winding coil-pitch
d_i	stator inner diameter (m)
d_o	stator outer diameter (m)
E	induced emf across stator windings (V)
$\vec{E}$	electric field strength (V/m)
e_{abc}	instantaneous induced emf's in phases a, b, and c
F_{po}	pull-out torque factor
$\vec{H}$	magnetic field strength (A/m)
i	node number
i_{dq}	instantaneous values of the d- and q-component currents (A)
i_{abc}	instantaneous phase currents for a, b, and c (A)
I_0	no-load current (A)
I_s	current space phasor (A)
J	moment of inertia (kgm^2)
$\vec{J}$	current density (A/m^2)
k_d	winding distribution factor

k_e	end-winding distribution factor
k_p	winding pitch factor
$[K]$	Park's transformation matrix
l	total active stator conductor length (m)
L_d	d-axis inductance (H)
L_e	end-winding leakage inductance (H)
l_e	average end-winding conductor length (m)
l_s	axial stator stack length (m)
L_q	q-axis inductance (H)
M	number of elements in one slot
m	number of phases
m_e	element number
n_a	number of parallel circuits per stator winding
N_{ijk}	magnetic vector potential shape functions in the i-, j- and k-plane
p	number of pole pairs
P	number of poles
P_c	core losses (W)
P_{cu}	copper/winding losses (W)
P_{fw}	friction and windage losses (W)
P_{in}	input power (W)
P_{out}	output power (W)
q	amount of coils per pole phase group
R_c	core loss resistance (Ω)
r_{mi}	radius from centre of shaft to node i at element m (m)
R_s	stator resistance per phase (Ω)
R_a	total stator resistance (Ω)

T_{avg}	average torque (Nm)
T_d	developed (electrical) torque (Nm)
T_{max}	maximum torque (Nm)
T_{min}	minimum torque (Nm)
T_{po}	pull-out torque (Nm)
T_r	reaction torque (Nm)
T_{rip}	percentage torque ripple (%)
v_{abc}	instantaneous stator voltages for phases a, b, and c (V)
V_{abc}	a, b, and c phase fundamental stator voltages (V)
V_d	d-axis fundamental stator voltage component (V)
V_q	q-axis fundamental stator voltage component (V)
V_{dq}	d and q-axis fundamental stator voltage components (V)
W	number of turns in series per phase
x_d	d-axis reactance (Ω)
x_q	q-axis reactance (Ω)
z	number of conductors per slot

Greek alphabet

α	$1\angle 120°$ or e^{j120}
α_t	temperature co-efficient
Γ	contour of integration (m)
Δ_m	area of element (m^2)
γ	torque angle (°)
θ	rotor angle between d-axis and a phase
$\bar{\lambda}_{abc}$	a, b, and c phase fundamental stator flux linkages (Wb)
$\bar{\lambda}_d$	d-axis fundamental stator flux linkage component (Wb)

$\bar{\lambda}_q$	q-axis fundamental stator flux linkage component (Wb)
$\bar{\lambda}_{dq}$	d and q-axis fundamental stator flux linkage components (Wb)
$\bar{\lambda}_s$	flux linkage space phasor (Wb)
ϑ	current angle (°)
μ	permeability (Wb/Am)
μ_0	permeability of air (Wb/Am)
σ	electrical conductivity (A/Vm)
τ	saliency ratio, L_d/L_q
υ	i_d/i_q ratio
ω	reference frame rotating speed (deg/s)
ω_e	electrical angular velocity (rad/s)

Abbreviations

DOL	Direct-on-line
FE	Finite Element
FEM	Finite Element Method
IM	Induction Machine
MST	Maxwell Stress Tensor
PQA	Power Quality Analyser
PWM	Pulse Width Modulation
RSM	Reluctance Synchronous Machine
SRM	Switched Reluctance Machine

1. Introduction

1.1. History of RSMs and their drives

The phenomenon of electromagnetism was discovered in 1820 by Oersted (Jezek, 2006), which effectively led to Taylor's discovery of the first electromagnetic engine (Aljaism, 2007) in 1838 and, in that same year, the first concept of a switched reluctance machine (SRM) by Davidson (Skvarenina, 2001) in which he propelled a locomotive into motion near Falkirk. Blondel (1913) wrote how Siemens, in 1874, discovered the effect of magnetic reluctivity in his synchronous generator when he realised he could attain a continuous motion after removing the rotor's excitation.

Over the next few years (1874 - 1913) the RSM sparked the interest of only a few researchers (Blondel, 1913; Thompson, 1902) as the main focus became Nikola Tesla's IM. Research on the RSM gradually faded until the initiative of Kostko (1923). He realised that the reluctance motor's "inferiority" was only due to its "faulty form of the rotor." Following on from this ground-breaking realisation, he then replaced the salient-pole rotor with a novel, round rotor, having internal flux barriers and cut-outs. This was a milestone in the development of RSMs, returning it once more to the limelight where its performance to other AC machines was compared.

It was around 1925 that the first paper on inverter drives was published which made use of controlled valve technology (Hoft, 1983). This did not turn out to be a popular technology at the time, and it was not until the discovery of the bipolar transistor in 1948 and the thyristor in 1958 that the power electronic era was revolutionised, allowing further discoveries to be made.

While the power electronic era was still in its development stages, engineers and researchers (Trickey, 1933; 1946; Talaat, 1951; Lin, 1951) focused on the theoretical performance of the RSM. Crouse (1951) investigated the design aspects of the RSM, along with the derivation of its equivalent circuit and parameters. Lin (1952) then continued the equivalent circuit calculations. By this time the development of the DC

motor drive system had already taken off which was followed by the infant stages of the AC motor drive system in the 1960s (Yano *et al*, 1983).

Although the interest in the RSM had grown considerably between the 1960s and the 1970s due to the contributions from various researchers, this machine had not yet been researched with reference to the developing AC drives. The theory of RSMs under various operating frequencies was investigated by Lipo (1967), however, slow-speed RSMs had already been in use in industry since 1956 for an atomic reactor, which ranged from frequencies of 0.3Hz – 1.5Hz (Guerdan, 1956). The main focus of research performed in this era was on rotor geometry alterations and stability analysis. Lawrenson*, et al.* (1963; 1964; 1964) investigated the performance of a segmented RSM. He developed new theories, comparing it to an older salient-pole type. In continuing his research, Lawrenson (1971) also set out to investigate the performance of an improved, segmented RSM's synchronous- and asynchronous mode of operation.

Making use of digital and analogue computer aided calculations, Lipo & Krause (1967) investigated the stability of the RSM, using the Nyquist stability criterion. This effectively led to further investigations, including methods of improving the stability of the RSM by researchers such as Krause (1968), Hoft (1968), Kanijo & Mohanty (1968), Lawrenson & Bowes (1971), and Cruickshank, *et al*. (1971).

The interest in the performance control of RSMs grew after Krause and Lipo (1969) experimented with the rectifier-inverter RSM to establish simplified representations of its performance. Since then, inverter drives started to become more readily available for the speed, control and start of RSMs for open loop systems, and it was not until the late 1970s that Faucher*, et al.* (1979) investigated the operation of a controlled, current-fed RSM using a closed-loop system. By taking saturation of the d- and q-axes into account, Faucher compared numerical calculations and computer simulations with experimental measurements, to determine the RSM's characterisation in a closed-loop, steady-state system.

It was during this era that researchers decided to adapt the rapid growing technology of vector-controlled (current-fed) drives to the RSM. The majority of the

aforementioned researchers and engineers who performed practical tests on RSMs controlled their motors from a standard, voltage-fed, fixed frequency supply and used the method of driving the RSM into synchronism by incorporating a caged rotor (damping windings) or by accelerating the RSM into synchronism via an external DC motor (Vasudevan *et al.*, 2012). In present day industry the majority of RSMs are largely fed by electronic vector drives, which control the currents and magnetic flux inside the motor. Using a closed-loop feedback system, the drive's magnetic flux components are then continuously adjusted to compensate for the change in impedance as the rotor moves.

1.2. Recent research on voltage-fed RSMs

Recently, Ferraz *et al.* (2001) performed a set of practical tests to determine the equivalent circuit of a voltage-fed, cage-rotor motor. The motor's parameters (frequency and stator voltage) were adjusted to obtain certain parameters for the circuit and the tests were performed in transient- and steady-state mode. However, no attention was given to the motor's harmonic components under these voltage-fed conditions. Lawrenson (1972) also investigated the performance of a RSM in its asynchronous (transient) stage to determine how the torque, current distribution, saliency ratio and stator resistance are affected for irregular rotor conductor distributions.

Ferraz and de Souza (2002) then performed another set of practical experiments for a voltage-fed, caged RSM to obtain quantities such as current, inductance, flux linkage and torque. The paper explained how the various induction losses can be categorised in order to determine individual flux linkage parameters. The focus was primarily on the transient operation, but some additional results were given such as torque/speed and line-current/speed performance in steady-state.

Nam*, et al.* (2004) investigated a caged, voltage-fed RSM, having several different rotor bar configurations. The work focussed on the starting torque produced at several rotor speeds and rotor starting positions and gave results for parameters such as efficiency, power loss, current, torque, and power factor in steady-state.

Although the majority of authors investigated the performance of a voltage-fed, caged RSM, the focus was primarily on the motor's starting conditions. The few that did investigate its steady-state operation did not fully analyse its performance, compare it to a similar motor under sensorless vector-control (current-fed) or meet the criteria of parameters previously mentioned. Additionally, it was also not determined how these parameters are affected at different values of load torque. From the above mentioned sources, it can be gathered that there is not a lot of information on the actual steady-state performance of a voltage-fed RSM and how it compares to a current-fed RSM under various loads.

1.3. Problem statement

In industry today, the majority of RSMs are current driven by vector-controlled drives to deliver an efficient and qualitative performance. They provide options for different tasks ranging from variable torque to variable speed applications. The problem with these drives is that they inject a considerable amount of harmonics into the grid, can become an expensive addition to the RSM setup and produce pulse width modulation (PWM) losses (Wakileh, 2003). In certain fixed speed applications, less motor control is required and the drive becomes redundant.

For fixed speed applications the average consumer will most likely have a preference for IMs in the sense that they are more readily available – "off the shelf" models – which can be started DOL and need no additional drives to meet the basic requirements. These IMs, however, tend to dissipate more heat due to copper loss in the rotor windings, giving RSMs an advantage and making them a viable option for such applications (Boglietti, 2008). Having taken all of this into consideration, the question arises; how do voltage-fed RSMs compare to current-fed RSMs for fixed speed applications?

It is therefore of academic interest to find out how the RSM, supplied by a DOL sinusoidal voltage, would perform when being compared to a current-fed RSM controlled by sensorless vector drive. Some of the publications mentioned in Section

1.1 and 1.2 have performed adequate studies on the basic parameters of a caged, voltage-fed RSM, but to the author's knowledge, have not yet been compared to a current-fed RSM. These results have also not yet been analysed with the use of a Finite Element Method (FEM) and compared to practical results. The question therefore not only becomes how they compare in practice, but also how they compare when being simulated with a constant current and a constant voltage source.

The FEM is a vital tool in the analysis of any motor as it can be very difficult to acquire certain parameters by means of analytical formulations or practical measurements. It also takes a lot of precision to model a machine as accurately as possible that is supplied with a constant voltage, as the mechanical dynamics of the motor are a function of the load drawn. It is therefore of interest to determine how the RSM responds to a sinusoidal voltage in its steady-state mode of operation, how it compares to the current-fed RSM, and to find an acceptable coherency between simulated and practical results in FE.

1.4. Problem approach

Since a voltage-fed RSM is being analysed in this study, it would be ideal to use a caged rotor to assist in the starting procedure and provide the necessary stability with the use of a damper cage. However, since the study only focuses on steady-state operations, the cage would have been redundant at synchronous speed.

A cageless RSM is therefore selected, based on a modified design by Hanekom (2006), who's objective was to find a rotor and stator configuration having an optimum torque ripple percentage. Before this, the rotor was modified by Kamper (1996) using an FE-integrated optimisation algorithm to improve the overall performance of the RSM. In this study, the stator used consists of 36 open slots with full pitched windings while the rotor is made of a single salient, unskewed, transverse laminated stack with two internal flux barriers per pole. Before the RSM was manufactured for this institution, it was slightly modified by replacing the rotor cut-outs with the same material as the rest of the rotor. This will decrease the average torque and power factor to some extent, but will remove a considerable amount of

torque ripple (Hanekom, 2006). The RSM used in this study is displayed in Figure 1.4.1.

Power Rating	3kW
Number of poles	4
Number of slots	36
Pole pitch	9
Flux barrier pitch	26°
Stator outer-diameter	203.2mm
Stator inner-diameter	126.98mm
Rotor diameter	126.3mm
Air-gap	0.34mm
Stack length	133.4mm
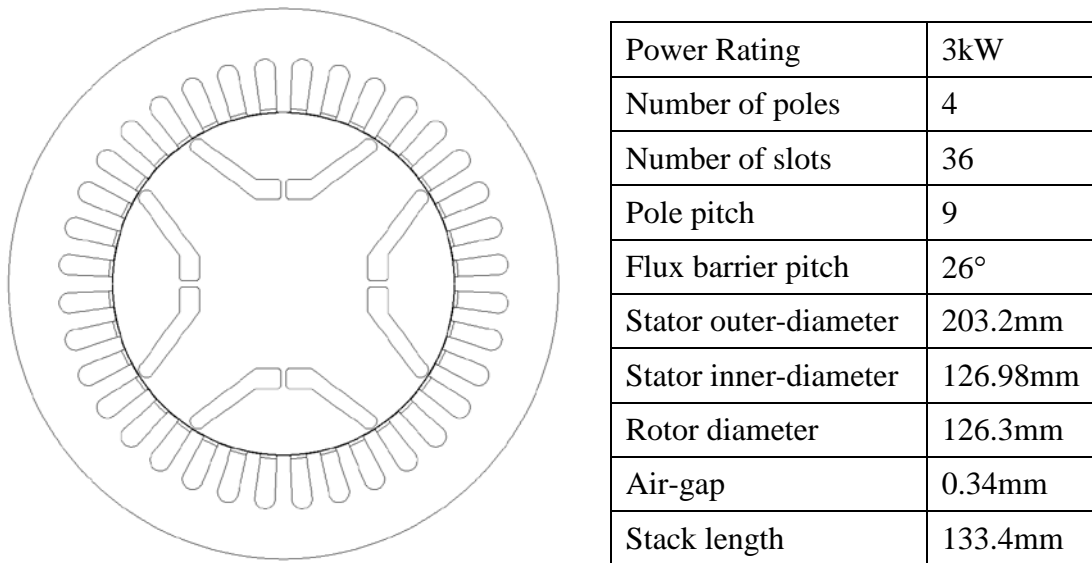
Fig. 1.4.1 Axial view and dimensions of RSM

The laminations for this RSM have already been laser-cut and assembled and the windings have been wound to the specifications of a 3kW motor. Following this, a test bench comprising a mechanically coupled RSM, torque-meter and DC motor will be assembled and connected to a control panel, containing the drive for the RSM and DC motor. The relevant parameters are then measured, along with the RSM's current angle.

Since a practical concern of the RSM is the starting, it will be driven to its synchronous speed with the DC motor, and then switched over to a constant 3-phase voltage source. For the current-fed operation it will use the drive start the RSM in the conventional manner. The general layout of both modes of operation is shown in Figure 1.4.2.
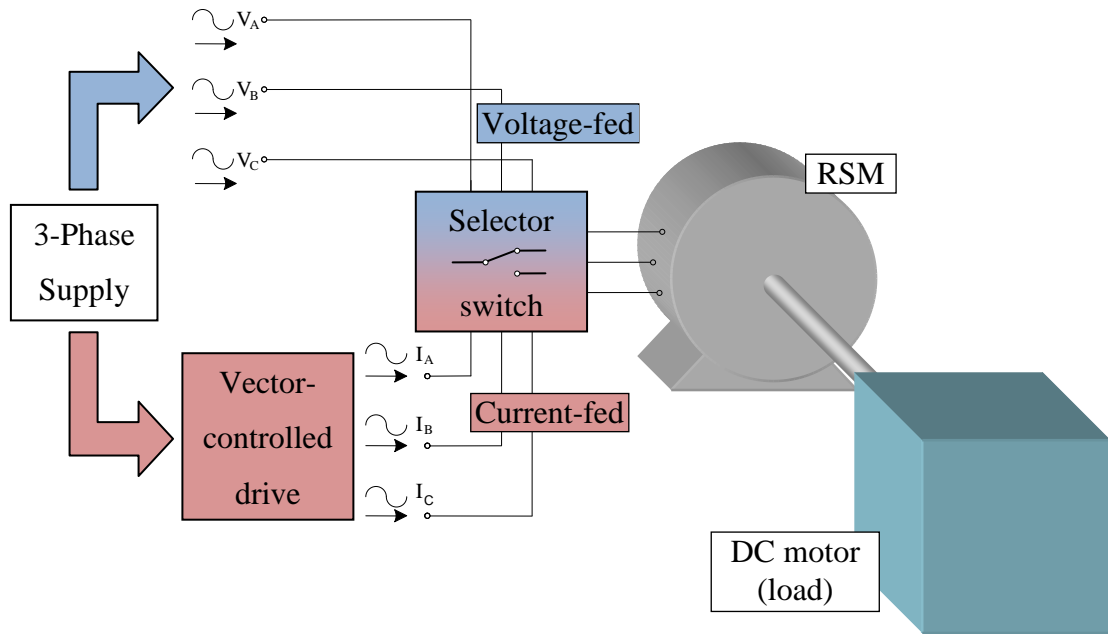
Fig. 1.4.2. Basic layout of RSM study

This study will put a significant amount of emphasis on the modelling procedure and accuracy of the voltage- and current-fed RSM. Using a 2D FE software package, both the current- and voltage-fed RSMs will be analysed in the time-domain. These studies will only focus on steady-state behaviour to determine the parameters such as torque, power factor, efficiency, harmonics, losses, and inductance. To perform a 2D study on a voltage-fed RSM using a FEM, the stator's end-winding leakage reactances need to be taken into account separately. To incorporate these end-effects, an external equivalent circuit must be included in the simulation to account for the additional voltage drop in the motor. Williamson *et al*. (1995) outlined a computational method for simulating a motor through FE by using a salient pole synchronous generator and IM as example. The paper signified the importance of using external circuit equations to impose a voltage balance around the rotor- and stator-windings. These take any stator and rotor losses into account – the most crucial being end-winding leakage reactance of the stator windings. The end-winding reactance can be determined by using several calculation methods. These methods are categorised into two sub-categories, namely; analytical formulations (Alger, 1951; Lawrenson, 1961; Liwschitz, 1961; Reece & Pramanick, 1965; Schuisky, 1960) and complex numerical formulations (Lawrenson, 1961; Williamson & Mueller, 1990).

The motor's mechanical load plays a big role in the amount of current it draws and as a consequence affect the other parameters. It therefore becomes essential to model the motor's mechanical behaviour as accurately as possible using the FE software by taking the moment of inertia, mechanical load, current angle, and friction and windage losses into account.

1.5. Outline of thesis

The layout of the remaining part of the thesis is as follows:

Chapter 2:   A mathematical model of the voltage-fed RSM is given, along with the mathematical derivations of the motor's performance parameters for fundamental values. These parameters include voltage, current and flux linkage space phasors as well as torque and power factor. A general explanation is given on how the voltage-fed RSM operates in FE, using magnetic field equations combined with circuit equations.

Chapter 3:   The voltage-fed RSM's equivalent circuit and mechanical model is compiled by measuring and calculating all the parameters necessary to simulate the machine in FE as accurately as possible. The RSM is tested in a laboratory to measure friction and windage losses, stator resistance as well as the motor's moment of inertia. From this, the remaining parameters such as the end-winding leakage reactance and core loss are calculated to contribute to the equivalent circuit. The mechanical model used in the FE software is explained and shown how the calculations are integrated into the program. Finally, an explanation is given as to how the RSM's current angle is measured.

Chapter 4:   The voltage-fed RSM is measured on a test bench and compared with the current-fed RSM in terms of its torque, torque-ripple, current, voltage, power-factor, efficiency, current angle and direct (d) and quadrature (q) axis currents. These parameters are compared for different values of loads, ranging from no-load to 150% full-load.

Chapter 5: Before the RSM is simulated in FE, an accuracy study is performed by comparing the measured inductance (excluding saturation) and efficiency with simulated values. The RSM's current and voltage harmonic components are then analysed for both the voltage- and current-fed RSMs. The d- and q-axis inductances (including saturation) are further analysed and is also used to explain the voltage-fed RSM's pull-out torque. A deeper investigation into the motor's core losses is also discussed and analysed, this time using FE to break it down into its three components, namely hysteresis, eddy current and excess loss.

Chapter 6: The previous chapters' findings are summarised, discussed and conclusions are drawn from the acquired results, including the advantages and disadvantages of the voltage-fed RSM. Recommendations are also made to apply the voltage-fed RSM to practical scenarios. The chapter ends with recommendations for future research.

2. Overview of the RSM

2.1. Mathematical model of the machine

The principle of synchronous machines can be understood in terms of its d- and q-axes. This method, which is also known as a *dq0*-transformation, changes the motor's stationary 3-phase coordinate system to a rotating *dq0*-coordinate system (Figure 2.1.1).
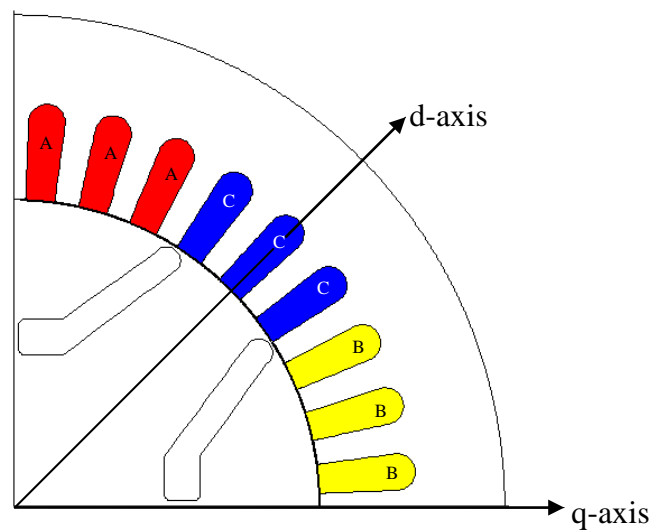
Fig. 2.1.1 Quarter stator representation of d- and q-axes with respect to ACB stator phases

The following assumptions are made for this section:

- A symmetrical 3-phase system
- Core losses and eddy currents are neglected
- Only fundamental values are considered

This transformation from 3-phase stationary quantities to two-axis rotor quantities is represented in the form of a matrix *K*:

$$K = \left(\frac{2}{3}\right) \begin{bmatrix} \cos\theta & \cos\left(\theta - \frac{2\pi}{3}\right) & \cos\left(\theta + \frac{2\pi}{3}\right) \\ \sin\theta & \sin\left(\theta - \frac{2\pi}{3}\right) & \sin\left(\theta + \frac{2\pi}{3}\right) \\ \frac{1}{2} & \frac{1}{2} & \frac{1}{2} \end{bmatrix} \qquad (2.1.1)$$

The inverse of matrix K:

$$K^{-1} = \begin{bmatrix} \sin\theta & \cos\theta & 1 \\ \sin\left(\theta - \dfrac{2\pi}{3}\right) & \cos\left(\theta - \dfrac{2\pi}{3}\right) & 1 \\ \sin\left(\theta + \dfrac{2\pi}{3}\right) & \cos\left(\theta + \dfrac{2\pi}{3}\right) & 1 \end{bmatrix} \qquad (2.1.2)$$

2.1.1. Voltage calculation

With R_S being the stator resistance, and λ_{abc} the stator flux linkage of the three phases in matrix form, the stator voltage is consequently defined as:

$$v_{abc} = R_s i_{abc} + \frac{d}{dt}\lambda_{abc} \qquad (2.1.1.1)$$

The three phases, representing a stationary time-dependant system, is then transformed to a rotating time-dependant system using eq. (2.1.1)

$$K^{-1}v_{dq} = R_s\left(K^{-1}i_{dq}\right) + \frac{d}{dt}\left(K^{-1}\lambda_{dq}\right) \qquad (2.1.1.2)$$

By applying the matrix K in eq. (2.1.1) on both sides of eq. (2.1.1.2), one obtains

$$v_{dq} = R_s i_{dq} + \frac{d}{dt}\lambda_{dq} + K\left(\frac{d}{dt}K^{-1}\right)\lambda_{dq} \qquad (2.1.1.3)$$

where $K\left(\dfrac{d}{dt}K^{-1}\right) = \begin{bmatrix} 0 & -\omega_e & 0 \\ \omega_e & 0 & 0 \\ 0 & 0 & 0 \end{bmatrix}$ and ω_e is the electrical angular velocity.

Eq. (2.1.1.3) can now be extrapolated into its respective components,

$$v_d = R_s i_d + \frac{d}{dt}\lambda_d - \omega_e \lambda_q \qquad\qquad (2.1.1.4)$$

$$v_q = R_s i_q + \frac{d}{dt}\lambda_q + \omega_e \lambda_d \qquad\qquad (2.1.1.5)$$

where the flux linkage components are defined as

$$\lambda_d = L_d i_d \qquad\qquad (2.1.1.6)$$

$$\lambda_q = L_q i_q \qquad\qquad (2.1.1.7)$$

It is clear, for both these d- and q-voltage equations, that the flux linkage components are functions of the rotor angle θ as well as the d- and q-currents because of cross coupling between the two axes.

$$\lambda_d = \lambda_d(i_d(t), i_q(t), \theta(t)) \qquad\qquad (2.1.1.8)^*$$

$$\lambda_q = \lambda_q(i_q(t), i_d(t), \theta(t)) \qquad\qquad (2.1.1.9)^*$$

Eq. (2.1.1.4) and eq. (2.1.1.5) are expanded into the following two equations:

$$v_d = R_s i_d + \frac{\partial \lambda_d}{\partial i_d}\frac{di_d}{dt} + \frac{\partial \lambda_d}{\partial i_q}\frac{di_q}{dt} + \frac{\partial \lambda_d}{\partial \theta}\omega_e - \omega_e \lambda_q \qquad\qquad (2.1.1.10)$$

$$v_q = R_s i_q + \frac{\partial \lambda_q}{\partial i_q}\frac{di_q}{dt} + \frac{\partial \lambda_q}{\partial i_d}\frac{di_d}{dt} + \frac{\partial \lambda_q}{\partial \theta}\omega_e + \omega_e \lambda_d \qquad\qquad (2.1.1.11)$$

In eq. (2.1.1.8) and (2.1.1.9) the terms $\dfrac{\partial \lambda_d}{\partial i_d}\dfrac{di_d}{dt} + \dfrac{\partial \lambda_d}{\partial i_q}\dfrac{di_q}{dt}$ and $\dfrac{\partial \lambda_q}{\partial i_q}\dfrac{di_q}{dt} + \dfrac{\partial \lambda_q}{\partial i_d}\dfrac{di_d}{dt}$

can be rewritten as

$$\frac{\partial \lambda_d}{\partial i_d}\frac{di_d}{dt} + \frac{\partial \lambda_d}{\partial i_q}\frac{di_q}{dt} = L_d' \frac{di_d}{dt} + M_{dq}' \frac{di_q}{dt} \qquad\qquad (2.1.1.12)$$

$$\frac{\partial \lambda_q}{\partial i_q}\frac{di_q}{dt} + \frac{\partial \lambda_q}{\partial i_d}\frac{di_d}{dt} = L_q^{'}\frac{di_q}{dt} + M_{qd}^{'}\frac{di_d}{dt} \qquad (2.1.1.13)$$

where $L_d{'}$ and $L_q{'}$ are the d- and q-self-inductances and $M_d{'}$ and $M_q{'}$ are the d- and q-mutual inductances, respectively. They are indicated with a dash to represent dynamic rotor quantities.

2.1.2. Current space phasor

The d- and q-currents in the rotating coordinate system are calculated from the stator currents as:

$$i_d = \frac{2}{3}\left(i_a \cos(\omega_e t) + i_b \cos(\omega_e t - 120°) + i_c \cos(\omega_e t + 120°)\right) \qquad (2.1.2.1)$$

$$i_q = -\frac{2}{3}\left(i_a \sin(\omega_e t) + i_b \sin(\omega_e t - 120°) + i_c \sin(\omega_e t + 120°)\right) \qquad (2.1.2.2)$$

From the above mentioned quantities it is possible to obtain the voltage space phasor $\vec{V}_s$, current space phasor $\vec{I}_s$, as well as the flux linkage space phasor $\vec{\lambda}_s$, all of which are expressed in magnitude and angle from the d- and q-voltage, current, and flux linkage quantities.

$$\vec{V}_s = \sqrt{v_d{}^2 + v_q{}^2} \angle \tan^{-1}\left(\frac{v_q}{v_d}\right) \qquad (2.1.2.3)$$

$$\vec{I}_s = \sqrt{i_d{}^2 + i_q{}^2} \angle \tan^{-1}\left(\frac{i_q}{i_d}\right) \qquad (2.1.2.4)$$

$$\vec{\lambda}_s = \sqrt{\lambda_d{}^2 + \lambda_q{}^2} \angle \tan^{-1}\left(\frac{\lambda_q}{\lambda_d}\right) \qquad (2.1.2.5)$$

These vectors can also be represented in a phasor diagram (Figure 2.1.2) which gives an intuitive understanding as to how they relate to each other. In this diagram, φ is angle between the voltage and current space phasor and γ is the angle between the flux linkage and current space phasor. The remaining two angles, δ and ϑ, are the angular distances from the d-axis for the flux linkage and current space phasors,

13

respectively. Here the flux linkage excludes any leakages in order to maintain simplicity but these will be covered in a later section.
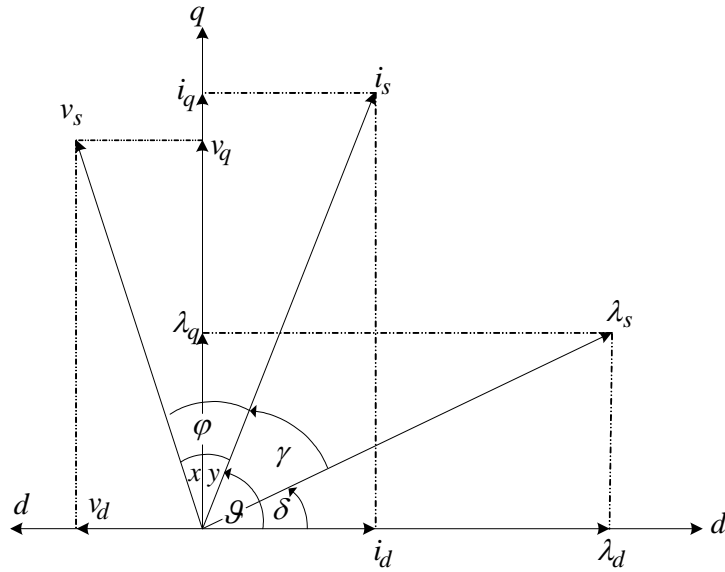
Fig. 2.1.2 Space phasor diagram

2.1.3. Power factor

The angle φ is referred to as the power factor angle (Figure 2.1.2). Parasiliti (1995) defines the power factor as the "ratio between the projection of the voltage vector on the current vector and the amplitude of the voltage vector". Assuming the angle φ is the sum of angles x and y, the power factor $cos\varphi$ can be written as

$$\cos \varphi = \cos(x + y) \tag{2.1.3.1}$$

$$\cos \varphi = \cos x \cos y - \sin x \sin y \tag{2.1.3.2}$$

Referring to Figure 2.1.2, eq (2.1.3.1) can be written in terms of d- and q- voltage and current quantities.

$$\cos \varphi = \frac{v_q}{v_s} \frac{i_q}{i_s} - \frac{v_d}{v_s} \frac{i_d}{i_s} \tag{2.1.3.3}$$

The currents in these two terms are defined as sine and cosine functions in terms of the current angle ϑ, according to

$$
\frac{i_q}{i_s} = \sin \vartheta
$$
$$
\frac{i_d}{i_s} = \cos \vartheta
$$

(2.1.3.5)

The power factor is then written in terms of its three voltage components, as well as the current angle.

$$
\cos \varphi = \frac{v_q \sin \vartheta - v_d \cos \vartheta}{v_s}
$$

(2.1.3.6)

Additionally, the power factor can be calculated in terms of the d- and q-axis inductance and current components. Ignoring stator resistance and iron loss, the power factor can be written as

$$
\cos \varphi = \cos \left(\tan^{-1} \left(\frac{\tau/\upsilon + \upsilon}{\tau - 1} \right) \right)
$$

(2.1.3.7)

where τ is the saliency ratio (*Ld/Lq*) and υ is the *id/iq* current ratio.

2.1.4. Torque

One of the simplest equations for calculating the torque found on the surface of the rotor is expressed in eq. (2.1.4.1) as the cross product between the current and flux linkage space phasors. The angle between these two quantities (see Figure 2.1.2) is also known as the torque angle γ.

$$T = \frac{3}{2}\left(\lambda_s \times I_s\right)$$
(2.1.4.1)

This is an approximate equation and does not account for the RSM's slotted air-gap. According to Hanekom (2006), this slotted air-gap can be accounted for in eq. (2.1.4.2) by using the motor's d- and q-current and flux components.

$$T = \frac{3}{4} p \left[\frac{1}{2}\left(i_d \frac{\partial \lambda_d}{\partial \theta} + i_q \frac{\partial \lambda_q}{\partial \theta} \right) - \lambda_q i_d + \lambda_d i_q \right]$$
(2.1.4.2)

The first term includes the change in flux linkage as a function of the rotor angle and therefore accounts for the torque ripple. The second term in eq. (2.1.4.2) is based on a linear magnetic circuit (no saturation) and therefore assumes no cross-coupling. The FE software used in this study, however, takes saturation and cross-coupling into account and uses the Maxwell stress tensor (MST) method to calculate the normal and tangential torque components. These components are functions of the normal and tangential stress tensors given in eq. (2.1.4.3) and (2.1.4.4).

$$\sigma_n = \frac{B_n{}^2 - B_t{}^2}{2\mu_0}$$
(2.1.4.3)

$$\sigma_t = \frac{B_n B_t}{\mu_0}$$
(2.1.4.4)

These tensors are calculated in the centre of the air gap by integrating the normal and tangential flux density components B_n and B_t along a contour Γ and multiplying it by the radius r of the path through the air gap. Eq. (2.1.4.5) gives the formula for the MST's tangential component as it is the one responsible for the rotor movement.

$$T_t = \frac{1}{\mu_0} \oint_\Gamma r B_t B_n d\Gamma \times \ell_s \qquad (2.1.4.5)$$

Where μ_0 is the permeability of free space, and ℓ_s is the motor's effective stack length. Although the two methods for torque calculation were compared by Hanekom (2006) and showed acceptable coherency, the MST method will be used for the torque calculation in this study.

2.2. Coupled magnetic field and electrical circuit equations

In the conventional case of simulating a current-fed RSM, the current density $\vec{J}$ is calculated in eq. (2.2.1) using the magnetic field strength $\vec{H}$ according to Ampère's Law (Bastos & Sadowski, 2003).

$$\vec{J} = curl\vec{H} \qquad (2.2.1)$$

which is then written in terms of the flux density $\vec{B}$ and the reluctivity ν according to

$$\vec{J} = curl\left(\nu\vec{B}\right) \qquad (2.2.2)$$

Since

$$\vec{B} = curl\vec{A}, \qquad (2.2.3)$$

the current density can then be expressed in terms of the vector potential $\vec{A}$ according to

$$\vec{J} = curl\left(\nu curl\vec{A}\right) \qquad (2.2.4)$$

The curl of the product of a scalar and vector function can be written as

$$\vec{J} = vcurlcurl\vec{A} - \vec{A} \times grad\,v \tag{2.2.5}$$

For 2D problems the vector potential $\vec{A}$ only has a z-component, and the reluctivity v is a function of the x- and y-plane.

$$\vec{A} = \vec{e}_z A_z \tag{2.2.6}$$

$$v = \vec{e}_x v_x + \vec{e}_y v_y \tag{2.2.7}$$

The gradient of v is written as

$$grad\,v = \left(\frac{\partial v}{\partial x} ; \frac{\partial v}{\partial y} \right) \tag{2.2.8}$$

Eq. (2.2.5) is therefore

$$\vec{J} = vcurl\left(\vec{e}_x \frac{\partial \vec{A}_z}{\partial y} - \vec{e}_y \frac{\partial \vec{A}_z}{\partial x} \right) + \vec{e}_x \frac{\partial v\vec{A}_z}{\partial y} - \vec{e}_y \frac{\partial v\vec{A}_z}{\partial x} \tag{2.2.9}$$

$$\vec{J} = v\vec{e}_x \frac{\partial^2 \vec{A}_z}{\partial x \partial z} + \vec{e}_y \frac{\partial^2 \vec{A}_z}{\partial y \partial z} + \vec{e}_z \left(\frac{\partial^2 \vec{A}_z}{\partial x^2} + \frac{\partial^2 \vec{A}_z}{\partial y^2} \right) + \vec{e}_x \frac{\partial v\vec{A}_z}{\partial y} - \vec{e}_y \frac{\partial v\vec{A}_z}{\partial x} \tag{2.2.10}$$

It is clear that the current-fed RSM can be simulated using only the vector potentials and the reluctivity. Since, in a voltage-fed machine, all the individual voltage drops must be simulated, the end-windings, which are not included in any two-dimensional simulation, must be considered separately. This is achieved by including an external equivalent circuit into the FE calculation. As a consequence, the simulation is made up of circuit as well as field equations. The terminal voltage is supplied by the user, which, in effect, calculates the vector potentials and magnetising currents from the circuit parameters using the combined field and circuit equations (Bastos & Sadowski, 2003).

The calculation for the voltage in an electrical machine can be described in its simplest form as

$$v = iR + \frac{d\lambda}{dt} \qquad\qquad (2.2.11)$$

Since the FE program in this study performs its calculations in a 2D mesh, the end-windings are included as a separate, series inductance in the equivalent circuit. This study therefore assumes the end-winding flux λ_e to be a function of the current only and the main flux to be a function of the current and rotor angle.

$$\lambda_e = \lambda_e(i)$$
$$\lambda_m = \lambda_m(i,\theta)$$

Eq. (2.2.11) is consequently expressed as

$$v = iR + \frac{d}{dt}\left(\lambda_m + \lambda_e\right) = iR + \frac{d}{dt}\left(\lambda_m(i,\theta) + \lambda_e(i)\right) \qquad\qquad (2.2.12)$$

$$v = iR + \frac{\partial \lambda_m}{\partial i}\frac{di}{dt} + \frac{\partial \lambda_m}{\partial \theta}\frac{d\theta}{dt} + \frac{\partial \lambda_e}{\partial i}\frac{di}{dt} \qquad\qquad (2.2.13)$$

The end-winding inductance is a constant value and can be written as a voltage-drop across an inductor, while the remaining magnetising flux-component responsible for torque production is defined as λ_m.

$$v = iR + \frac{d\lambda_m}{dt} + i\omega L_e \qquad\qquad (2.2.14)$$

The instantaneous current and flux linkage can be written in its integral form to represent the current density $\vec{J}$ and the magnetic flux density $\vec{B}$.

$$v = R\iint\limits_{a_s} \vec{J} \cdot d\bar{a}_s + \frac{d}{dt}\iint\limits_{a_r} \vec{B} \cdot d\bar{a}_r + i\omega L_e \qquad (2.2.15)$$

It is important to realise that the current density component is only integrated over the surface of the slot $\bar{a}_s$ while the flux density is integrated over the surface area $\bar{a}_r$ having the radius from the centre of the rotor to the centre of the air gap. Since the current density $\vec{J}$ in eq. (2.2.15) is an unknown factor, it can be written as the product of the conductivity σ and the electric field strength $\vec{E}$ according to one of Maxwell's constitutive equations (Ohm's Law).

$$\vec{J} = \sigma\vec{E} \qquad (2.2.16)$$

The electric field strength can be written in terms of the flux density $\vec{B}$ (Faraday's Law).

$$curl\vec{E} = -\frac{\partial\vec{B}}{\partial t} \qquad (2.2.17)$$

$$curl\vec{E} + \frac{\partial\vec{B}}{\partial t} = 0 \qquad (2.2.18)$$

Using eq. (2.2.18)

$$curl\vec{E} + curl\frac{\partial\vec{A}}{\partial t} = 0 \qquad (2.2.19)$$

which is only true if the circuit's dimensions do not change with time. Eq. (2.2.19) is then used to obtain

$$curl[\vec{E} + \frac{\partial\vec{A}}{\partial t}] = 0 \qquad (2.2.20)$$

Because the curl of any scalar function is zero, the term in brackets can now be written as

$$\bar{E} + \frac{\partial \bar{A}}{\partial t} = -gradV \tag{2.2.21}$$

or

$$\bar{E} = -\frac{\partial \bar{A}}{\partial t} - gradV \tag{2.2.22}$$

and eq. (2.2.16) becomes

$$\bar{J} = \sigma \left[-\frac{\partial \bar{A}}{\partial t} - gradV \right] \tag{2.2.23}$$

The current density $\bar{J}$ can now be written in terms of the electric scalar potential V, the vector potential $\bar{A}$ and the conductivity σ.

$$v = R\sigma \iint_{a_s} \left(-\frac{\partial \bar{A}}{\partial t} - gradV \right) \cdot d\bar{a}_s + \frac{d}{dt} \iint_{a_r} \bar{B} \cdot d\bar{a}_r + i\omega L_e \tag{2.2.24}$$

Since $\bar{B} = curl\bar{A}$,

$$v = R\sigma \iint_{a_s} \left(-\frac{\partial \bar{A}}{\partial t} - gradV \right) \cdot d\bar{a}_s + \frac{d}{dt} \iint_{a_r} curl\bar{A} \cdot d\bar{a}_r + i\omega L_e \tag{2.2.25}$$

Using Stoke's law,

$$\iint_F curl\bar{F} \cdot d\bar{F} = \oint_C \bar{F} \cdot d\bar{r} \tag{2.2.26}$$

the second term of (2.2.24) is written as

$$v = R\sigma \iint\limits_{a_s} \left(-\frac{\partial \bar{A}}{\partial t} - gradV \right) \cdot d\bar{a}_s + \frac{d}{dt} \oint\limits_C \bar{A} \cdot d\bar{r}_r + i\omega L_e \tag{2.2.27}$$

The motor windings in this study are simulated to have a solid conductor in each slot. The voltage V_1 across a conductor with the length l is therefore written as

$$V_1 = \int\limits_0^l -(gradV)dl = -Vl \tag{2.2.28}$$

Using eq. (2.2.23), (2.2.18) and (2.2.28), the currents in the windings are therefore defined as

$$I_1 = \iint\limits_{a_s} \bar{J} \cdot d\bar{a}_s = -\iint\limits_{a_s} \sigma \frac{\partial A_z}{\partial t} \cdot d\bar{a}_s + \iint\limits_{a_s} \sigma \frac{V_1}{l} \cdot d\bar{a}_s \tag{2.2.29}$$

$$I_1 = -\iint\limits_{a_s} \sigma \frac{\partial A_z}{\partial t} \cdot d\bar{a}_s + \frac{V_1}{R_s} \tag{2.2.30}$$

Since the size of the slot's cross-section is known, the individual currents can be calculated through the use of the vector potentials and stator voltage (Bastos & Sadowski, 2003).

3. Test Bench Measurements and Parameter Calculations

3.1. FE equivalent circuit

In order to simulate the voltage-fed RSM, an equivalent circuit needs to be integrated into the FE model. It is therefore important to acquire all of the necessary parameters used in this study. These parameters are either calculated or measured, the latter made possible by using the test bench as mentioned in Section 1.4, which has now been assembled. The test bench is explained in further detail in Chapter 4. According to Kamper (1996) the equivalent circuit of a RSM can be represented by Figure 3.1.1 which is the basis of the circuit used in this study,

where

R_s - stator resistance,

L_e - end-winding leakage inductance,

R_c - core loss, and

L_m - magnetic inductance found in the active region of the motor.
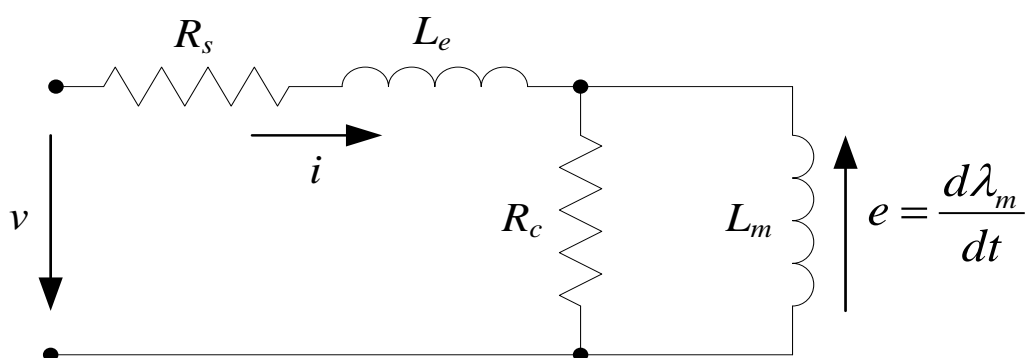

Fig. 3.1.1 Fundamental equivalent circuit of per phase RSM

The field equations (Section 2.2) are used to calculate the value of the magnetic inductance L_m while the remaining circuit elements are calculated using the given motor data.

3.1.1. Stator resistance

The calculation for the per phase resistance of the stator windings (eq. 3.1.1.1) is done using a method suggested by Kamper (1996).

$$R_S = \frac{2W\rho_t(l_s + l_e)}{n_a A_{cu}/z}$$

(3.1.1.1)

Where

W - number of turns in series per phase,

ρ_t - resistivity of copper at temperature t,

l_e - average length of a single end-winding,

l_s - stator stack length,

n_a - number of parallel circuits per stator winding,

A_{cu} - total active copper area, and

z - number of conductors per slot.

The resistivity of copper ρ_t at a temperature t is calculated using the formula

$$\rho_t = \rho_{20}\left(1 + \alpha_t\left(t_c - 20\right)\right)$$

(3.1.1.2)

where $\rho_{20} = 17 \times 10^{-9}\,\Omega.m$ and $\alpha_t = 0.0039/°C$. If the temperature at no-load is assumed to be $20°C$ and the temperature at full-load $75°C$, the stator resistances are

0.76Ω at $20°C$ (no-load) and

0.92Ω at $75°C$ (full-load).

These two values will be used for the FE modelling procedure.

3.1.2. End-winding leakage inductance

The end-windings, also known as the winding overhang, are situated on the ends of the stator stack length (Figure 3.1.2.1) and do not contribute to the torque production of the motor. They are simulated in FE as a separate, series voltage drop and therefore need to be calculated as one of the parameters in the RSM's equivalent circuit.
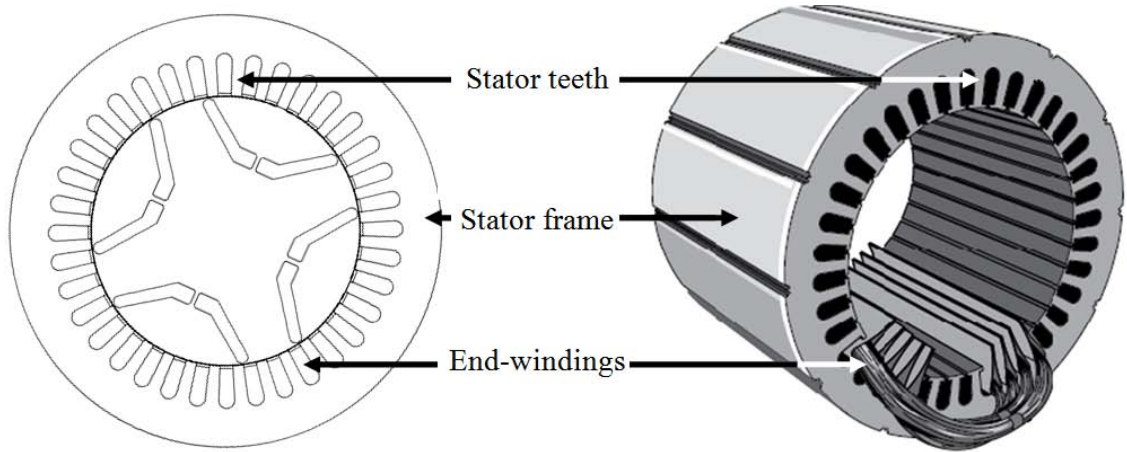
Fig. 3.1.2.1 An example of a motor's end-winding

The calculation is based on a formula given by Honsinger (1959) which was later simplified by Kamper (1996).

$$L_e = V_{(u)} m d_i \left[\frac{W k_d k_{p(u)}}{p} \right]^2 k_{e(p)} \cdot 10^{-8} \, Henry \, / \, phase$$

(3.1.2.1)

The subscript u in $V_{(u)}$ represents a constant that refers to the shape of the end-winding with

$V_1 = 600$ (V-shaped coils),
$V_2 = 1180$ (elliptical shaped coils), and
$V_3 = 1400$ (rectangular coils).

These constants are based on the work produced by Kamper (1996). Since the RSM investigated in this study has an elliptical shaped end-winding, the co-efficient $V_2 = 1180$ is selected for calculation. Furthermore, m represents the number of phases, d_i

the stator's inner diameter, W the number of turns in series per phase, p the number of pole pairs, k_d the distribution factor, given by

$$k_d = \frac{\sin\left(\dfrac{\pi}{6}\right)}{q\sin\left(\dfrac{\pi}{6q}\right)} \qquad (3.1.2.2)$$

and $k_{p(u)}$ the end-winding pitch factor. Similar to $V_{(u)}$, the factors $k_{p(1)}$, $k_{p(2)}$, and $k_{p(3)}$ refer to a V-shaped, elliptical-shaped, and rectangular coil respectively. The factors can be calculated as follows:

$$k_{p(1)} = \frac{3\sin\left(\dfrac{\pi c}{6q}\right)}{4 - \left(\dfrac{c}{3q}\right)} \qquad (3.1.2.3)$$

$$k_{p(3)} = \sin\left(\frac{\pi c}{6q}\right) \qquad (3.1.2.4)$$

$$k_{p(2)} \approx \frac{k_{p(1)} + k_{p(3)}}{2} \qquad (3.1.2.5)$$

where c is the coil-pitch and q is the number of coils per pole phase group, in which case $k_{p(2)} = 1$. Finally, $k_{e(p)}$ represents the end-winding factor for a machine with p pole-pairs. The factors are specified as

$k_{e(1)} = 0.51,$
$k_{e(2)} = 0.595,$
$k_{e(3)} = 0.64,$ and
$k_{e(4)} = 0.785.$

For a 3-phase, 36 slot, 4-pole machine with an inner stator diameter of 126.98mm, having 210 turns in series/phase, with 3 coils/ppg, a coil-pitch of 9 and a distribution factor of 0.9597, an end-winding leakage inductance of $L_e = 9.778$ mH/phase is computed using equation (3.1.2.1).

3.1.3. Core-, friction- and windage loss

An ideal, lossless magnetic material would comprise a linear *B-H* curve, having no saturation or core losses (Figure 3.1.3.1a). When the saturation of the material is taken into account, it limits the maximum flux density inside the material, and as a consequence, the material becomes non-linear (Figure 3.1.3.1b). When the hysteresis and eddy current losses are taken into account, the *B-H* curve then becomes a hysteresis loop. This loop represents the materials demagnetisation characteristic after crossing zero and is caused by the coercive force of the material. Since the magnetic material in the motor is also conductive, the revolving magnetic field will induce circulating eddy currents in the core, which are reduced by the use of laminations. The area in Figure 3.1.3.1(c) represents the core loss in the material (Soong, 2008).
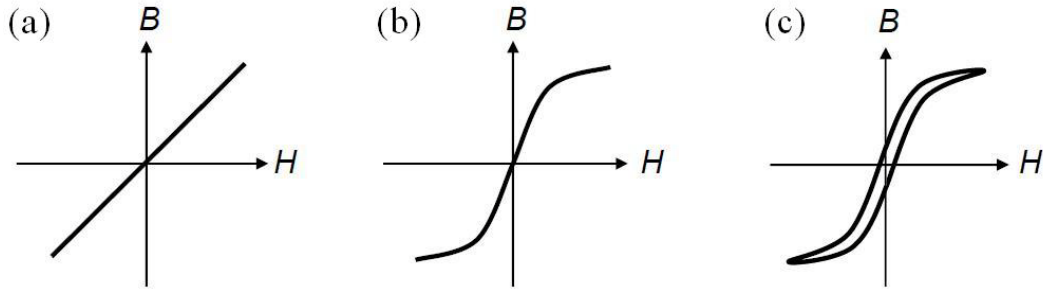

Fig. 3.1.3.1 *B-H* loops (a) ideal (b) saturated (c) saturated and hysteresis

Along with this core loss, an additional loss contributes significantly to the motor's overall efficiency, namely friction and windage loss. Friction and windage represent mechanical losses inside the motor. These losses consist primarily of bearing friction as well as wind friction in the air-gap and on the motor fan. According to the IEEE standard 112-2004 (IEEE Power Engineering Society, 2004) these losses can be determined through a series of power vs. voltage squared measurements. The power that is being compared is that which remains after the I^2R stator losses have been subtracted from the input power. It is important to determine the friction & windage loss as it gives an indication of what the motor's core loss is. From eq. (3.1.3.1) it can be seen that, since there is no mechanical load on the motor, the input power P_{in} can be expanded into its three main power components.

$$P_{in} = P_c + P_{cu} + P_{fw} \qquad (3.1.3.1)$$

Where P_c, P_{cu}, and P_{fw} represent the core, copper, and friction & windage losses, respectively. After P_{Cu} has been subtracted from the measured input power, the remaining power (P_c and P_{fw}) is recorded for decreasing steps of the input voltage until it is possible to extrapolate the curve to zero voltage. In this study however, the presence of the mechanically coupled DC motor adds an additional loss to the total input power. Due to practical reasons, it is not possible to decouple the DC motor from the RSM, adding an additional 2.12Nm between the two motors, which is accounted for in the final breakdown of these losses (see Figure 3.1.3.2). The loss caused by the DC motor P_{DC} now adds to the remaining power after the copper loss has been subtracted (P_c, P_{fw} and P_{DC}).

$$P_{in} = P_c + P_{cu} + P_{fw} + P_{DC} \qquad (3.1.3.2)$$

At the zero voltage intercept, the core loss becomes redundant, the DC motor loss is known, and the remaining unknown component is the friction and windage losses, represented in Figure 3.1.3.2.
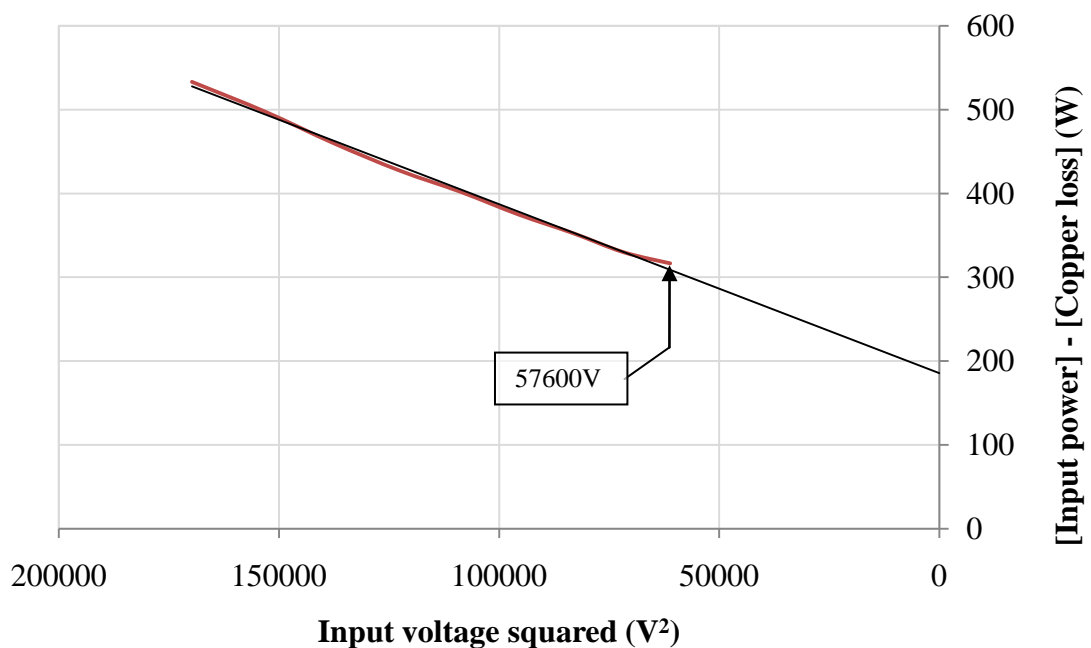

Fig. 3.1.3.2 Friction & windage as a function of the squared supply voltage at no-load

The power is measured up to a phase voltage of 240V (57600V when squared). A linear regression to the zero volt intercept shows the friction and windage loss to be 185.6W. The remaining core loss is roughly calculated using eq. (3.1.3.2), and the different losses are consequently represented in Figure 3.1.3.3.
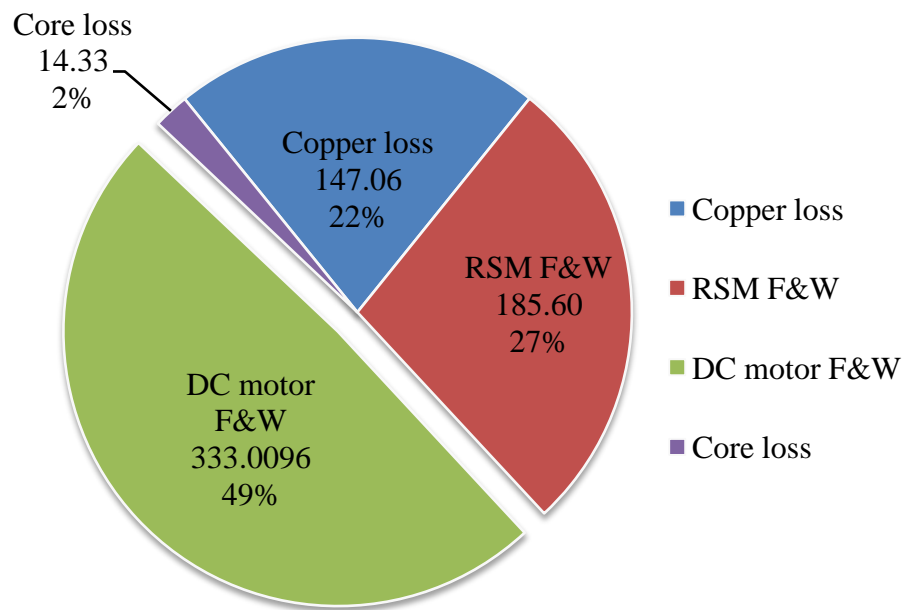
Fig. 3.1.3.3 Representation of the three main losses in the RSM at no load

3.2. FE mechanical model

To simulate the various loads that will be run on the test bench in Section 4, an integrated source code has to be written into the FE software. The source code uses an equation based on the calculation for the moment of inertia of a rotating body, which is dependent on the size and shape of the body and, in this study, comprises the RSM's rotor as well as the DC motor's armature. Due to the complex shape of the armature, this can quickly become a cumbersome task. The moment of inertia is therefore determined using the deceleration method (Louw, 2010).

3.2.1. Moment of inertia

The deceleration method uses eq. (3.2.3.1) which shows that it is a function of the deceleration, $\dfrac{d\omega}{dt}$, where ω is the angular mechanical velocity, $T_r(\omega)$ the reaction torque, $T_d(\omega)$ the developed torque and J the moment of inertia. It can also be seen that there is no change in inertia when the reaction torque is equal to the developed torque. (Louw, 2010)

$$J = \frac{T_d(\omega) - T_r(\omega)}{\dfrac{d\omega}{dt}} \qquad\qquad (3.2.1.1)$$

When the motor's supply is removed, the developed torque becomes zero and the motor decelerates. The slope of this nonlinear deceleration curve can be step-wised, each of which can be defined as

$$J = \frac{-T_r(\omega)}{\dfrac{d\omega}{dt}} \qquad\qquad (3.2.1.2)$$

Since the motor is running under no-load, the only reaction torque (T_r) responsible for slowing the motor down is due to the friction & windage of the motor which was determined in Section 3.1.3. The reaction torque is therefore calculated from eq. (3.2.1.3).

$$T_r = \frac{P_{fw}}{\omega} \qquad\qquad (3.2.1.3)$$

The measured deceleration curve showing the rotor speed as a function of time is presented in Figure 3.2.1.1.
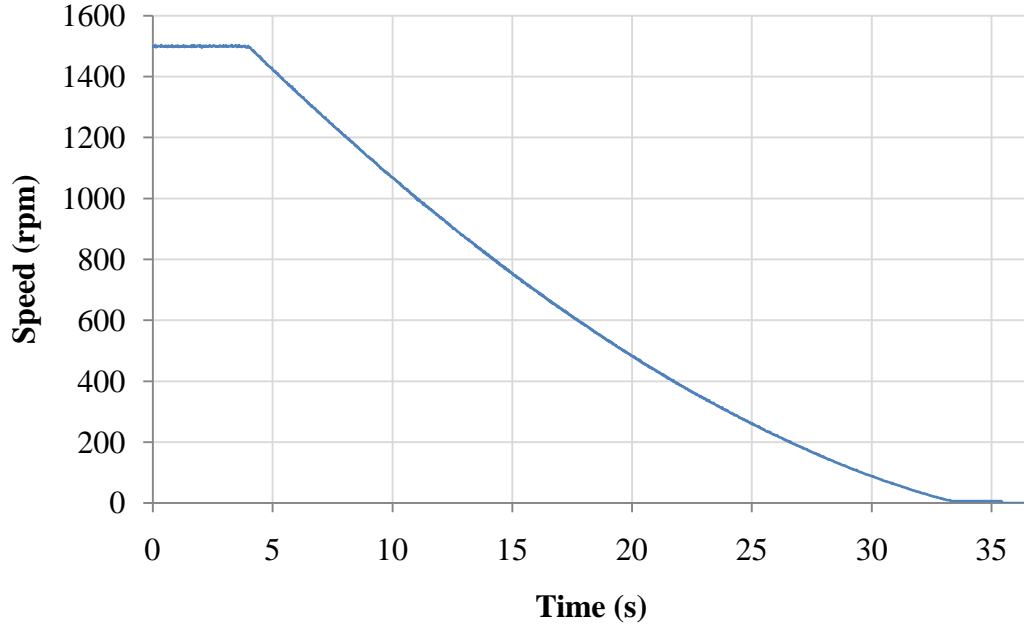
Fig. 3.2.1.1 Speed vs. time deceleration curve

Using (eq. 3.2.1.2) the moment of inertia is calculated to be $J=0.2889$ kgm^2. According to the performance data of a Motorelli datasheet (see Appendix C) this is in the range of a 30kW motor. However, due to the combined weight and friction of the 22kW DC motor's armature, and the 3kW RSM's rotor, this result coincides well with industry values.

3.2.2. Rotor angle calculation in FE

Using an integrated source code in FE, the current angle of the RSM is continuously calculated at each time-step using eq. (3.2.1.1). If the RSM is simulated at the wrong angle, it will increase or decrease the angular displacement in each time-step until equilibrium between T_r and T_d is achieved. The angular velocity is defined as

$$\omega = \frac{d\vartheta}{dt}$$
(3.2.2.1)

and the angular acceleration as

$$\frac{d\omega}{dt} = \frac{d^2\vartheta}{dt^2}$$
(3.2.2.2)

31

Eq. (3.2.1.1) is therefore written in terms of the current angle

$$T_d - T_r = J \frac{d^2 \vartheta}{dt^2}$$
(3.2.2.3)

Referring to eq. (3.2.2.3) it is clear that the rotor would accelerate/decelerate, depending on the difference between the developed (electrical) torque and the reaction torque. Since FE calculates the rotor angle for each time-step, the angle ϑ consequently becomes the subject of the formula. Using a backward difference formula, the derivative for angular velocity is analytically defined as

$$\frac{d\vartheta}{dt} = \frac{\vartheta_2 - \vartheta_1}{t_2 - t_1} = \omega_1$$
(3.2.2.4)

$$\frac{d\vartheta}{dt} = \frac{\vartheta_3 - \vartheta_2}{t_3 - t_2} = \omega_2$$
(3.2.2.5)

The angular acceleration is consequently defined in eq. (3.2.2.6) as

$$\frac{d\omega}{dt} = \frac{\omega_2 - \omega_1}{t_2 - t_1}$$
(3.2.2.6)

$$\frac{d^2\vartheta}{dt^2} = \frac{(\vartheta_3 - \vartheta_2) - (\vartheta_2 - \vartheta_1)}{(t_{n+1} - t_n)^2}$$
(3.2.2.7)

The angles ϑ_1, ϑ_2 and ϑ_3 represent the last three angles – ϑ_3 being the last – that the rotor has moved. The individual time-steps are identical and the equation therefore does not necessitate the third time-step t_3.
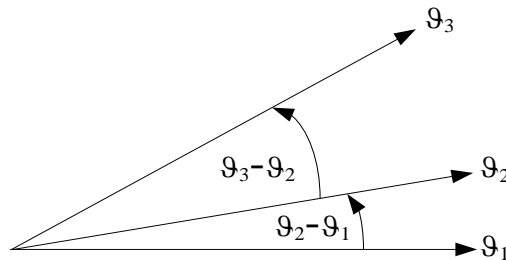

Fig. 3.2.2.1 An example of the rotor angles during acceleration

The resulting angle in the time-step simulation is therefore calculated from eq. (3.2.2.7),

$$\vartheta_3 = \frac{1}{J} dt^2 (T_d - T_r) + 2\vartheta_2 - \vartheta_1 \tag{3.2.2.7}$$

where the inertia, reaction torque and initial two starting angles are user input variables.

3.2.3. Rotor angle acquisition

In synchronous motor theory (Gupta, 2011), the angular displacement between the d-axis and flux linkage space phasor λ_s is determined by load. For an ideal, lossless motor, the d-axis of the rotor and stator reference axis (*a*-phase) coincide at no-load after synchronisation has taken place. At this moment of alignment, the induced emf E across the stator windings is equal to the line voltage V of the supply (eq. 3.2.3.1).

$$I_0 = \left(\frac{V - E}{R_s} \right) \tag{3.2.3.1}$$

The resultant voltage is therefore zero, and hence no stator current (in this example I_0) is drawn from the supply. A change in load, however, causes the rotor to momentarily slow down, and therefore allows the d-axis to slightly fall back in relation to the stator reference axis. This adjustment causes the emf to drop, causing an increase in the supply current.

The angle referred to above is usually known as the torque or power angle and is defined as the angle between the current space phasor and the flux linkage space phasor (Figure 2.1.2). In this study, however, the angular displacement between the current space phasor and the rotor d-axis is measured to obtain the RSM's current angle ϑ. The current space phasor is derived in terms of the three phase currents (eq. 3.2.3.2).

$$i_s = \sqrt{\frac{2}{3}} \cdot \left[i_a \cos \omega t + \alpha i_b \cos(\omega t - 120°) + \alpha^2 i_c \cos(\omega t + 120°) \right] \tag{3.2.3.2}$$

where $\alpha = e^{j120}$.

Using the phase a current i_a as the reference, it is noted that the current space phasor will always have the same angle as the a-phase current angle. The only difference is that the angle of the a-phase current is in the time domain whereas the angle of the current space phasor is in the space domain. For example, $i_a \angle 30°$ in time would be an indication of $i_s \angle 30°$ in space. The physical location of this current space phasor at $\omega t = 0°$ is therefore situated exactly between the remaining two phases, b and c, which represents the magnetic axis of the a-phase, as shown in Figure 3.2.3.1(a). The rotation of this current space phasor is therefore dependant on the angular time displacement of the a-phase current and is consequently an indication of its physical position.

This study therefore records the angular time displacement of the a-phase current and compares it to the physical position of the d-axis. This is achieved by displaying the current waveform on an oscilloscope along with the rotor's incremental encoder output. The encoder produces a $0 - 10V$ output through the rotor's $0 - 360°$ mechanical degrees and displays it as a saw-tooth waveform. Figure 3.2.1.1 illustrates how the current waveform is used to make a comparison to the position of the rotor. The reference point of the current waveform is taken as $i_a = \sqrt{2}I_a \cos \omega t$ when $\omega t = 0°$ or when the current is at a maximum. The encoder output then displays a voltage between $0 - 10V$ to show the deviation from this reference. Figure 3.2.3.1 shows the motor with a current angle of $0°$, where the indices a, b and c represent the distributed windings of the three phases. If the friction and windage losses are negelcted, the RSM will produce zero torque.
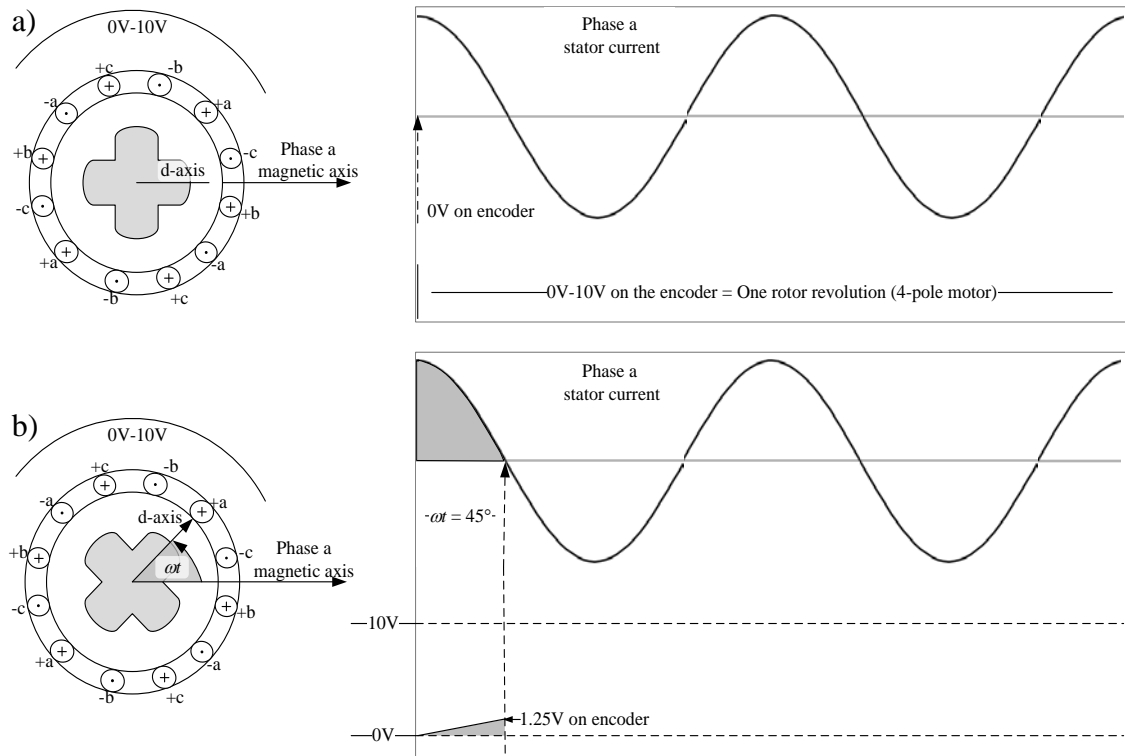
Fig. 3.2.3.1 Phase a current vs rotor angle graph with a current angle of 0° at

(a) $\omega t = 0°$ and (b) at $\omega t = 45°$

In Figure 3.2.3.2, a practical example is given in which the rotor pole is shifted to an angle of 20.3° away from the *a*-phase pole. This illustration is based on measurements taken from the oscilloscope when the motor load on the shaft experienced an average torque of 8.9Nm. The load is simulated by adjusting the DC motor's armature current to a specified amount. Figure 3.2.3.3 represents an axial view of the RSM at the angle represented in Figure 3.2.3.2.
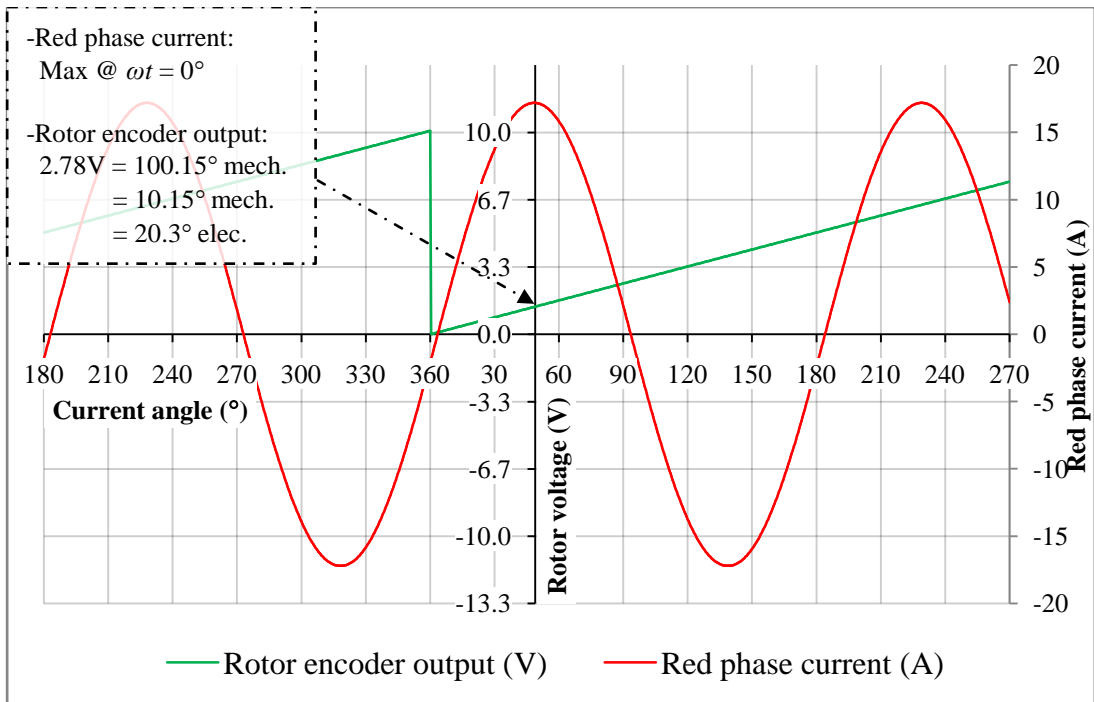
Fig. 3.2.3.2 An example of the current angle acquisition
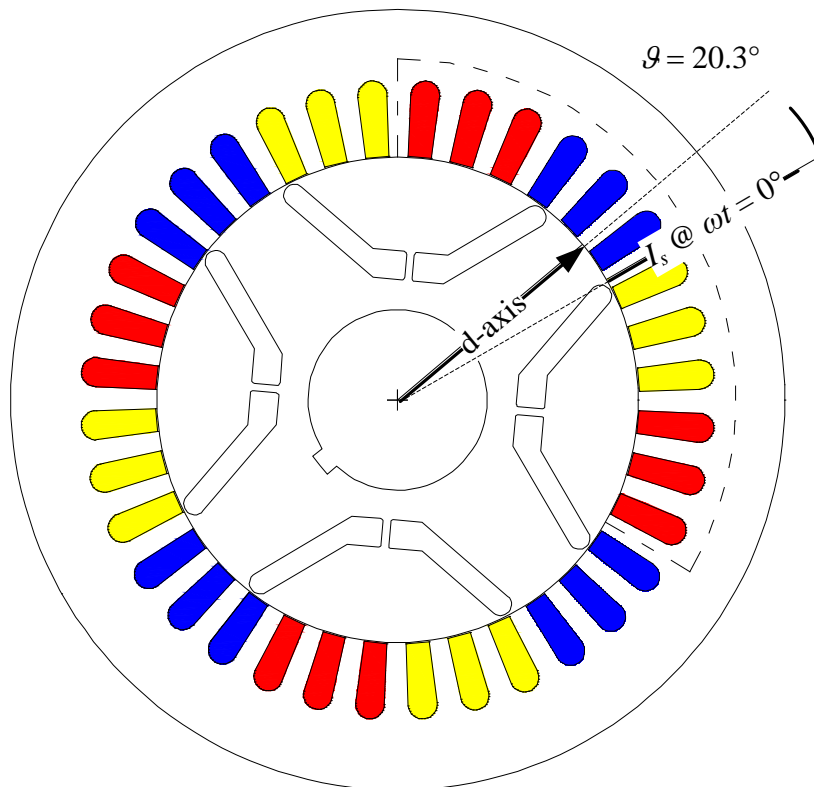
Fig. 3.2.3.3 Representation of RSM at $\vartheta = 20.3°$

With reference to Figure 3.2.3.3 it should be noted that this is the position of the rotor when the *a*-phase current is at a maximum. The current space phasor therefore continues to rotate along with the rotor, whilst maintaining an electrical angle of 20.3° between the two axes. It is important to know the position of the rotor relative to the stator's waveform in order to simulate these results with FE software. The acquired current angles for the various case studies are therefore recorded for different values of load torque. The parameters necessary for the comparison are displayed in Section 4.

4. The Voltage- and Current-fed RSM Measurements

The test bench consists of a RSM having the same specifications as used in the FE simulation. By definition, the voltage-fed RSM is not controlled in any way and runs from the frequency and voltage supplied by the network. It is therefore started and driven to its synchronous speed using an external DC motor (Figure 4.1). Once the motor has reached its synchronous speed of 1500rpm, it will be switched onto a sinusoidal voltage which will, in turn, drive the motor from that point onwards. The method of starting the RSM, however, is of no particular importance to this thesis, as only the RSM's operation under constant voltage supply is considered.
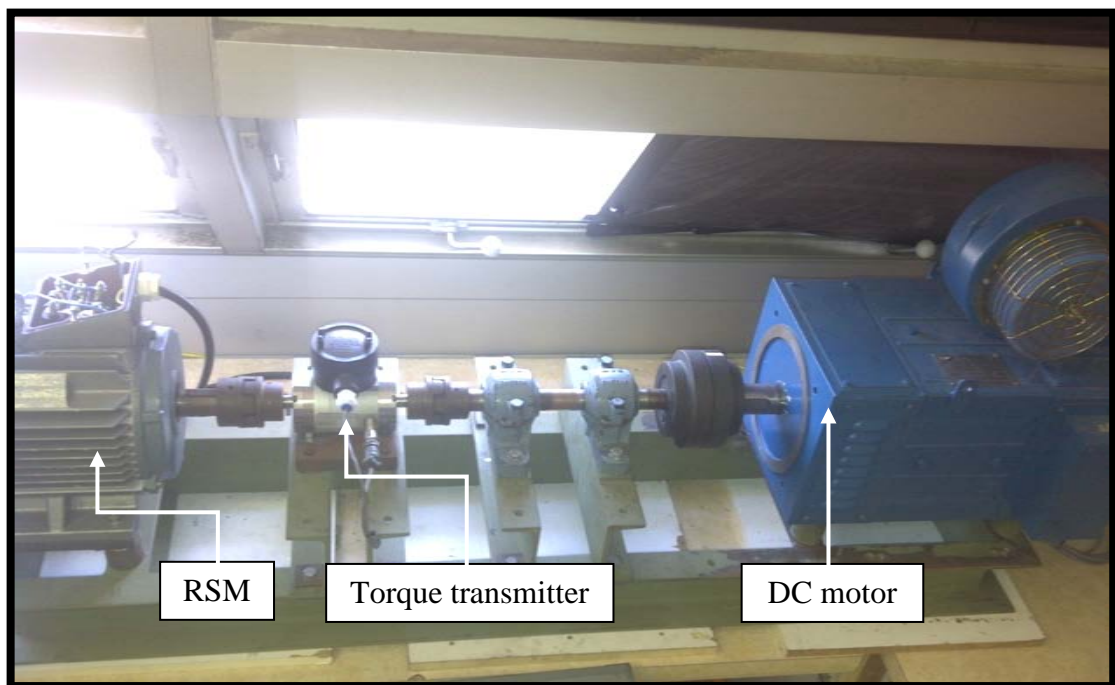
Fig. 4.1 (Left to right) Top view of RSM, torque sensor and DC motor (load)

The current-fed RSM, however, is controlled with a sensorless vector drive (Figure 4.2) which operates similar to the voltage-fed method, but uses a torque-current estimator technique to control the amount of flux in the air gap. This method is achieved by altering the voltage magnitude and the angle between the voltage and current. Hence, the current is controlled according to the load requirements. A schematic wiring diagram of the RSM drive can be seen in Appendix D along with the schematic diagram of the test bench.
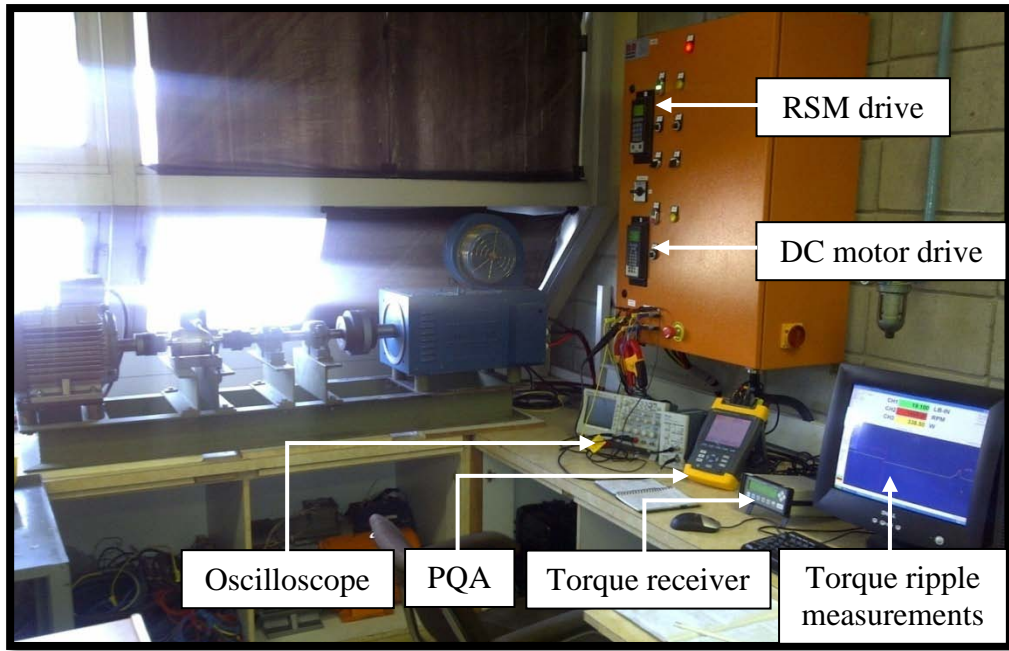
Fig. 4.2 Test bench layout including measurement equipment

The RSM's input power (P_{in}), power factor (PF), rms voltage (V_{red}), and rms current (I_{red}) are measured with a power quality analyser (PQA) as shown in Figure 4.3. The current angle ϑ is measured with an incremental encoder (Figure 4.4) which is then displayed on a 200MHz oscilloscope. The average torque (T_{avg}) and percentage torque ripple ($\%T_{rip}$) are measured using a torque transmitter.
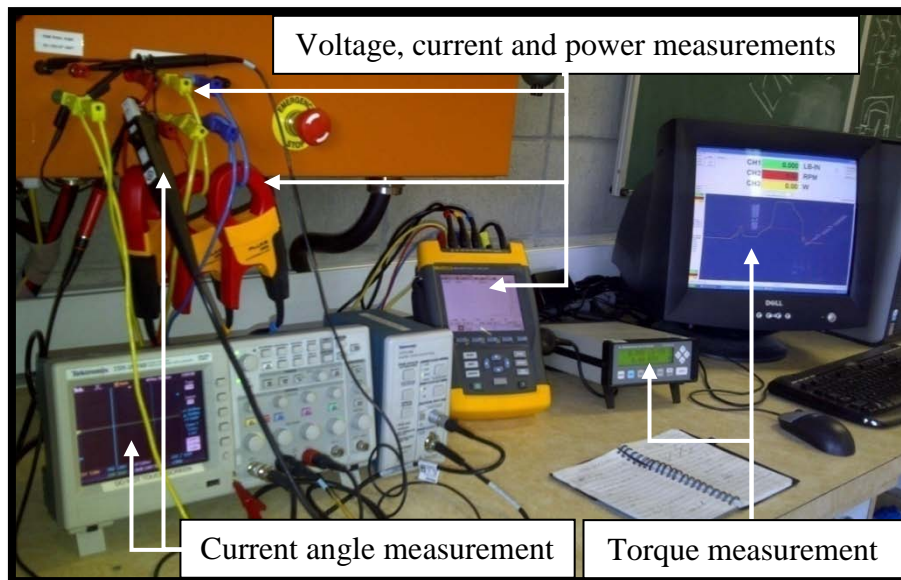
Fig. 4.3 Test bench measurement equipment

The motor's various load conditions are obtained through a 22kW DC motor which is controlled by a four-quadrant DC-drive (Figure 4.2). The measured results are taken for loads varying from no-load to 150% of full-load. The full-load setting (100%) is defined as the full rated output power of the motor. In this case, a full-load motor has an output power of 3kW. The measurements in this study are therefore taken up to 4.5kW (28.65Nm). These loads are varied by adjusting the DC-drive's current limiting capability, allowing the DC motor to deliver the exact amount of reaction torque needed to obtain the desired results.
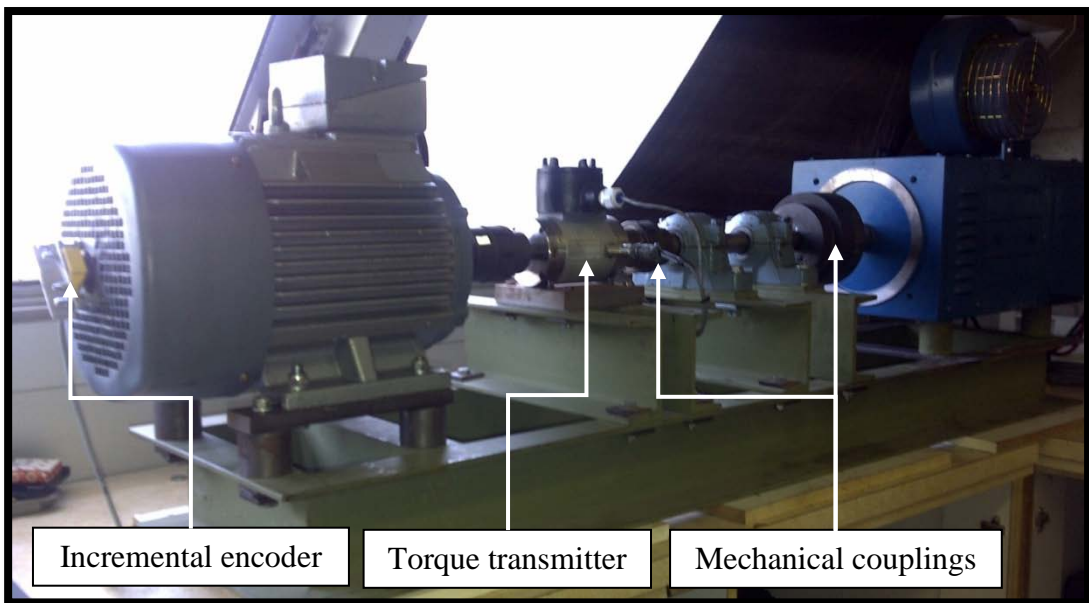
Fig. 4.4 (Left to right) Encoder, RSM, torque transmitter and DC motor (load)

4.1. Torque

In addition to not having any starting torque, the voltage-fed RSM also has a fairly low pull-out torque when compared to the current-fed RSM. This is a great disadvantage for the voltage-fed RSM in terms of its practicality in industry.
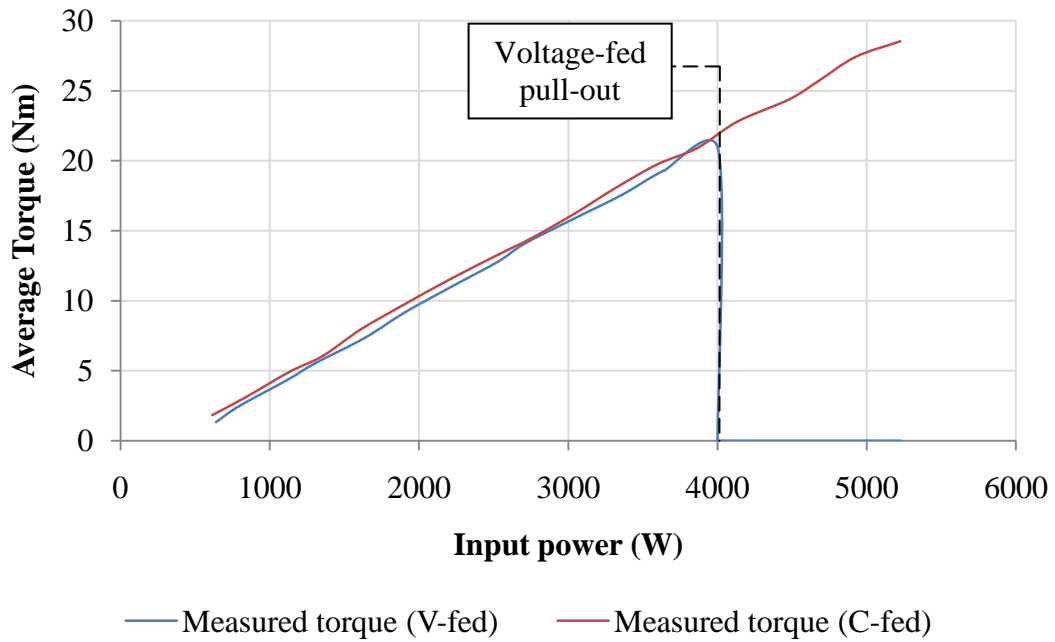
Fig. 4.1.1 Average torque comparison vs. input power

Referring to Figure 4.1.1 it can be seen that the maximum steady output torque (pull-out torque) of the voltage-fed RSM is around 21Nm, while the current-fed RSM is still able to produce 150% of its full-load output power. Figure 4.1.2 represents the instantaneous torque of the voltage-fed RSM when the load is slightly increased to 22.5Nm. The torque, represented as a function of time, shows that the motor pulled out of synchronism in less than 35s.
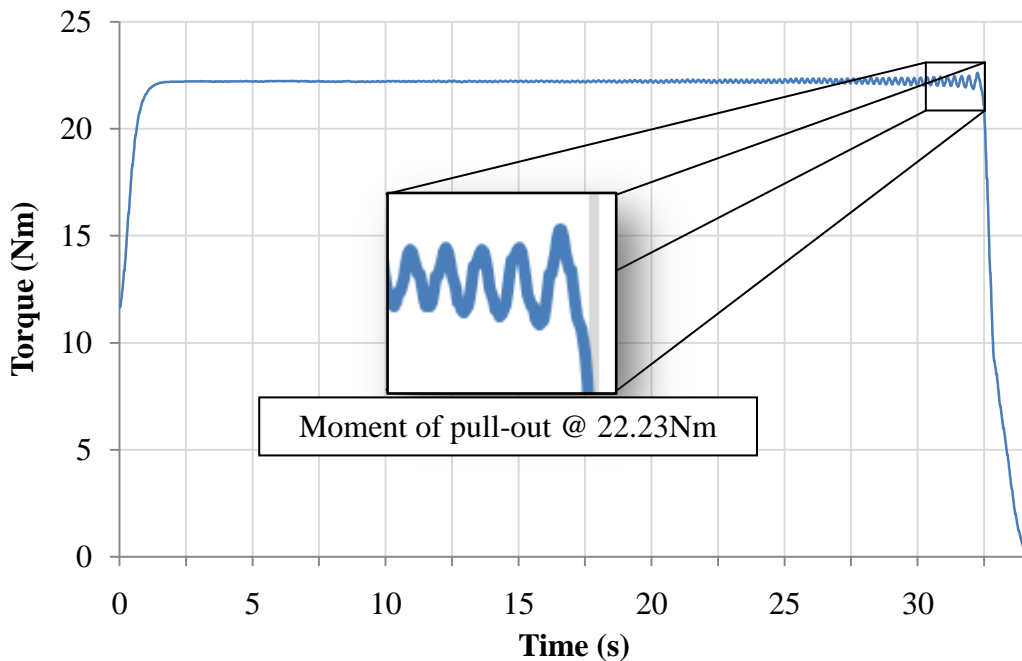
Fig. 4.1.2 Torque waveform of voltage-fed RSM at 22.23Nm

41

4.2. Torque ripple

The torque ripple is defined as the "deviation of the minimum and maximum torque from the average value" (Hanekom, 2006) and is a result of the rotor asymmetry in the RSM, preventing the electromagnetic field in the air gap from distributing uniformly. Excessive torque ripple can produce vibrations, causing unnecessary mechanical wear. It therefore becomes an important performance criteria to establish the percentage torque ripple, expressed in eq. (4.2.1) as

$$\% T_{rip} = \frac{T_{max} - T_{min}}{T_{avg}} \times 100\% \qquad (4.2.1)$$

where T_{max}, T_{min} and T_{avg} are the maximum, minimum and average torque of a measured torque waveform. Figure 4.2.1 represents the torque ripple as a function of the output torque. From this graph it can be seen that the voltage-fed RSM provides less measurement data due to the aforementioned pull-out torque.
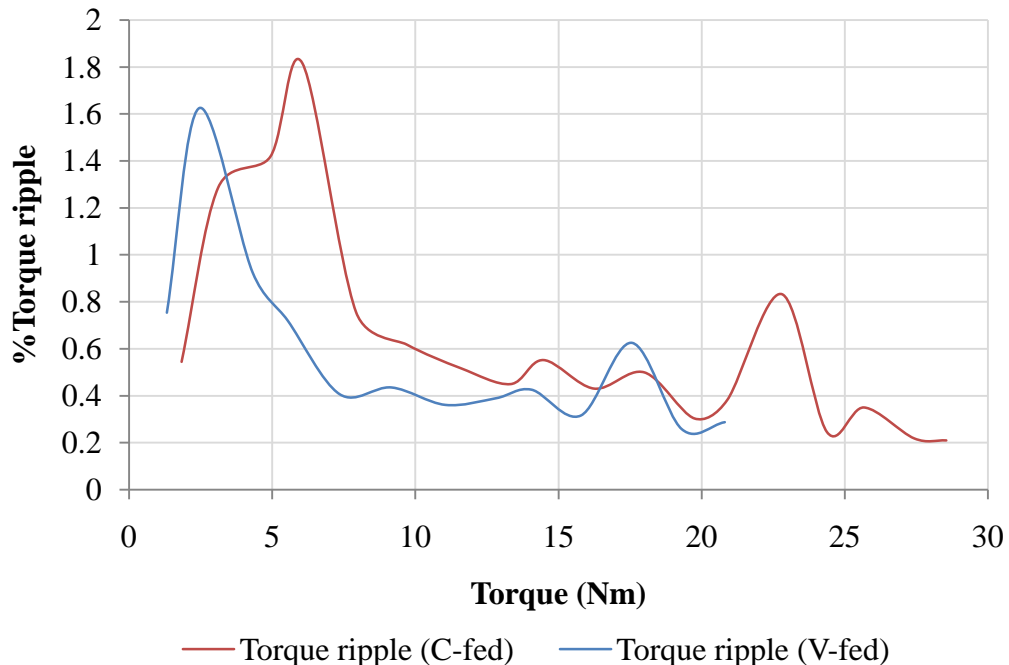
Fig. 4.2.1 Percentage torque ripple comparison vs. output torque

With the exception of two instances (at lower loads and at 17.5Nm) the voltage-fed RSM produces slightly lower values in torque ripple. According to Hwang (1994) a

higher torque ripple is expected for RSMs at lower loads. It should be noted that the torque ripple values measured in this study are different from those in other FE studies (Hanekom, 2006) (Smith, 2010) (Heyns, 2011) although the same motor was used. The reason for this is partly due to the fact that the RSM used in this study is connected to a DC motor load using various couplings which act as dampers.

4.3. Voltage, current and power factor

The voltages and currents are shown in Figure 4.3.1 to highlight the consistent differences between the two modes of operation. It is clear that, while the two motor's currents remain fairly close to each other, the voltage for the current-fed RSM is consistently higher. This is due to the PWM voltage selected by the drive in order to control the RSM as accurately as possible. It is also interesting to find an increase in the voltage-fed RSM's current/torque rate of change after 15Nm.
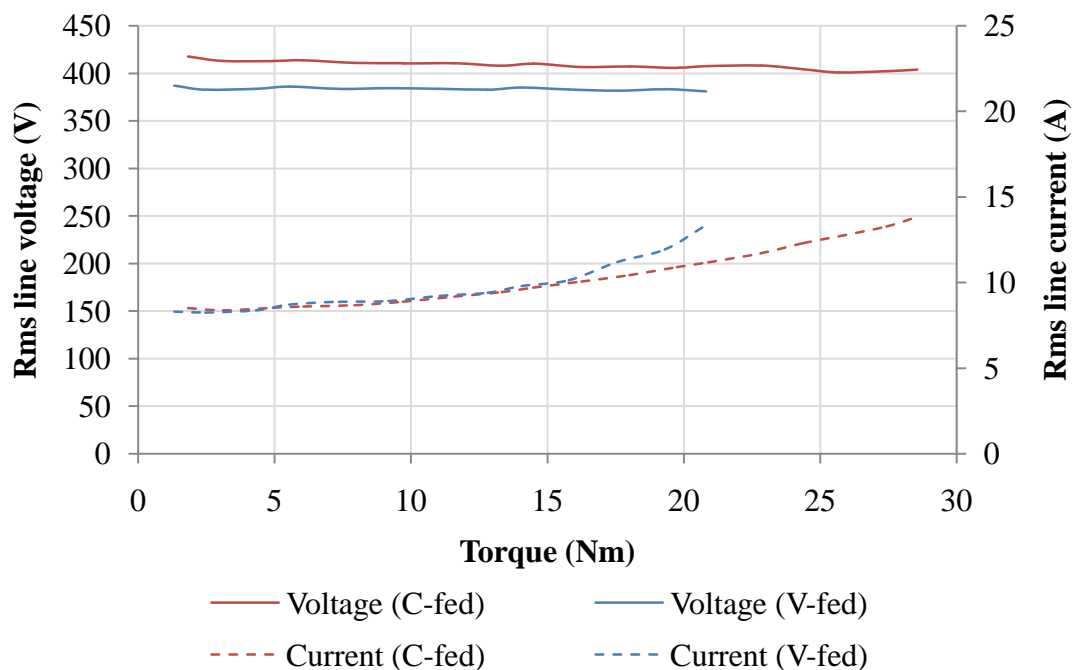
Fig. 4.3.1 Current and voltage comparisons vs. output torque

The current-fed RSM, however, maintains a steady supply of current increase to the stator as part of its torque per ampere functionality. The rate of change for the

voltage-fed RSM's power factor vs. torque graph, however, shows an opposite behaviour in Figure 4.3.2 when compared to that of Figure 4.3.1.
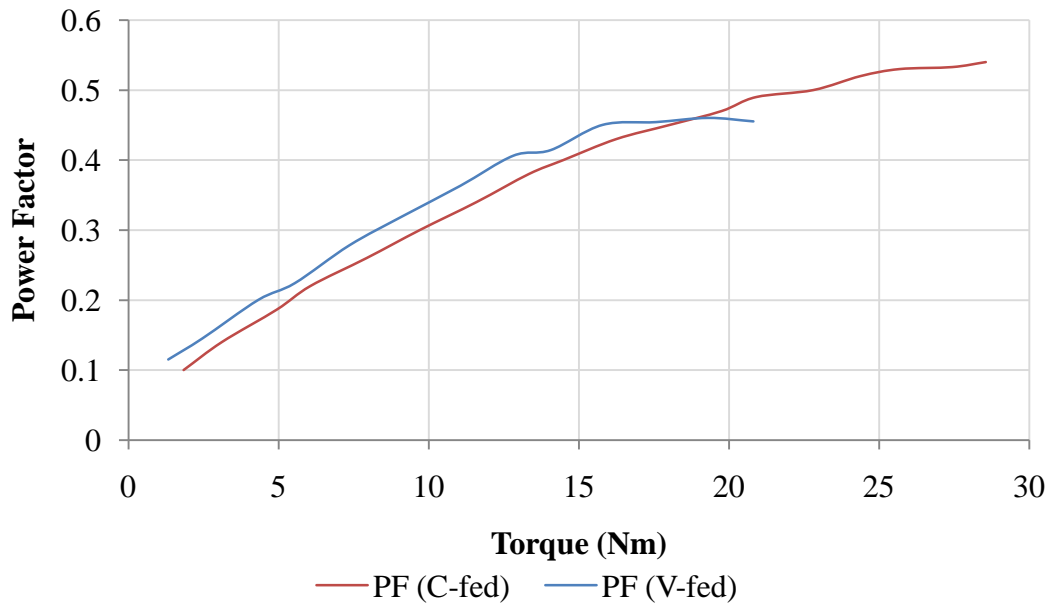
Fig. 4.3.2 Power factor comparison vs. output torque

The results seen in Figures 4.3.1 and 4.3.2 are clear examples of the voltage-fed RSM's shortfall in terms of its control and provide an insight into the motor's inevitable pull-out.

4.4. Efficiency

In addition to the voltage-fed RSM's low pull-out torque, another disadvantage is found in terms of its efficiency, displayed in Figure 4.4.1.
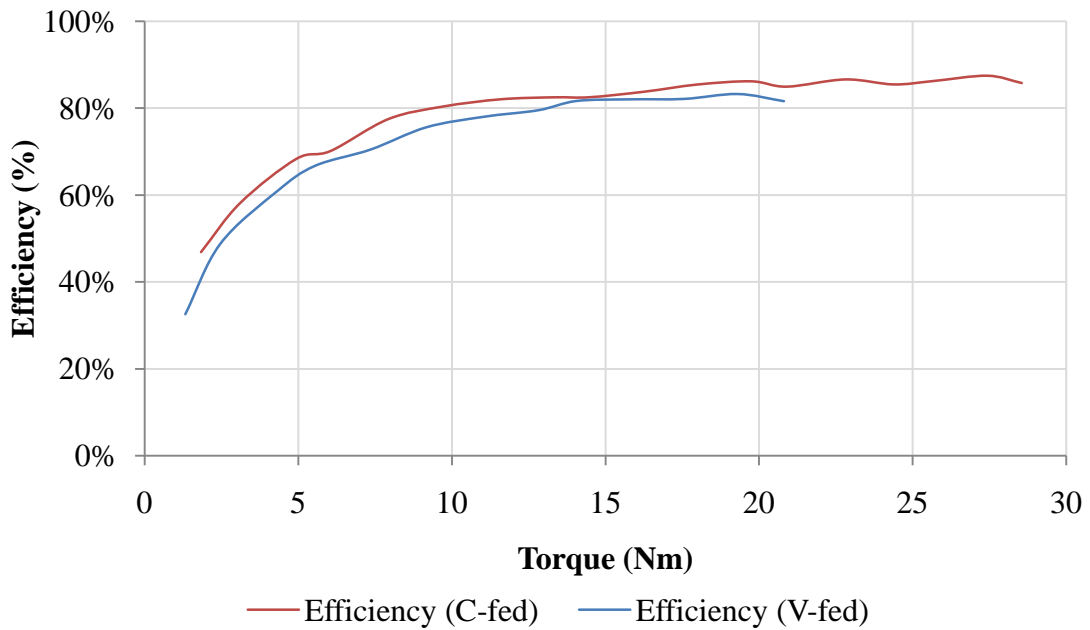
Fig. 4.4.1 Efficiency comparison vs. output torque

It is interesting to realise that the voltage-fed RSM has a 4% overall lower efficiency than the current-fed RSM. The reason for this behaviour is not verified, but it is believed to be due to the fact that the current-fed RSM's PWM voltage produces a higher rms voltage across the windings than that of the voltage-fed RSM, supplied by the utility.

4.5. Current angle

The current angle is measured for both the voltage- and current-fed RSM, using the incremental voltage encoder (Section 3.2.3). The current angle is naturally selected by the motor as the different loads are applied. In Figure 4.5.1 it can be seen that, for both the voltage- and current-fed RSM, the d-axis moves further away from the reference axis as the load is increased. It is also interesting to note how the current-fed RSM's current angle remains fairly constant in the initial increase in applied load and then gradually lags a few degrees behind the voltage-fed RSM's current angle. This deviation is a result of the torque-current estimator technique which controls the amount of flux in the air gap for the current-fed RSM.
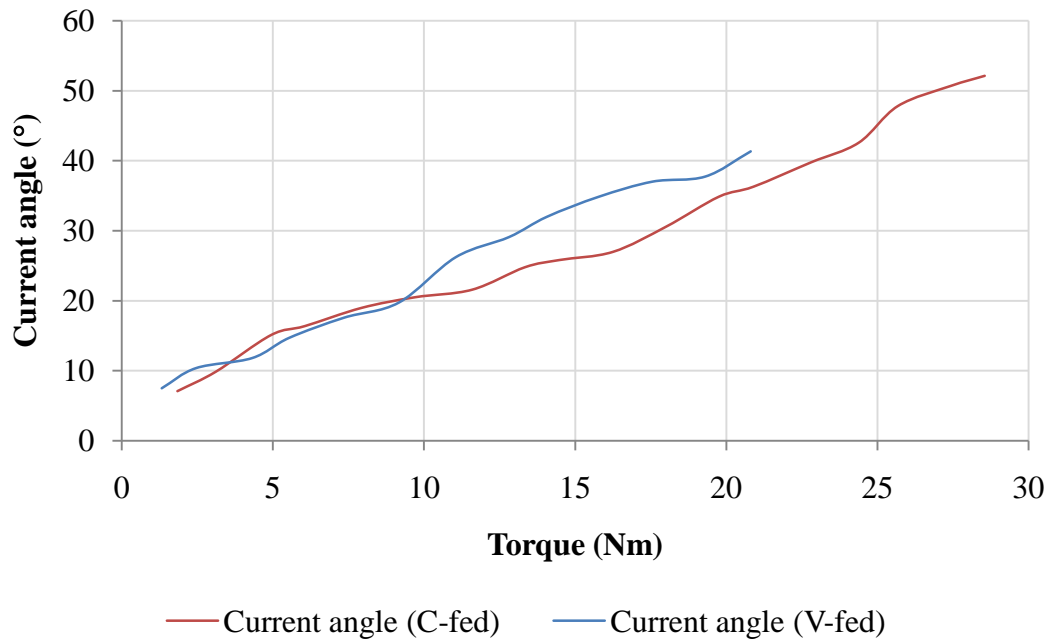
Fig. 4.5.1 Current angle measurements as a function of the output torque

It should be noted that the nonlinearity of the two curves are due to distortions in the output current and encoder voltage causing slight errors in the results. The distortions are partially due to the resolution of the oscilloscope's output (Figure 4.5.2) as well as the output encoder's insufficient bit-rate frequency.
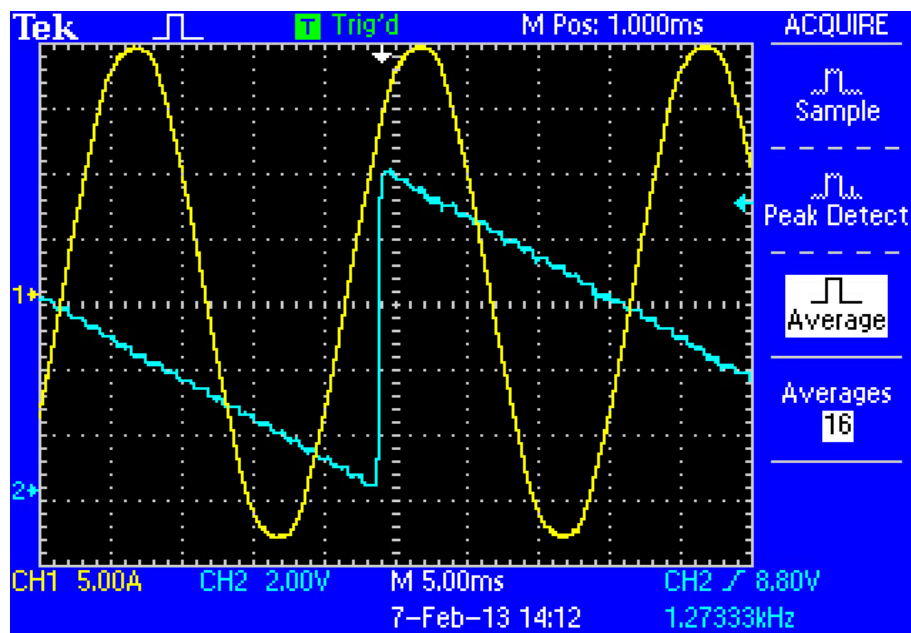
Fig. 4.5.2 Oscilloscope screenshot for current angle measurement

However, the oscilloscope and encoder's drawback is partially overcome by exporting the measured data to a spreadsheet for further analysis. Using a trend-line function, the encoder voltage and measured current are fitted to linear and polynomial equations (Figure 4.5.3). The encoder voltage is consequently calculated when the current waveform is at a maximum (refer to Section 3.2.1).
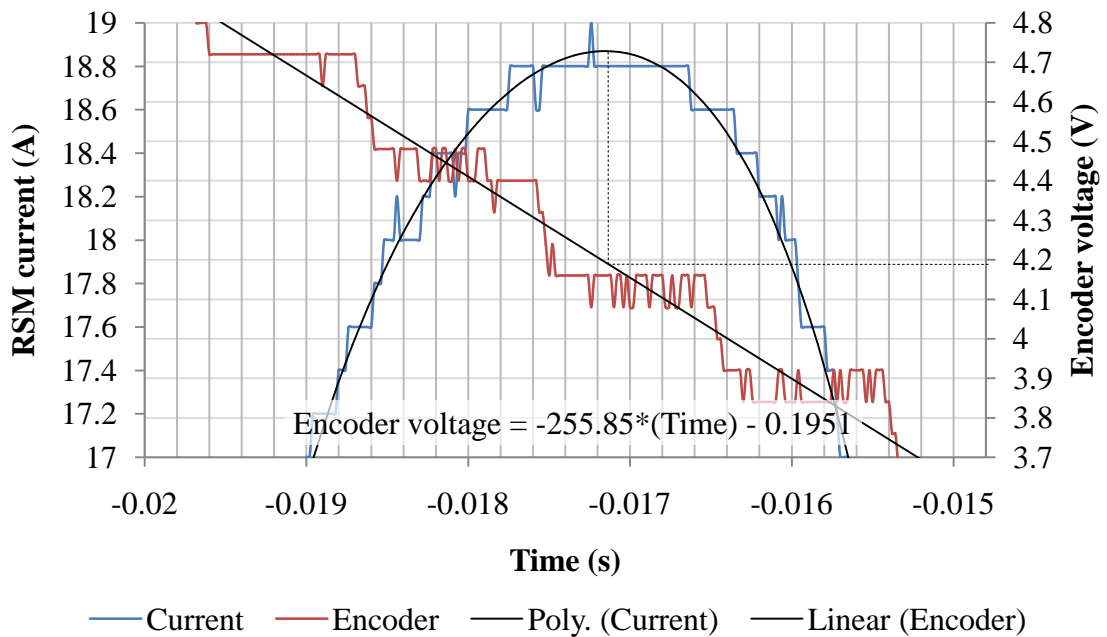
Fig. 4.5.3 Linear and polynomial extrapolation of measured current angle

4.6. D- and q-axis currents

With the current angles known, it is now possible to determine the change in d- and q-axis current components using eq. (2.1.2.1) and (2.1.2.2). Referring to Section 2.1 it is clear that these parameters play an important role in the overall performance of the RSM. It is therefore necessary to establish the differences between the voltage- and current-fed RSM's d- and q-currents.
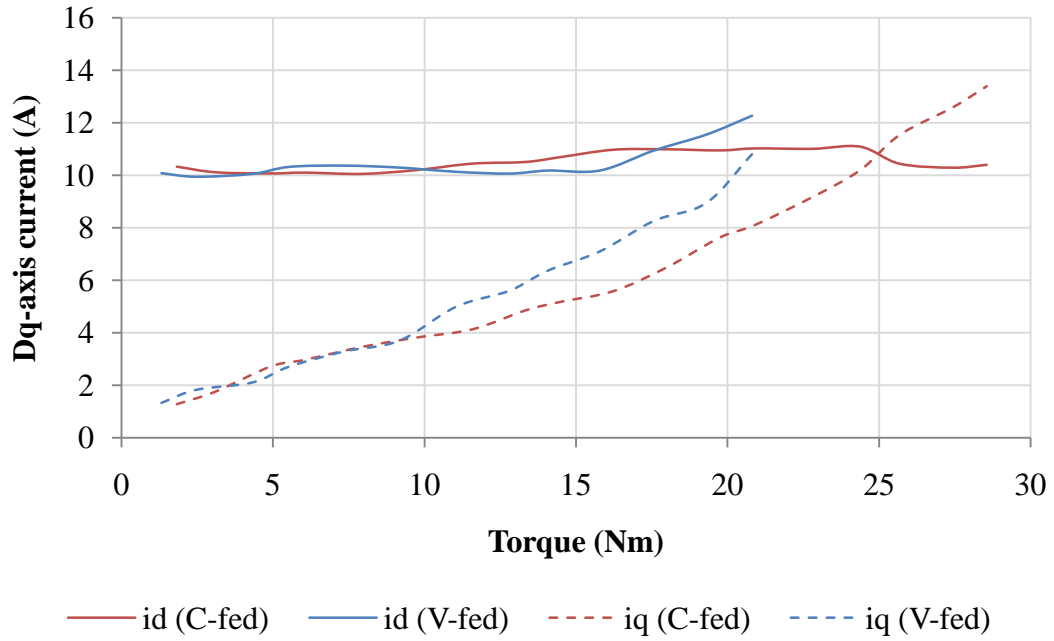
Fig. 4.6.1 D- and q-currents comparison vs. output torque

The voltage- and current-fed's d- and q-currents are relatively in agreement up until approximately 10Nm. After this point, the voltage-fed RSM's q-axis current tends to rise faster than that of the current-fed RSM, while the two d-axis currents remain fairly constant. From Figure 4.6.1 it can be seen that the current-fed RSM's d- and q-currents are controlled and maintained more efficiently when compared to those of the voltage-fed RSM. The current-fed RSM's d- and q-current curves tend to have smoother variations with the change in current angle.

5. The Voltage- and Current-fed RSM in FE

A general method of simulating a vector-controlled drive in FE is adapted in this section. This is achieved by assigning a sinusoidal current source to each of the RSM's slots (Kim & Ryu, 2012). These are then used to calculate the magnetic vector potential which is generated on a time-step basis as the rotor mesh is rotated.

This 2D approach is also used for the voltage-fed RSM, but is simulated using all the motor's individual voltage drops to account for the RSM's overhang. The mathematical model for the voltage-fed RSM is based on field, circuit, and mechanical motion equations. The field equations are used to describe the active region of the RSM (Section 2.2), which is defined as the entire length of the motor, excluding the end-windings. Neglecting the leakage flux caused by fringing on the motor ends, this active region is responsible for creating the torque. The end regions of the stator windings are modelled using the equivalent circuit determined in Section 3.1. The FE software also simulates the voltage-fed RSM through discrete time-steps, but calculates every new rotor position using the mechanical motion equations, as seen in Section 3.2.2.

An important part of the preparation for modelling the RSM is establishing that the appropriate *B-H* curve is being used for the model. Referring to the datasheet in Appendix E, it can be seen that the manufacturer's data is only taken up to a flux density of 1.8T. Since the region up to and beyond saturation is an important factor in the modelling procedure, a method has been proposed in Appendix F, in which the *B-H* data is extrapolated to around 3T using the Law of Approach.

The purpose of this chapter is not only to confirm the measured results (efficiency, torque and measured inductance), but also to perform a deeper analysis on the voltage- and current-fed RSM. The calculated flux linkages and inductances are converted to their respective d- and q-components to calculate and confirm performance parameters, such as efficiency, pull-out torque, and the various angles explained in Section 2.1. Additional parameters such as harmonics and core loss are also calculated.

5.1. Validating the accuracy of the FE model

One of the objectives of this study is to find an acceptable coherency between the measured and simulated results for both the voltage- and current-fed RSM. This coherency is shown by calculating the percentage error between the measured and simulated results (eq. 5.1.1).

$$\% \varepsilon = \frac{1}{n} \sum_{i=1}^{n} \left(\frac{i_m - i_s}{i_m} \right)^2 \cdot 100\% \tag{5.1.1}$$

This error calculation uses the square of the difference between the sum of the measured values (i_m) and the sum of the simulated values (i_s) to find the percentage error over the whole range of values (Nie *et al.*, 2008).

5.1.1. Inductance (excluding saturation)

The inductance of the rotor is measured at standstill by aligning the d-axis with the magnetic axis of the *a*-phase. Measurements are then taken in steps of 5° until the q-axis is aligned with the *a*-phase magnetic axis. This process is then repeated in FE. It should be noted that the stator windings are measured at low voltage so that the iron does not saturate. The RSM is therefore simulated with a linear *B-H* curve, with the core having a relative permeability of 3300. Figure 5.1.1 shows the change in inductance as a function of the mechanical angle between the d-axis and the *a*-phase magnetic axis.
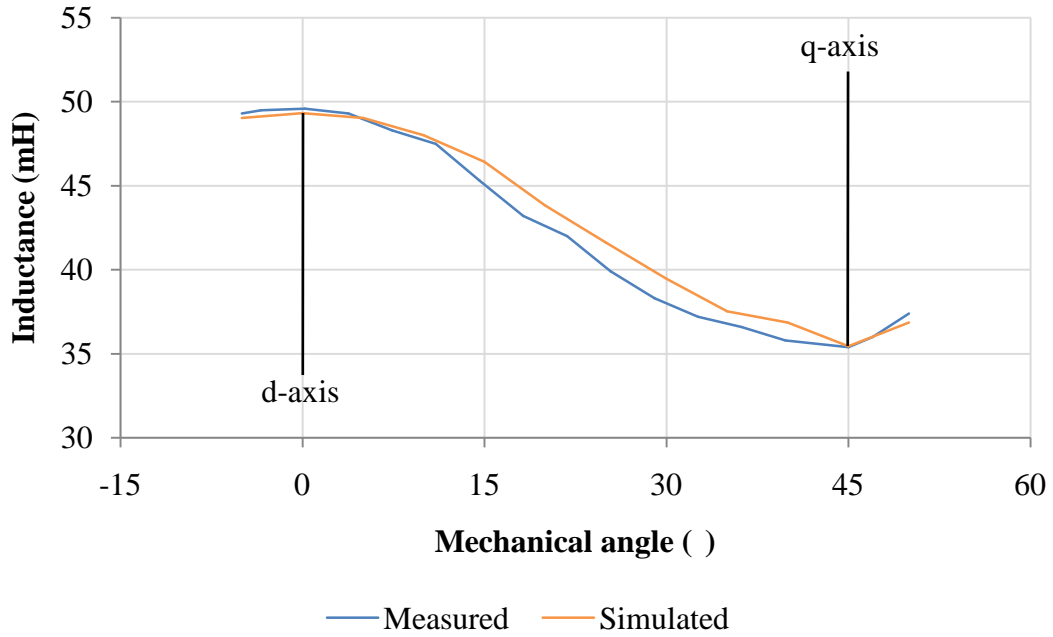
Fig. 5.1.1.1 Inductance measurement and simulation comparison for d- and q-axis

Looking at Figure 5.1.1.1, it is clear that the locked rotor inductances for measured and simulated values are in close agreement, with an error of 0.05% calculated according to eq. (5.1.1). The saliency ratio plays an important role when determining parameters such as torque and power factor. It is therefore important to ensure that these fundamental values are in agreement in order to validate the FE model's accuracy. This method, however, is not yet fully sufficient, and therefore further measured and simulated comparisons follow in the subsequent sections.

5.1.2. *Torque*

The developed torque produced by the RSM is calculated using the MST method (see Section 2.1, eq. 2.1.4.5) in which the normal and tangential flux density components in the air gap are used to model the instantaneous torque for each individual time-step. The average torque for the calculated and measured values is shown as a function of the input power for the voltage-fed (Figure 5.1.2.1.a) and the current-fed (Figure 5.1.2.1.b) RSM.
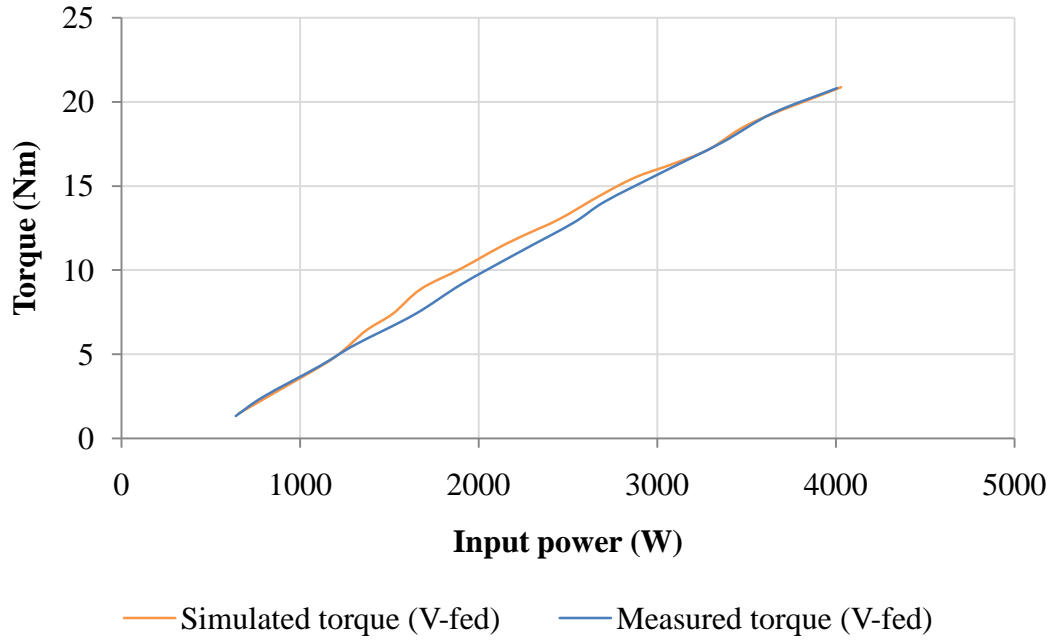
Fig. 5.1.2.1(a) Simulated and measured torque for voltage-fed RSM
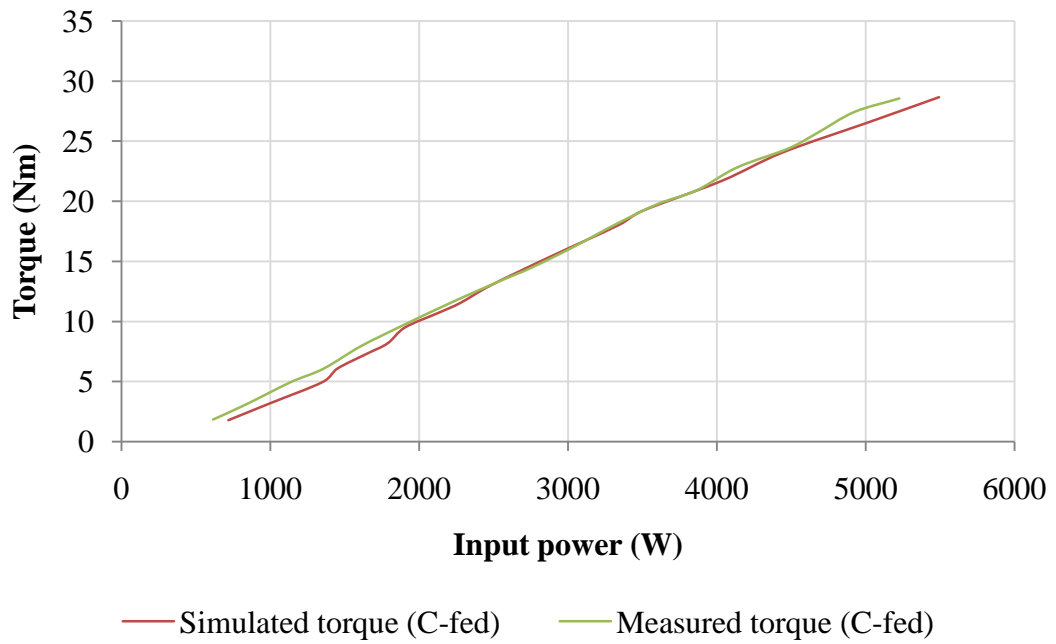
Fig. 5.1.2.1(b) Simulated and measured torque for current-fed RSM

From Figure 5.1.2.1(a) and (b), it is clear that the measured and simulated values of torque correspond very well. Using eq. (5.1.1) the average errors are 0.41% and 1.11% respectively.

5.1.3. Efficiency

To further establish the accuracy of the FE model with the measured results, the RSM's efficiency is compared. This is a reliable method as it encompasses all the remaining fundamental parameters. These parameters include:

- output torque (T),
- angular velocity (ω),
- rms line voltage (V_L),
- rms line current (I_L), and
- power factor ($cos\varphi$)

and is calculated according to eq. (5.1.3.1).

$$\%\eta = \frac{P_{OUT}}{P_{IN}} \cdot 100\% = \frac{T\omega}{\sqrt{3}V_L I_L \cos\varphi} \cdot 100\%$$

(5.1.3.1)

The power factor is calculated according to eq. (2.1.3.7), Section 2.1.3 which consists of d- and q-axis inductances and currents, therefore making it a good indicator of the level of accuracy required. The motor's efficiency is compared for both the voltage- (Figure 5.1.3.1 a) and current-fed motor (Figure 5.1.3.2 b).
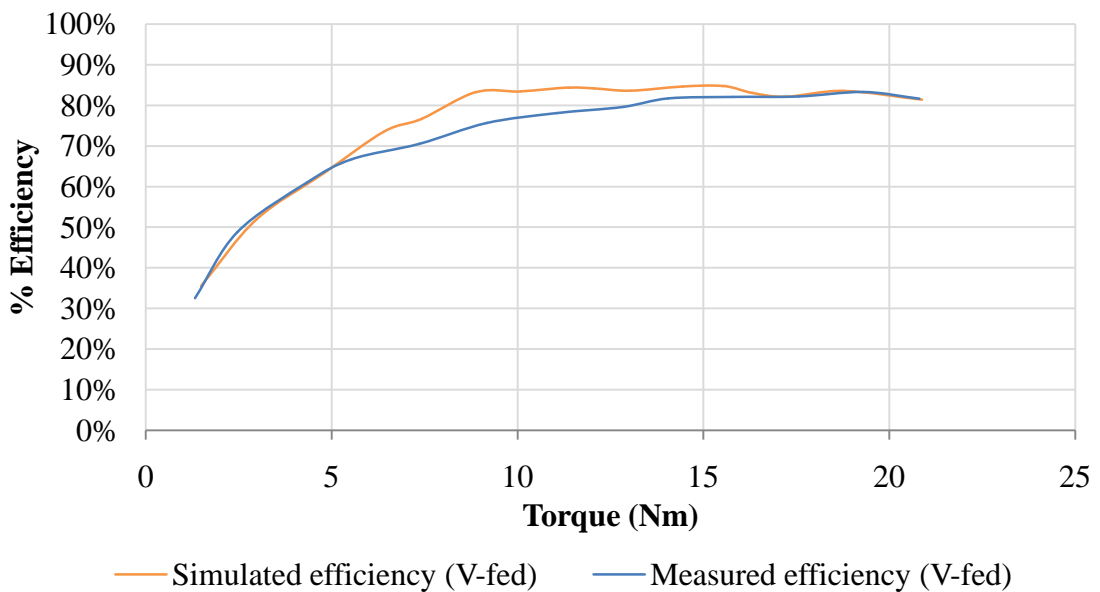
Fig. 5.1.3.1 (a) Simulated and measured efficiency vs. torque for voltage-fed RSM
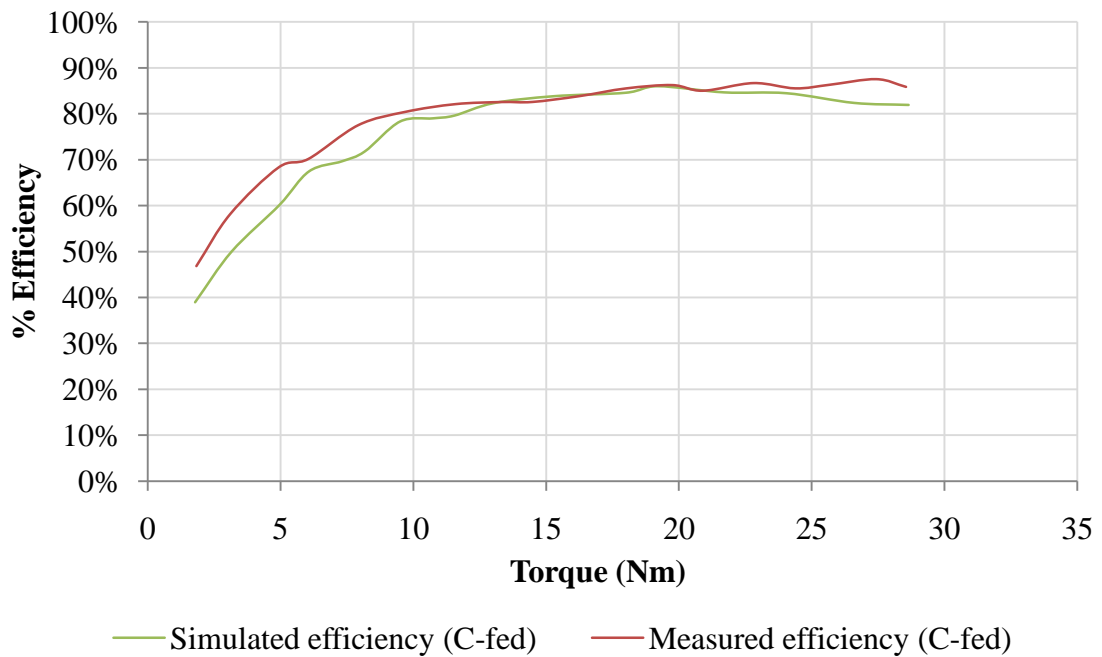
Fig. 5.1.3.1 (b) Simulated and measured efficiency vs. torque for current-fed RSM

The percentage errors for Figure 5.1.3.1 (a) and (b) are 0.24% and 0.79% respectively.

5.2. Inductance (including saturation)

Since the fundamental parameters from the previous section for the measured and simulated values only deviate by a maximum of 0.52%, a certain degree of accuracy can now be assumed and consequently the inductances, calculated from the FE values, can now be used as a reliable indication of the RSM's true inductance. The RSM, simulated with the nonlinear *B-H* curve, causes the iron to saturate at certain regions in the core (Figure 5.2.1). As the load torque is increased, the angle between the d-axis flux linkage and space phasor flux linkage increases and the space phasor starts to move closer to the q-axis. As the q-axis flux linkage increases with the load, it becomes more exposed to an increasing flux density. The flux density consequently saturates the ends of the rotor flux barriers. These saturated regions affect the permeability of the steel causing it to become close to that of air (see Appendix F for *B-H* curve). This effectively decreases the overall inductance in the rotor's q-axis. It is for this reason that the d- and q-axis inductances do not correspond to the results

shown in Figure 5.1.1.1, and this signifies the importance of torque production as the saliency ratio increases due to the q-axis saturation.
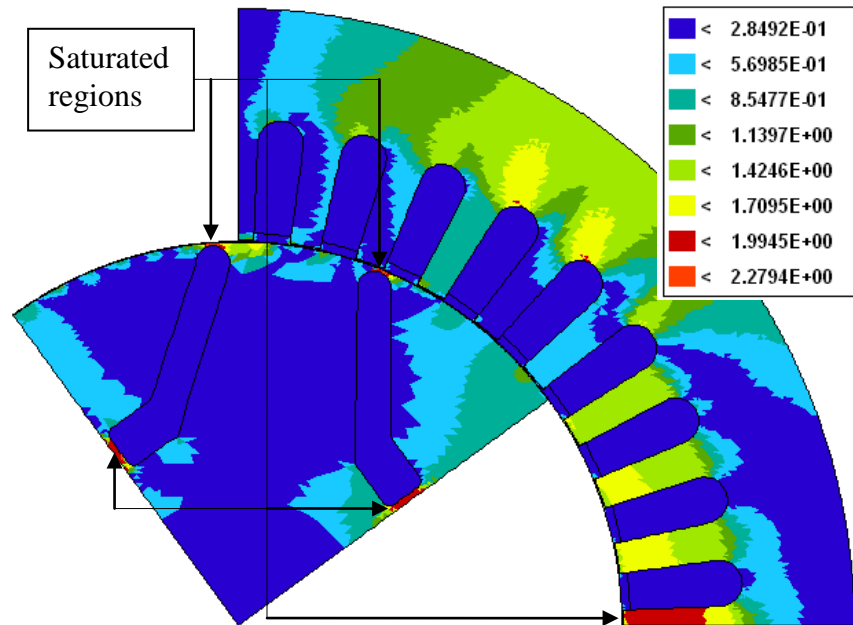
Fig. 5.2.1 Flux density mapping of a quarter RSM

The inductances are calculated from the RSM's flux linkages and currents in the three stator phases and are transformed into their respective d- and q-components by using Park's transformation (Section 2.1, eq. 2.1.1). It is for this reason that the inductance measured in Figure 5.1.1.1 will be different to that calculated in Figure 5.3.2. The inductance measured in Figure 5.1.1.1 was only measured on the stator's *a*-phase with no influence from the adjacent phases, while the calculated d- and q-axis inductance in Figure 5.3.2 is a result of all three stator phases. Figure 5.3.2 represents the inductances of the voltage-fed RSM as a function of the torque.
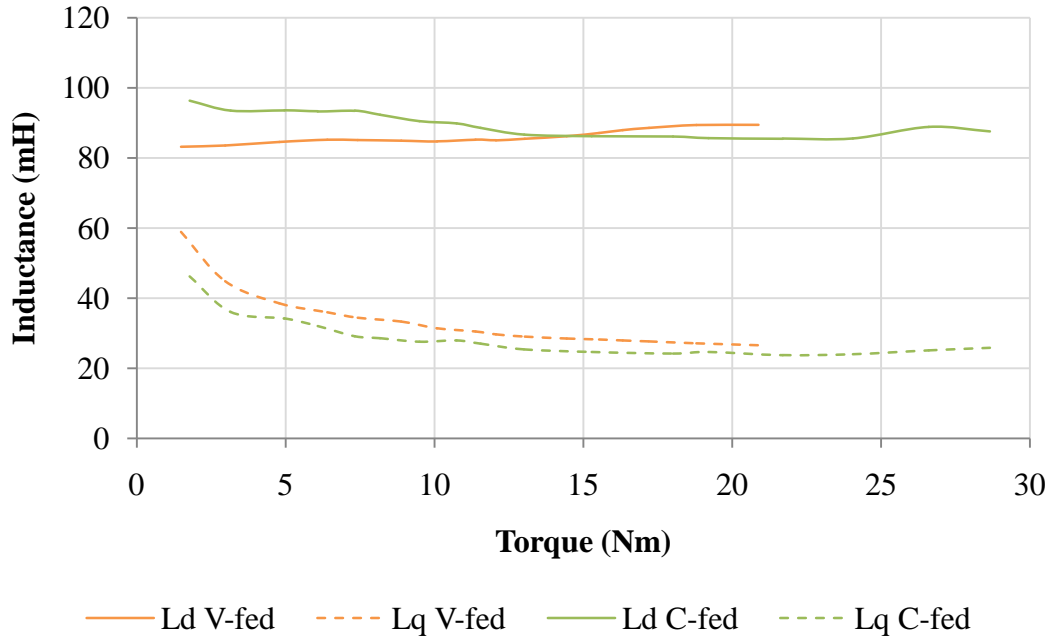
Fig. 5.2.2 D- and q-axis inductance comparison vs. output torque

It is clear that, for the lower values of load torque, the current-fed RSM is inclined to operate at higher d-axis inductance values, as well as a larger $L_d – L_q$ difference. This effect can be explained by the measured voltages in Figure 4.3.2, which show how the current-fed RSM operates at a naturally higher voltage than that of the voltage-fed RSM. Another noticeable difference is the d-axis inductance for the voltage-fed RSM. In comparison with the current-fed RSM's slight decrease in d-axis inductance, the voltage-fed RSM's inductance tends to rise with the load increase. This inconsistency is due to the manner in which the two RSMs were simulated. For the current-fed RSM, the input variables consisted of an rms current (Section 4.3) as well as the applied load, while for the voltage-fed RSM, only the applied load was varied while the voltage was kept constant (slight voltage deviations can be neglected in this case). The FE software was therefore able to calculate the voltage-fed RSM flux linkages from a constant voltage source, without the intervention of any external parameters, explaining the steady decrease in d-axis flux linkage (Figure 5.2.3) for this RSM.
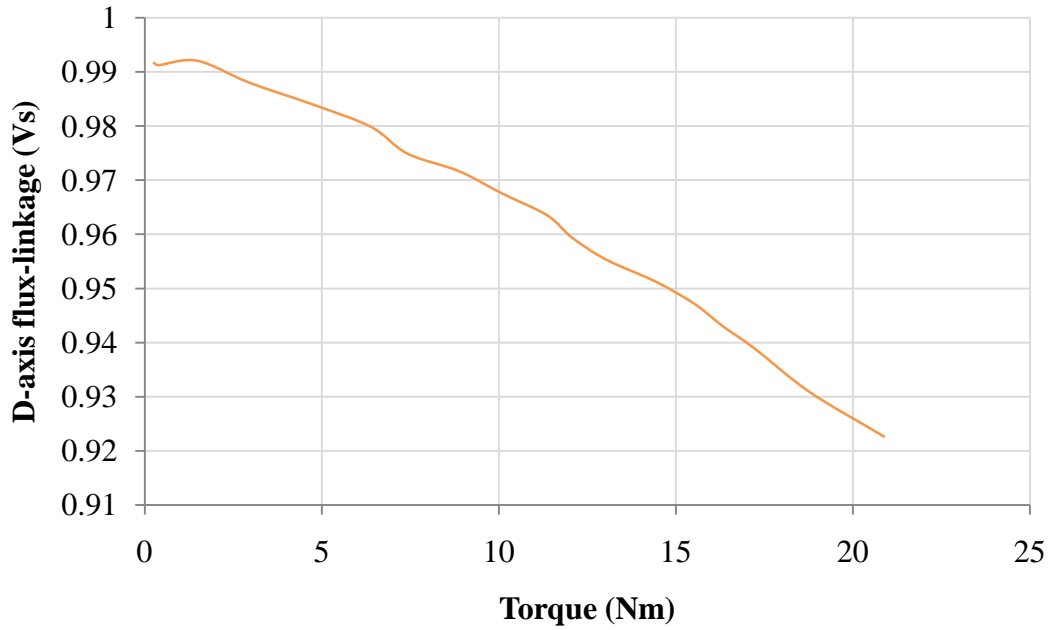
Fig. 5.2.3 Flux linkage decrease in the d-axis for voltage-fed RSM

The current-fed RSM, on the other hand, seemed to produce a more constant flux linkage (Figure 5.2.4) which averaged at around 0.945Vs. This is because the stator current input parameter was selected according to the measured current produced by the RSM's sensorless vector drive, consequently having an influence on the overall calculated flux linkage.
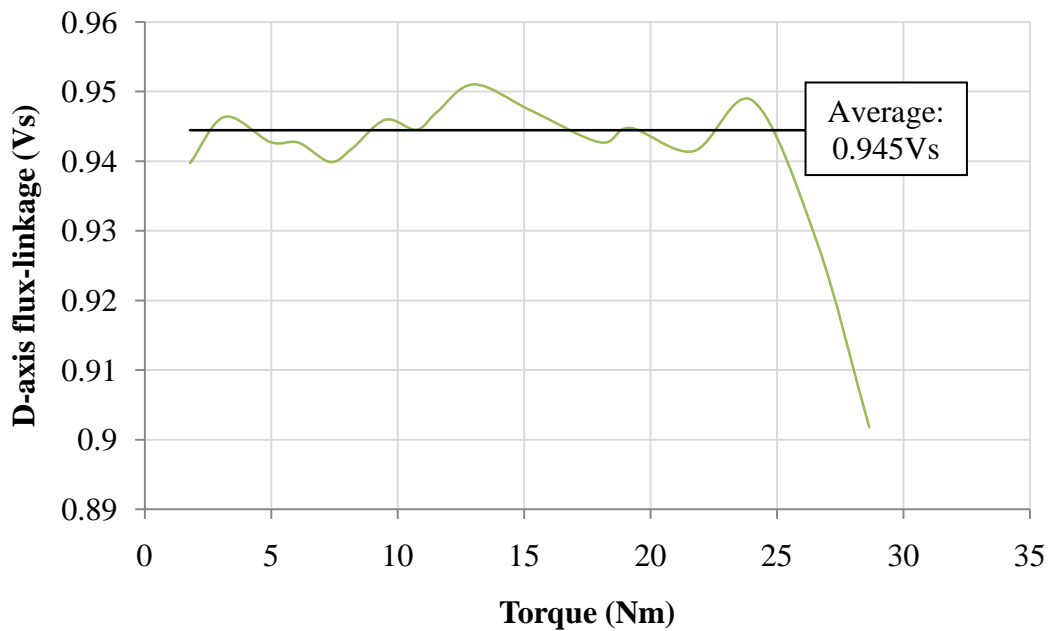
Fig. 5.2.4 Flux linkage decrease in the d-axis for current-fed RSM

5.3. Harmonics

As it is well known (Hart, 1988; Wagner, 1993) that drives produce a significant amount of harmonic distortion, this does not necessitate further investigation. However, the harmonic distortion produced by the RSM geometry is of interest. Since sinusoidal voltages and currents are used to drive the RSM, it is necessary to obtain the voltage harmonics produced by the current-fed RSM, and the current harmonics produced by the voltage-fed RSM. Figure 5.3.1 (a) and (b) are screenshots taken from the PQA which represent the line voltage and current, respectively, of the current-fed RSM at no-load. The PQA uses harmonic filters to find the fundamental voltage and displays it as a peak value.
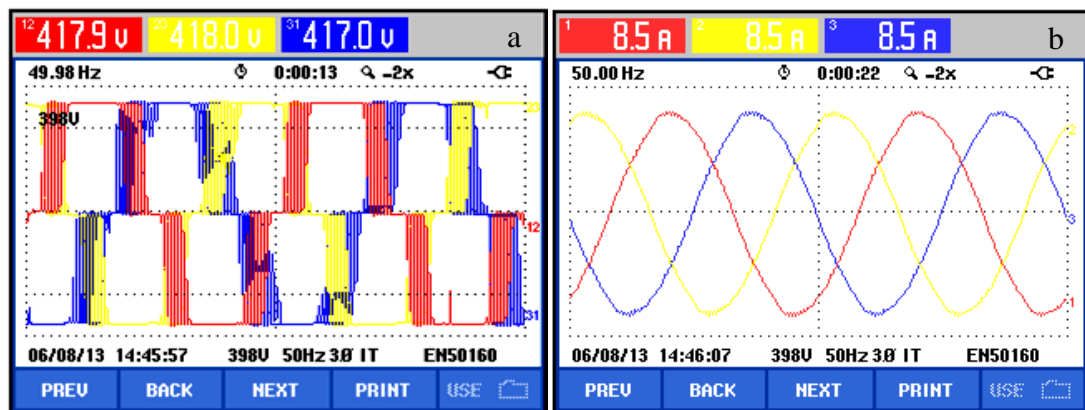
Fig. 5.3.1 Measured line-voltage (a) and -current (b) waveforms of current-fed RSM

In Figure 5.3.1 (a) it can be seen that the voltage distortion is created by the RSM drive. The phase voltage (Figure 5.3.2) taken from the FE software also contains a certain amount of harmonic distortion, but in this case it is a result of the non-sinusoidal flux linkage, which is caused by a combination of the flux linkage saturation as well as distortion in the slotted air gap. The fundamental component of the voltage waveform is calculated by using Fourier analysis.
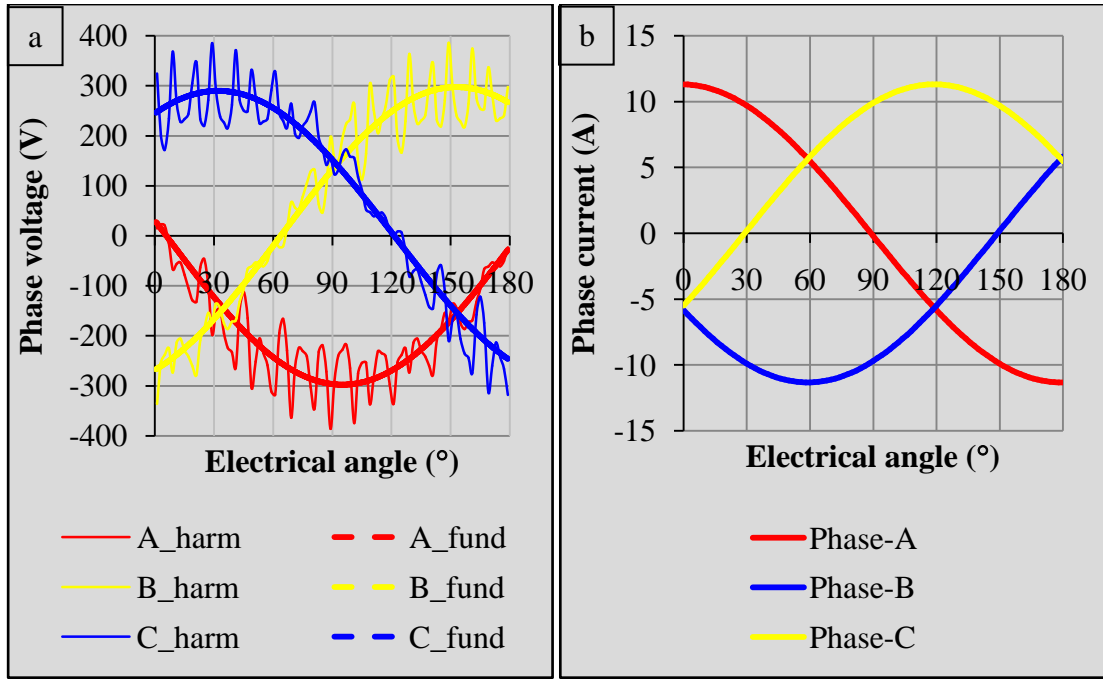
Fig. 5.3.2 Simulated voltage waveform (a) containing distorted and fundamental components and sinusoidal current waveforms (b) of current-fed RSM

By looking at the measured PWM voltage waveform in Figure 5.3.2, it is quite clear that a fair amount of voltage harmonic content is produced by the RSM drive. When the same RSM is simulated in FE, the voltage distortion tends to decrease. It can therefore be deduced that the voltage distortion is not only produced by the RSM drive, but is also partially produced by the rotor geometry. A similar result is found for the current produced by the voltage-fed RSM, and is further explained in the following section.

From the harmonic results found in the FE calculations, the odd harmonics are taken up to the 7th order as there are no even harmonics present and magnitude of harmonic orders higher than the 7th becomes negligible. Each harmonic order's percentage is related to the fundamental harmonic's rms value.

$$h_{\%} = \frac{|h_n|}{|h_1|} \cdot 100\% \qquad (5.3.1.1)$$

Where $h_{\%}$, h_n and h_1 is harmonic percentage, n^{th} harmonic, and fundamental harmonic respectively.

59

5.3.1. Current-fed voltage harmonics

Figure 5.3.1.1 represents the change in the voltage harmonic distortion, for the three harmonic orders, as the load is increased. Here the current-fed RSM produces a 3rd order harmonic distortion of 9.47% at full-load.
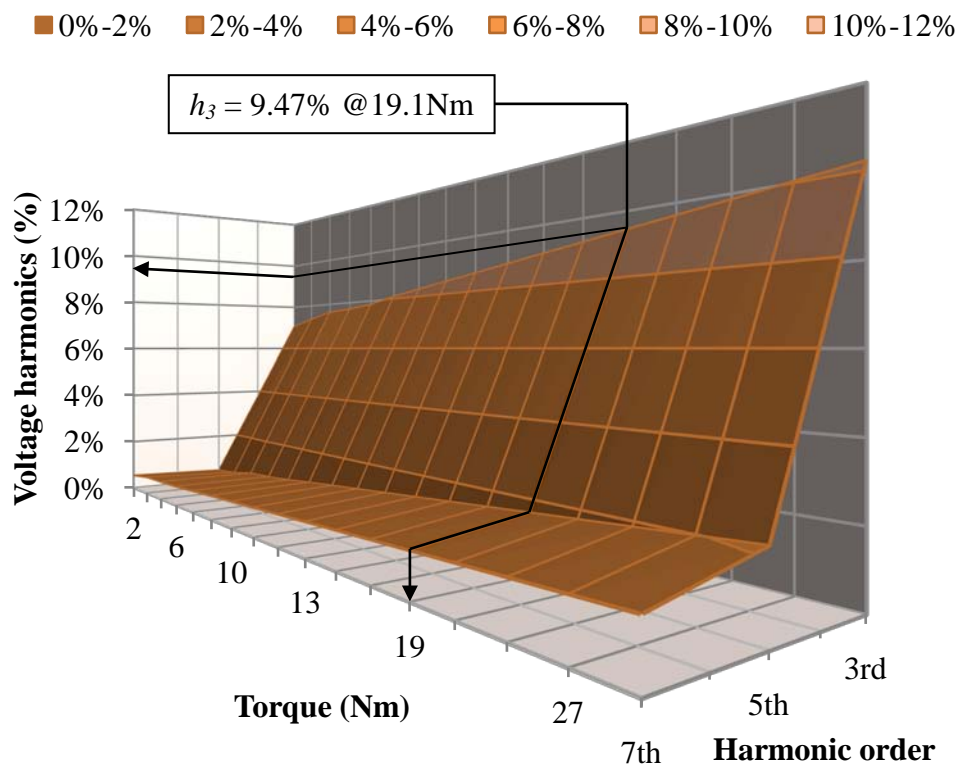
Fig. 5.3.1.1 Voltage harmonic spectrum for current-fed RSM vs. output torque

The voltage produced by the current-fed RSM is calculated according to eq. (2.1.1.1) where it can be seen that the voltage is shown to be related to the change in flux linkage. The voltage distortion in Figure 5.3.1.1 is therefore an indication of the flux linkage harmonic distortion as well.

5.3.2. Voltage-fed current harmonics

The current distortion produced by a sinusoidal voltage in the RSM can be seen in Figure 5.3.1.1 and produces just fewer than 6% current distortion for the 3rd harmonics.

60
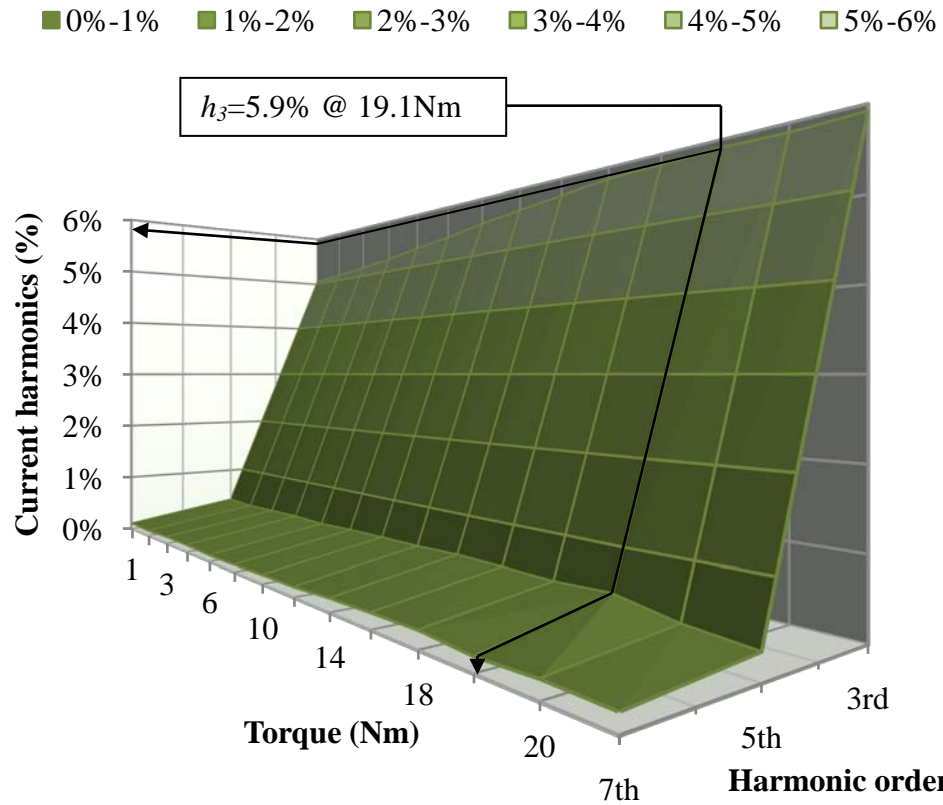
Fig. 5.3.2.1 Current harmonic spectrum for voltage-fed RSM vs. output torque

By simply comparing the amount of distortion in Figure 5.3.1.1 to that of Figure 5.3.1.2, it is clear that the current-fed RSM produces more harmonic distortion and can be seen in Table 5.3.2.1

Table 5.3.2.1 Summary of harmonic distortion at no-load and full-load

		$\frac{|h_3|}{|h_1|}$ %	$\frac{|h_5|}{|h_1|}$ %	$\frac{|h_7|}{|h_1|}$ %
Current harmonics (V-fed)	No-load	5.06%	0.39%	0.10%
	Full-load	**5.90%**	0.50%	0.17%
Voltage harmonics (C-fed)	No-load	7.06%	0.44%	0.54%
	Full-load	**9.47%**	1.67%	1.23%

5.4. Torque angle

With the flux linkages and currents known, it is now possible to determine the space phasor magnitude and angle for the flux linkage and current using their respective d- and q-axis values. Referring to Figure 2.1.2, the angular displacement between these two phasors (λ_s and I_s) indicates the torque angle γ. Although the voltage-fed RSM on the test bench reached its pull-out torque at around 22.5Nm, it was still possible to simulate it beyond this point in order to determine its behaviour. The torque angle is displayed (see Figure 5.4.1) as a function of the current angle, ranging from $0 - 90°$.
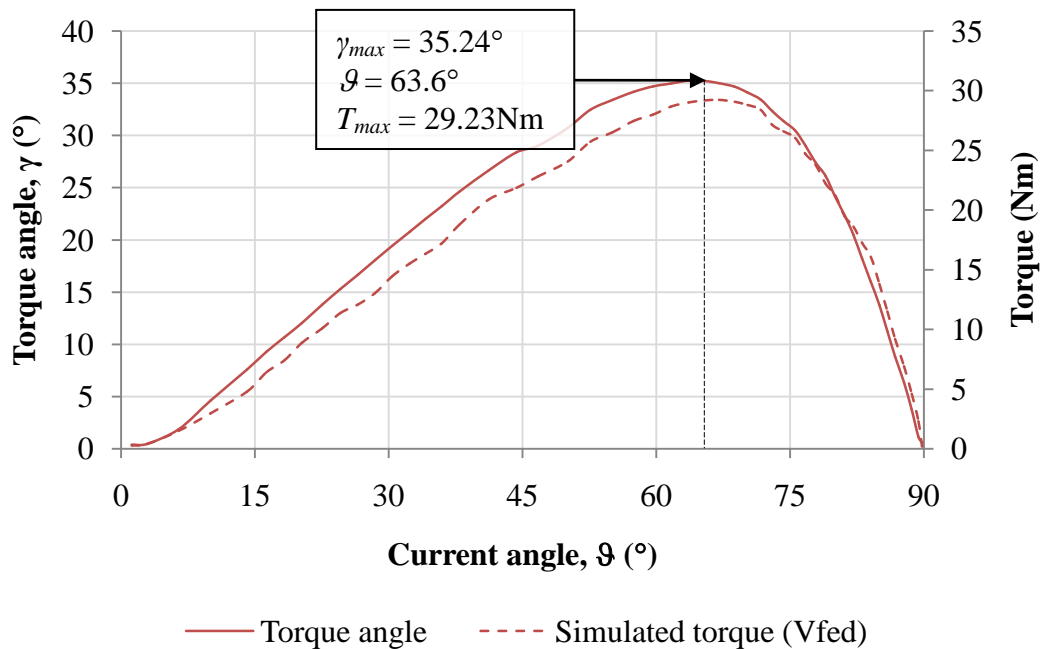
Fig. 5.4.1 Current angle vs. torque angle for voltage-fed RSM

According to the FE results in Figure 5.4.1, the pull-out torque is reached at a torque angle of 35.24°, resulting in a maximum torque of 29.23Nm, which is slightly higher than the measured results. It is therefore of interest to determine the pull-out torque in terms of its d- and q-axis inductance components.

5.5. Pull-out torque

The pull-out torque is the maximum amount of torque that a motor is capable of producing. When the motor's load exceeds that of the developed torque, the rotor

slips out of synchronism, but the reason for the voltage-fed RSM's low pull-out torque remains to be investigated. According to Honsinger (1971) the pull-out torque T_{po} is calculated according to (eq. 5.5.1)

$$T_{po} = \frac{mV_a^2 p}{4\omega^2 L_d}\left(\frac{L_d}{L_q} - 1\right)F_{po} \tag{5.5.1}$$

Where

m – number of phases,

V_a – a-phase rms voltage,

p – number of pole pairs,

ω – mechanical angular velocity (rad/sec), and

L_d, L_q – d- and q-axis inductance.

F_{po} is a factor that determines the pull-out torque as the frequency is changed. The frequency effectively changes the d- and q-axis reactance x_d and x_q while the total stator resistance r_a remains constant. In this study, however, a fixed frequency of 50Hz is maintained. By using these three constants, the pull-out torque factor is calculated according to eq. (5.5.2).

$$F_{po} = \frac{\sqrt{1+(r_a/x_d)^2}\cdot\sqrt{1+(r_a/x_q)^2} - (r_a/x_d)\cdot(x_d/x_q - 1)}{\left(1+(r_a/x_d)^2(x_d/x_q)\right)^2} \tag{5.5.2}$$

In this approach, Honsinger (1971) used rotor inductances that were analytically calculated from the geometry of the RSM while assuming a specific flux density. Since the results in this study contain a set of parameters over a range of loads, it would not provide adequate insight to select only one set of inductances to determine the pull-out torque. A pull-out torque is therefore calculated for the complete range of data used in Figure 5.5.1. Since the rotor inductances (and effectively the inductive reactances) change with respect to the applied load, the pull-out torque is calculated as a function of the current angle ϑ.

63
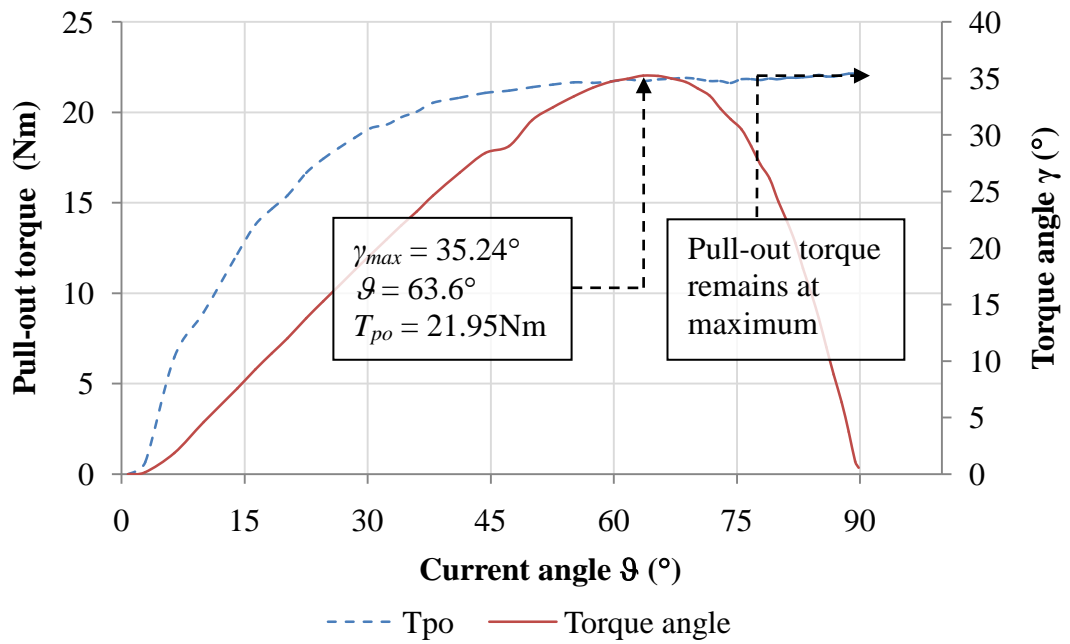
Fig. 5.5.1 Pull-out torque vs. current angle for voltage-fed RSM

According to eq. (5.5.1), the pull-out torque can be calculated over the whole range of current angles, where it remains reasonably constant as the applied load increases and γ decreases. It can be seen that, in this case, the pull-out torque reaches T_{po} at around 21.95Nm, after exceeding the maximum torque angle γ_{max} and are in closer agreement to the measured results. Since the d- and q-axis inductances are the only variables in eq. (5.5.1), it is necessary to analyse their behaviour as a function of the current angle.
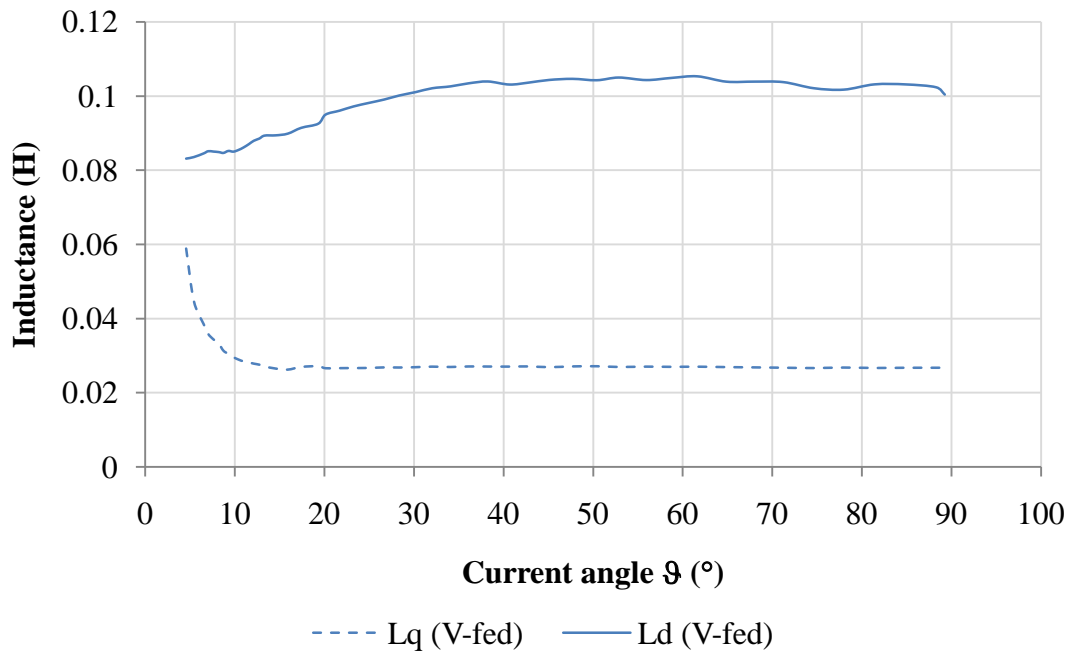
Fig. 5.5.2 D- and q-axis inductance vs. current angle

From Figure 5.5.2 it can be seen that the d-axis inductance reaches a maximum value at approximately 60° after which it starts to slowly decrease again, indicating the RSM's pull-out torque. Figure 5.5.2 also shows how the q-axis inductance reaches a constant value at approximately 20°. The highest value of the q-axis inductance L_q at $\vartheta = 10°$ indicates a higher amount of flux linkage λ_q for the current i_q. As i_q increases with ϑ, the amount of flux linkage decreases until the ratio between the flux linkage and current remains proportional. This is an indication of saturation in the q-axis. According to Rashad (2005), the saturation in the q-axis has the highest effect on the RSM's pull-out torque.

5.6. Core loss

As a final addition to the voltage-fed RSM's performance study, the core loss is investigated as a function of the load. To analyse this loss, it is broken up into its three main components, namely; eddy current (P_e), hysteresis (P_h) and excess loss (P_{ex}). Using the FE software, it is possible to determine an accurate method of obtaining the core loss by deriving it from the motor's flux density. The core loss measurements

(supplied by the datasheet in Appendix E) are given as a function of flux density and measured in W/kg as shown in Figure 5.6.1.
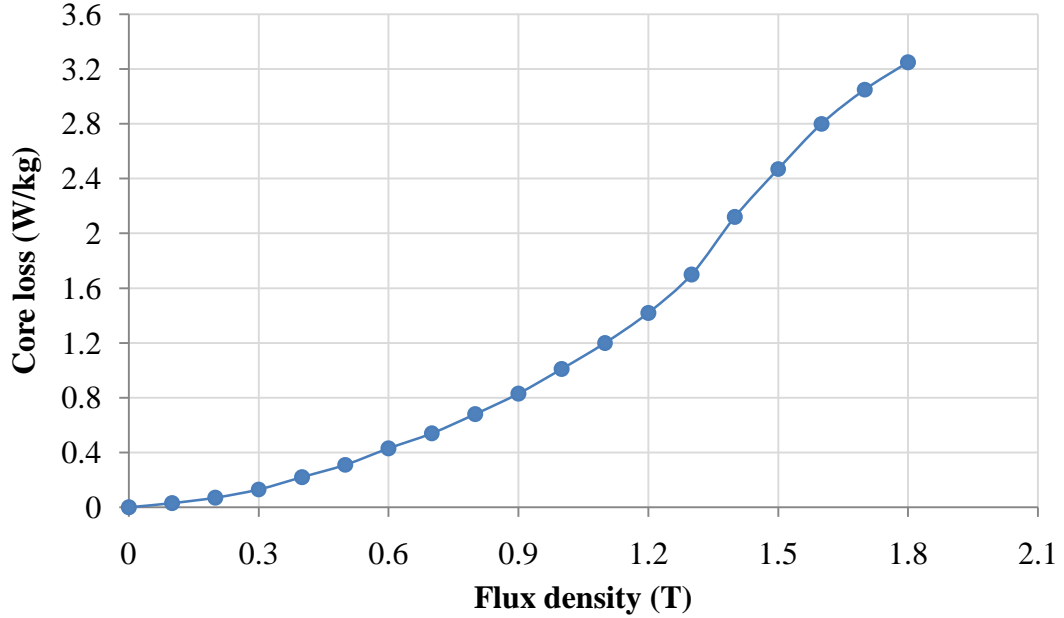
Fig. 5.6.1 Flux density vs. core loss measurements for M310-50A steel

The curve created from these data points can be expressed by a general equation (eq. 5.6.1) which describes the average total iron loss per cycle (Nie *et al.*, 2008).

$$P_c = P_h + P_e + P_{ex} \tag{5.6.1}$$

According to the separation model proposed by Bertotti (1988), these terms can now be written in terms of flux density and frequency,

$$P_c = a \cdot f \cdot B^x + b \cdot (f \cdot B)^2 + e \cdot (f \cdot B)^{1.5} \tag{5.6.2}$$

where *a*, *b* and *e* represent the hysteresis, eddy current, and excess coefficients and *x* is the Steinmetz coefficient (Akiror, 2012). These parameters are mathematically calculated by using a nonlinear regression analysis in which the parameters are continuously estimated until the error value ε (eq. 5.6.3) is at a minimum.

$$\varepsilon = \frac{1}{n} \sum_{i=1}^{n} \left(\frac{P_c - P_c^*}{P_c} \right)^2 \tag{5.6.3}$$

The minimum error ε was calculated using MATLAB, where P_c is the measured core loss and P_c^* is the estimated core loss for n amount of data points. A minimum error of 0.0079585 was found with the coefficients presented in Table 5.6.1.

Table 5.6.1 Core loss coefficients

a	*b*	*x*	*e*	*ε*
0.0124708	-0.000024765	2.02925	0.00146859	0.0079585

Applying these coefficients to eq. (5.6.2) results in a curve similar to that of the measured data (Figure 5.6.2).
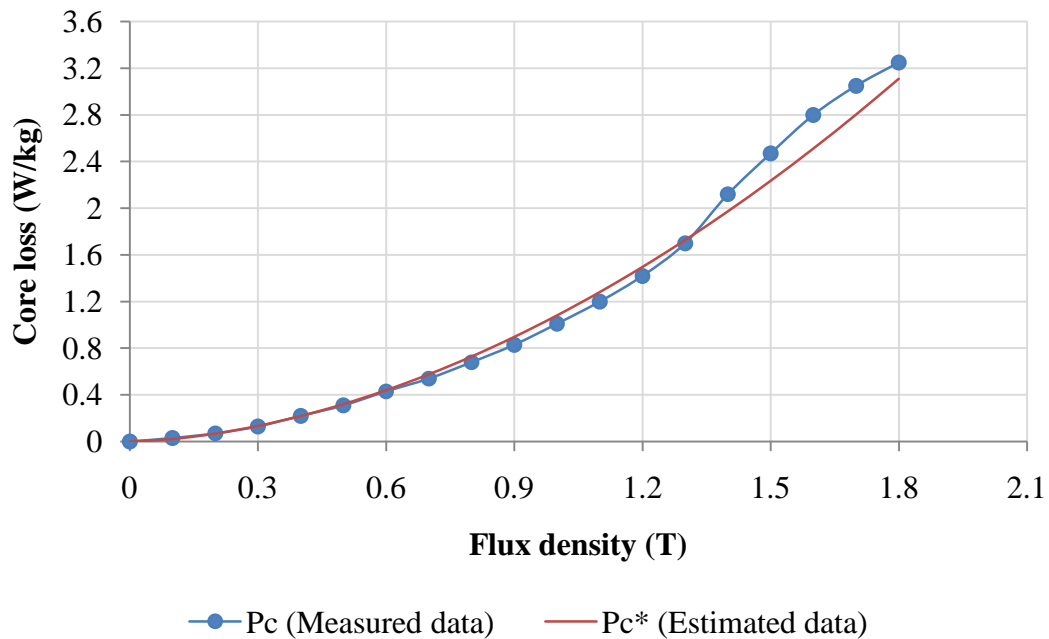
Fig. 5.6.2 Comparison of measured- and estimated core loss vs. flux density

It should be noted that this curve is not extrapolated in any way, but is merely used as a method of obtaining the coefficients for eq. (5.6.2). These calculated coefficients are then input into the FE software to find the core loss and, effectively, the three components of which it is made. The results from the FEM are shown in Figure 5.6.3.
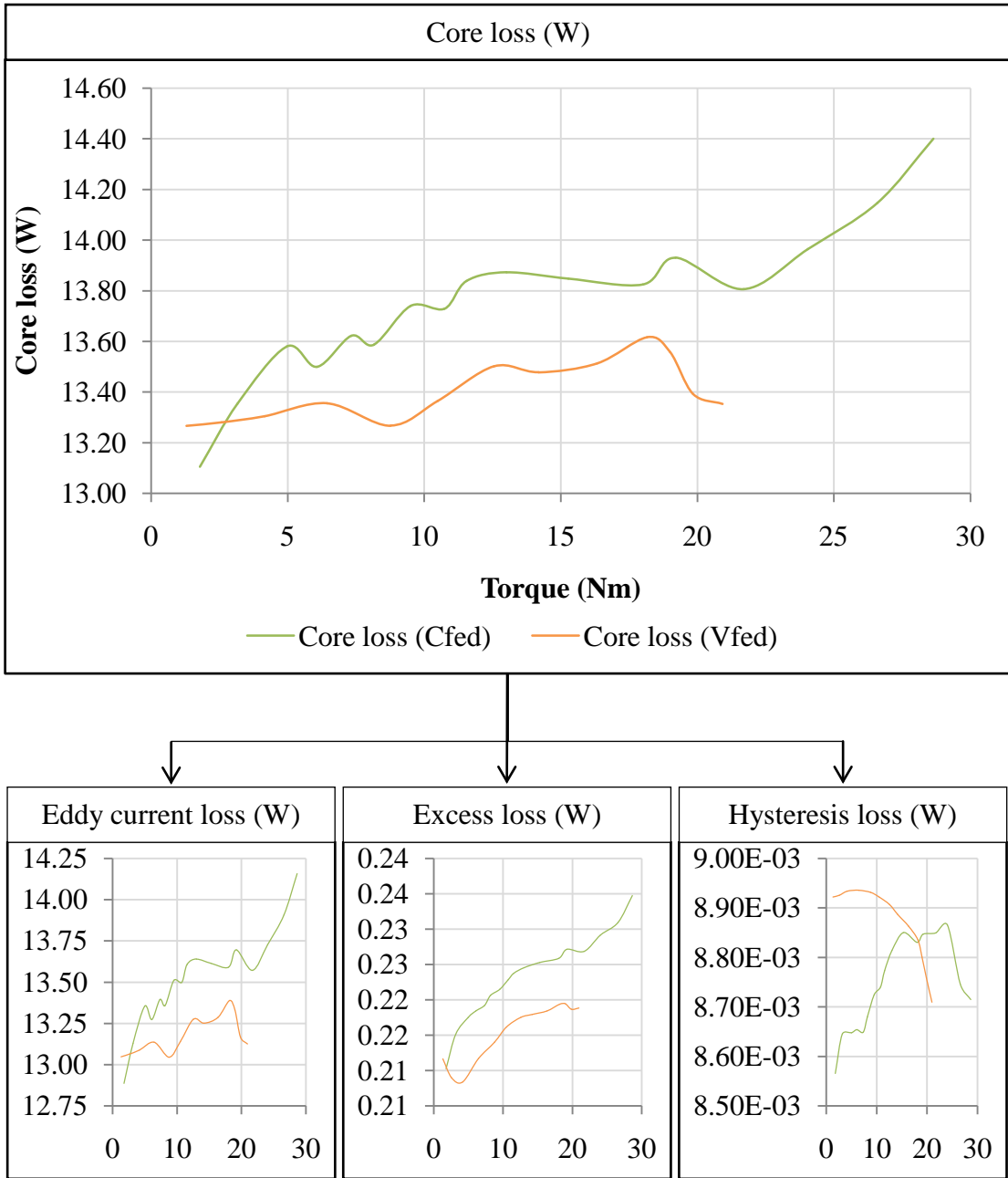
Fig. 5.6.3 Core loss and its three main components vs. output torque

The axis labels of the three smaller graphs in Figure 5.6.3 are removed due to their size, but still have the same x- and y-axes as the larger graph (representing the total core loss). From these results, it is clear that the current-fed RSM produces an overall higher core loss than the voltage-fed RSM. Although it does not make a big contribution to the total core loss, an exception is found in the hysteresis loss. Here, the voltage-fed RSM remains slightly higher for the majority of the load torque. It is also interesting to note how the hysteresis loss in the voltage-fed RSM decreases with

an increase in load in comparison with the rising hysteresis loss for the current-fed RSM. Furthermore, it can be seen that, for both motors, the losses due to eddy currents comprise the majority of the motor's core loss. At the full-load rated torque (19.1Nm), the eddy current loss makes up around 98% of the total core loss for both motors. Finally, the FE simulated core loss is in the range of 13 – 14.4W. These findings correlate well with the core loss measurements taken in Section 3.1.3, which amounted to 14.33W.

6. Summary, Conclusions and Recommendations

6.1. Summary

The objective of this thesis was to analyse the performance of a cageless, 4-pole RSM supplied by a sinusoidal voltage, in an effort to find the reason for its deficiency in industry. The intention was therefore to investigate the feasibility of this mode of operation and to endorse the likelihood of it becoming a practical alternative in certain related industrial applications. The performance of the voltage-fed RSM was therefore compared to a RSM being controlled by a sensorless vector drive, referred to as current-fed, due to the fact that it is simulated in FE by a sinusoidal current source.

6.1.1. Procedure summary

A test bench laboratory was setup and equipped with a 3kW RSM connected to a vector-controlled RSM drive, along with the option of switching the RSM over to the grid for a constant voltage supply. The RSM was coupled to a DC motor, controlled by a four-quadrant DC drive, which acted as a load to the RSM, as well as a synchronous start-up technique for the voltage-driven RSM. The electrical measurements were taken by a PQA including voltage, current, power and power-factor. The average torque and torque ripple were measured with a torque meter and the current angle was measured with an incremental encoder. These measurements were taken for increasing steps of load for the voltage- and current-fed RSM.

The measurements that were taken on the test bench were simulated in FE to conduct a deeper analysis of the RSM. In order to simulate the measured results as accurately as possible, certain electrical and mechanical parameters had to be determined by means of measurements and calculations. These parameters included the motor's inertia, stator resistance, end-winding leakage reactance, core loss and friction & windage loss. Through the use of FEA, these parameters resulted in the determination of the RSM's flux linkage, inductance, pull-out torque and core loss.

6.1.2. Results summary

After all the necessary parameters were measured, the next challenge was to validate the accuracy of the FE solution. The measured voltage, current, torque and efficiency were compared to the FE results and an average error of only 0.55% was found, thus providing the assurance that the remaining parameters to be calculated were within a reasonable accuracy range.

The measured and simulated parameters for both the voltage- and current-fed RSM were compared as a function of the load increase. Before the smaller differences are pointed out, it is important to first highlight the consistent differences that were found over the whole range of loads (0-150% P_{OUT}). Consistent differences are those that remain at a similar approximate difference relative to one another throughout the range of loads, whereas inconsistent differences are those that vary relative to each other as the load is increased.

6.1.2.1. Consistent differences

From the test bench measurements, it was found that only two consistent differences were picked up, namely, the supply voltage (Figure 4.3.1) and the efficiency (Figure 4.3.2). The RSM drive (current-fed) seemed to operate at a slightly higher PWM voltage, which might have had an influence on its overall efficiency. From the FE software, the only consistent difference was the harmonic content produced by the motor geometry. The harmonics were assessed in percentages relative to their fundamental component. Although the voltage harmonic (produced by the current-fed RSM) was compared to the current harmonic (produced by the voltage-fed RSM) it still remains a type of distortion. It can therefore be stated that the current-fed RSM consistently produces more harmonic distortion than the voltage-fed RSM.

6.1.2.2. Inconsistent differences

Following from this, the inconsistent differences are highlighted to show how the voltage-fed RSM reacts to the variety of loads. The first few relevant parameters are analysed, starting at a region between no-load and an applied load of around 3Nm. In this region, it was found that the voltage-fed RSM's torque ripple was slightly higher than that of the current-fed RSM (Figure 4.2.1). This torque ripple, however, soon decreases below that of the current-fed RSM as the load is further increased. In this

same initial region, the d-axis of the current-fed RSM has a 17.7% higher inductance than the voltage-fed RSM (Figure 5.2.2). This higher inductance consequently has an influence on the current-fed RSM's slightly superior efficiency. The voltage-fed RSM's power factor (Figure 4.3.2) also seems to have an influence on its efficiency as remains slightly higher than that of the current-fed RSM. Furthermore, it was found that the voltage-fed RSM produces a 1.4% higher core loss at no-load (figure 5.6.3). This difference, however, was only found for no-load conditions as the current-fed RSM's core loss immediately increased to a higher value than the voltage-fed RSM, as the load was increased. This core loss remains higher than the voltage-fed RSM's core loss for the remainder of the load increase. A similar observation was made after the core loss was split into its three components, with the exception found in the higher hysteresis loss for the voltage-fed RSM.

When increasing the load beyond 3Nm, the torque ripple found in the current-fed RSM's increases and remains at a higher value than the voltage-fed RSM for the majority of the loads (Figure 4.2.1). A further increase to 10Nm showed the current angle of the voltage-fed RSM to rise at a faster pace than the current-fed RSM, and remained roughly 5° higher throughout the load's increase (Figure 4.5.1). This causes the voltage-fed RSM's q-axis current to operate at a slightly higher value than that of the current-fed RSM. In addition, at a further 15Nm, the FE simulation shows the voltage-fed RSM's d-axis inductance to exceed that of the current-fed (Figure 5.2.2). At this same instant, the voltage-fed RSM's current-torque ratio seems to increase at a faster pace, while the current-fed RSM remains at a fairly consistent rate of current increase (Figure 4.3.1). The opposite reaction occurs for the voltage-fed RSM's power factor whereby its linear increase tends to reach a maximum value and remains fairly constant until pull-out (Figure 4.3.2).

The voltage-fed RSM finally reaches its pull-out torque at a load of 22.23Nm (Figure 4.1.2), which is only 16% above the rated output power, as compared to the current-fed RSM, which ran steadily up to 150% of the full-load output power (Figure 4.1.1). After a more in-depth FE investigation into the voltage-fed RSM, it was shown that the reason for this low pull-out torque is due to the d- and q-axis inductance's tendency to reach a maximum at $\vartheta = 63.3°$ (Figure 5.5.1). The saturation of the q-

axis inductance was also found to have an effect on the RSM's pull-out torque (Figure 5.5.2).

6.1.2.3. Core loss summary

As a final addition to the voltage-fed RSM's performance assessment, the core loss was simulated in FE, using the different values of flux density that are distributed throughout the RSM. The FE results proved that, for the majority of the loads, the current-fed RSM's core loss exceed that of the voltage-fed. These results were subsequently divided into their three main parts, namely the eddy current, hysteresis and excess losses. Of these three losses, the hysteresis loss is the only one that has different results to its counterparts. While the eddy current loss and excess loss increase with the load, the hysteresis loss for the voltage-fed RSM seems to decrease in relation to the increase from no-load to full-load. Furthermore, it was found that the core loss calculated by FE closely matches the core loss predicted by measurements.

6.1.2.4. Tabulated summary

The findings in this study presented the performance of the RSM as a function of the load. Providing a tabulated overview of each and every one of these results would turn into a cumbersome amount of data. A comprehensive overview is therefore provided, consisting of the main results at no-load (Table 6.1.1) as well as the rated full-load output power (Table 6.1.2).

Table 6.1.1 Summary of results at no-load

Parameter	Symbol	V-fed	C-fed	Unit
Linkage angle	δ	4.58	3.69	el°
Torque angle	γ	2.94	3.41	el°
Current angle	θ	7.52	7.1	el°
Average torque	T_{avg}	1.33	1.84	Nm
Torque ripple	$\%T_{rip}$	0.75	0.54	%
Voltage	V	386.92	417.69	V
Current	I	8.30	8.50	A
Input Power	P_{in}	639.67	614.94	W
Output Power	P_{out}	208.13	288.24	W

Parameter	Symbol	V-fed	C-fed	Unit
Efficiency	η	32.54	43.67	%
Power Factor	pf	0.115	0.10	no unit
3rd Voltage Harmonic	$\%Vh_3$	-	7.06	%
3rd Current Harmonic	$\%Ih_3$	5.06	-	%
Core Loss	P_c	13.27	13.10	W
Eddy Current Loss	P_e	13.05	12.89	W
Excess Loss	P_{ex}	211.63	210.23	mW
Hysteresis Loss	P_h	8.92	8.57	mW
D-axis inductance	L_d	68.64	83.46	mH
Q-axis inductance	L_q	48.62	40.04	mH

Table 6.1.2 Summary of results at full-load

Parameter	Symbol	V-fed	C-fed	Unit
Linkage angle	δ	15.92	11.98	el°
Torque angle	γ	21.84	22.9	el°
Current angle	θ	37.76	34.88	el°
Average torque	T_{avg}	19.31	19.75	Nm
Torque ripple	$\%T_{rip}$	0.26	0.3	%
Voltage	V	383.21	405.61	V
Current	I	11.93	10.90	A
Input Power	P_{in}	3642.00	3598.29	W
Output Power	P_{out}	3032.43	3102.33	W
Efficiency	η	83.26	85.84	%
Power Factor	PF	0.46	0.47	no unit
3rd Voltage Harmonic	$\%Vh_3$	-	9.47	%
3rd Current Harmonic	$\%Ih_3$	5.89	-	%
Core Loss	P_c	13.56	13.93	W
Eddy Current Loss	P_e	13.33	13.69	W
Excess Loss	P_{ex}	219.42	227.12	mW
Hysteresis Loss	P_h	8.80	8.85	mW
D-axis inductance	L_d	78.03	74.07	mH
Q-axis inductance	L_q	22.80	21.31	mH

6.2. Conclusions

The objective of this thesis was not only to study and compare the operation of a voltage- and current-fed RSM, but to model it as accurately as possible using a FEM. In order to accomplish this, two different FE models had to be created. The FE model for both the voltage- and current-fed RSM proved to be accurate to within 0.55%, making it possible to obtain a deeper investigation into the RSM. To conclude from these measured and simulated results, the following disadvantages were discovered for the voltage-fed RSM with regard to its performance characteristics.

- Low starting torque (requires cage or external/soft start),
- Low pull-out torque (Section 4.1),
- 4% Lower overall efficiency (Section 4.4),
- No speed control and
- No torque control

However, there are some advantages. These include:

- Cheaper operation (does not require a drive),
- Overall lower torque ripple,
- Lower voltage harmonic distortion and
- Lower core losses

From these results, it can be concluded that the disadvantages of the voltage-fed RSM outweigh the advantages, making the current-fed RSM the favourable alternative. However, despite the aforementioned conclusion, the results found in Figures 4.1.1, 4.3.2 and 4.4.1 clearly show that the torque, power factor and efficiency are quite compatible within the voltage-fed RSM's operating range, making the voltage-fed RSM a viable alternative to the current-fed RSM for fixed speed applications.

6.3. Recommendations

In industry today, RSMs and their drives are readily available and are used on a global scale. As previously mentioned, some of these drives are simply used to run the motor at a fixed speed for fans or pumps, making the variable speed drive redundant. This study has shown some advantages to alternatively using a voltage-fed RSM, but this has the added disadvantage of a low starting torque. Although a caged RSM is the most common choice for a voltage-fed operation, a few observations were made for the starting procedures when using a cageless rotor.

The starting procedure adapted in this study proved to be a reasonably simple task, but occasionally had a difficulty in synchronising. Since the RSM was manually switched onto the grid at synchronous speed, it was found that about ten percent of the starting attempts could not maintain synchronisation. This gives the impression that the RSM has the ability to self-align its poles relative to one another, but only to a certain extent. It was found that these types of RSMs usually require two basic conditions for starting; the relative alignment of the RSM's poles (d-axis and the a-phase) as well as a simple soft-starting or external starting technique to bring it up to synchronous speed. It is still necessary, however, to run the RSM slightly below its rated output power to ensure a stable range of operation. The presence of a caged rotor is the obvious solution to assist in the starting and synchronising of the RSM, but since the transient period is outside the scope of this study, it is unsure how this specific RSM would react to the alignment of the poles in order for it to synchronise. Jung and Nam (2006) stated that there are in fact challenges associated with the caged RSM's starting and synchronising procedure. These challenges include the starting torque ripple and negative torque. Their research focused on different number of rotor bars and shapes as a solution to this problem.

The presence of a possible rotor cage for this study could most likely have an even greater influence on the RSM's pull-out torque, increasing its feasibility as an alternative to the current-fed RSM. Ferraz and de Souza (2002) mention the importance of incorporating a caged rotor to assist in speed oscillations. When looking at the torque characteristics in IMs, it can be seen that the shape and size of the rotor bars affect the starting, rated and maximum torque. A significant amount of

research has been conducted on the shape and size of the rotor bars in an IM's squirrel cage. Moeller and Vaske (1976) presented the effect different rotor bars have on the IM's starting, rated and maximum torque (Figure 6.3.1).
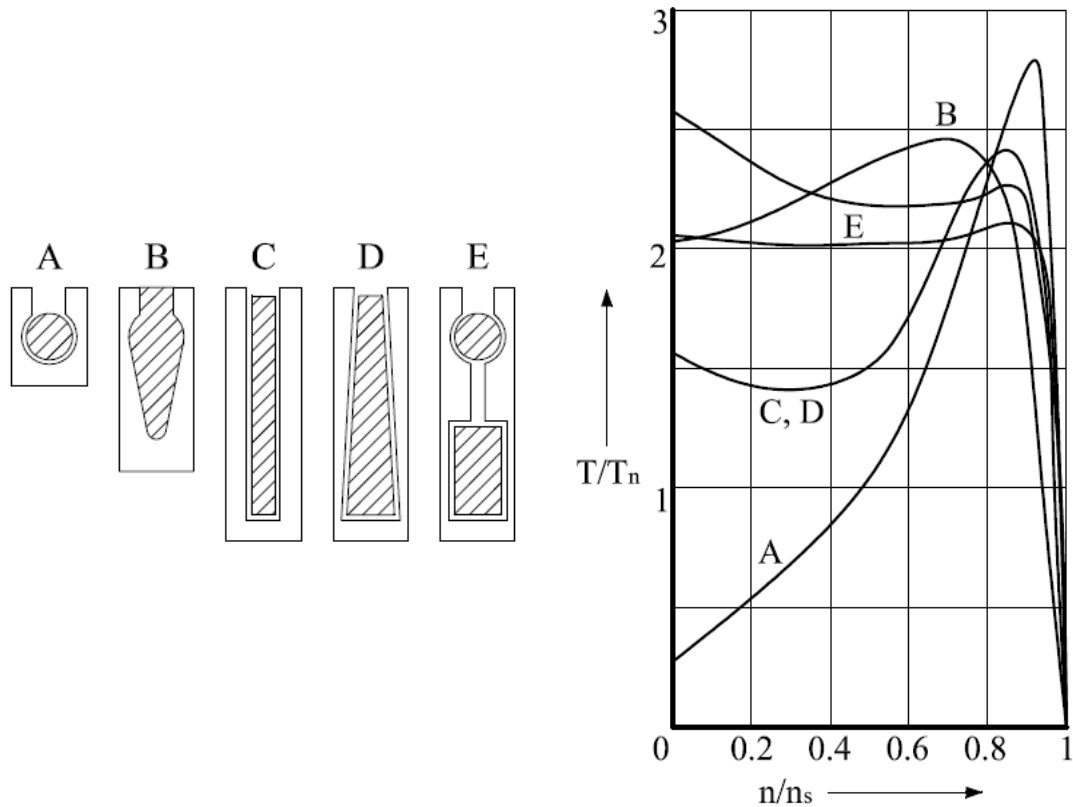
Fig. 6.3.1 Squirrel cage rotor bars and their respective torque-speed graphs

Theoretically, the only difference between an IM's squirrel cage rotor and a RSM's rotor cage are the flux barriers and cut-outs. They, like cage bar shapes, have an influence on the developed torque, inductance and depth of penetration of the magnetic field into the rotor. Since the voltage-fed RSM operates on the principle of reluctivity to produce its torque and the principle of inductance to maintain its stability, an interesting study could be performed on the combination of rotor bars, flux barriers and cut-outs to determine the effect it has on these parameters. By comparing a cageless RSM with a caged RSM, it could also be investigated to what degree a rotor cage might affect the stability of the RSM. Since copper and aluminium are the most widely used materials in electrical machines, a comparison could be made as to the machine's general behaviour with respect to these materials.

The flux barriers, according to Jung and Nam (2006), have a negative effect on the RSM's starting conditions when compared to an IM. An investigation into the RSM's flux barriers at the moment of pull-out and starting conditions could allow the engineer to redesign the flux barrier arrangement for optimum performance.

It is of the author's opinion that, although the voltage-fed RSM appears to be outdated technology, there are still numerous possibilities for its application in industry. The technology growth in RSMs is increasing by the day and is being utilised in various complex applications throughout industry. Some of these RSMs are used in an environment that requires less complicated tasks. The argument effectively leads towards the same ultimate goal – to reduce the complexities and expenses related towards a current-fed operation. Researchers and engineers are continuously attempting to solve problems by complicating solutions that could have been simplified. Complex electronic filter circuits in electrical machines, for instance, can be simplified by short-pitching the stator windings thus eliminating harmonic content. It is pointed out that electronics is not always needed and, to the author's opinion, a physical method is rather more elegant.

7. References

Akiror, J.C., 2012. *Model for Core Loss Prediction at High Frequency and High Flux Density*. Degree of Master of Applied Science. Montreal, Canada: Quebec Concordia University.

Alger, P.L., 1951. *The Nature of Polyphase Induction Machines*. New York: John Wiley and Sons Inc.

Aljaism, W., 2007. Switched Reluctance Motor Controller Design Using Novel Cam Positioner. *Power Conversion and Intelligent Motion Control Group*.

Badr, M.A., Hamouda, R.M. & Alolah, A.I., 1997. Synchronisation problem of high performance reluctance motors. In *IEE Proceedings - Electric Power Applications.*, 1997.

Bastos, J.P.A. & Sadowski, N., 2003. *Electromagnetic Modeling by Finite Element Methods*. 1st ed. CRC Press.

Bertotti, G., 1988. The Prediction of power losses in soft magnetic materials. *Journal de Physique*, 49(8), pp.1915-19.

Blondel, A.E., 1913. *Synchronous Motors and Converters: Theory and Methods of Calculation and Testing*. New York: McGraw-Hill.

Boglietti, A., 2008. Induction and synchronous reluctance motors comparison. In *IECON 2008. 34th Annual Conference of IEEE Industrial Electronics*. Orlando, FL, 2008. Politecnico di Torino.

Cogent Power, 2011. Typical data. In *Non oriented electrical steel*. Surahammar: Tata Group. p.14.

Crouse, C.H., 1951. A design method for polyphase reluctance synchronous motors. In *AIEE Trans., 70.*, 1951.

Cruickshank, A.J.O., Anderson, A.F. & Menzies, R.W., 1971. Stability of reluctance motors from freely accelerating torque speed curves. In *IEEE Trans. Power Apparatus and Systems.*, 1971.

Cruickshank, A.J.O., Anderson, A.F. & Menzies, R.W., 1971. Theory and performance of reluctance motors with axially laminated anisotrophic rotors. In *IEE Proc.*, 1971.

Douglas, J.F.H., 1956. The theory of anisotrophic field structures in synchronous machines. *AIEE Journal*, 75(1), pp.84-86.

Enache, E.A., Campeanu & S., A.a.E., 2009. Considerations regarding influences of reluctance synchronous motors parameters on the asynchronous starting. In *3rd International Symposium in Electrical Engineering and Energy Converters*. Suceava, 2009.

Faucher, J., Lajoie-Mazenc, M. & Chayegani, A., 1979. Characterization of a Closed-Loop Controlled Current-Fed Reluctance Machine Taking into Account Saturation. In *IEEE Trans. on Industry Applications*., 1979.

Ferraz, C.A.M.D. & de Souza, C.R., 2001. Measuring the parameters of a cage-rotor reluctance synchronous motor. In *Canadian Conference on Electrical and Computer Engineering*., 2001.

Ferraz, C.A.M.D. & de Souza, C.R., 2002. Reluctance synchronous motor asynchronous operation. In *Canadian Conference on Electrical and Computer Engineering*., 2002.

Guerdan, D.A., 1956. The Design of a Very-Slow-Speed Reluctance Motor forAtomic Reactor Rod Mechanism Drive. In *AIEE Summer and Pacific General Meeting*. San Fransisco, Calif., 1956. Westinghouse Electric corporation.

Gupta, J.D., 2011. *Theory and performance of electrical machines*. 14th ed. Delhi: S.K. Kataria & Sons.

Hanekom, A.N., 2006. *A torque ripple analysis on reluctance synchronous machines*. 1st ed. Cape Town, Western Cape, South Africa: Cape Peninsula University of Technology.

Hart, P.M., 1988. Harmonic modeling of synchronous machines. *IEE Proceedings*, 135(2), pp.52-58.

Heyns, G., 2011. *Analysis of harmonic field effects in reluctance synchronous machines*. MTech Thesis. Cape Town: Cape Peninsula University of Technology.

Hoft, R.G., 1968. Liapunov stability analysis of reluctance motors. In *IEEE Trans. Power Apparatus and Systems*., 1968.

Hoft, R.G., 1983. Power Electronics: Historical Review, Present Status and Future Prospects. In *IPEC*. Tokyo, 1983.

Honsinger, V.B., 1959. Theory of end-winding leakage reactance. *IEEE Transactions*, 90(1), pp.417-26.

Honsinger, V.B., 1971. Steady-state performance of reluctance machines. *IEEE Transactions on Power Apparatus and Systems*, 90(1), pp.305-17.

Honsinger, V.B., 1971. The inductances Ld and Lq of reluctance machines. In *IEEE Transactions on Power Apparatus and Systems*., 1971.

Hwang, S., 1994. Design techniques for reduction of reluctance torque in brushless permanent magnet motors. *IEEE Transactions on Magnetics*, 30(8), pp.4287-89.

IEEE Power Engineering Society, 2004. *IEEE Standard Test Procedure for Polyphase Induction Motors and Generators*. 1122004th ed. New York: IEEE Power Engineering Society.

Jezek, G., 2006. *History Of Magnets*. [Online] Available at: http://www.howmagnetswork.com/history.html [Accessed June 2011].

Jung, T.K. & Nam, H., 2006. Rotor Design to Improve Starting Performance of the Line-start Synchronous Reluctance Motor. *Journal of Electrical Engineering & Technology*, 1(3), pp.320-26.

Kamper, M.J., 1996. *Design Optimization of Cageless Flux Barrier Rotor Reluctance Synchronous Machine*. PhD Thesis. Stellenbosch: University of Stellenbosch.

Kanijo, M.K. & Mohanty, A.K., 1968. Stability of reluctance synchronous motor. In *IEEE trans. Power Apparatus and Systems*., 1968.

Kim, K.C. & Ryu, D.S., 2012. Torque characteristic with respect to the load angle of a permanent magnet motor. In *IEEE Transactions on Magnetics*. South Korea, 2012.

Kostko, J.K., 1923. Polyphase reaction synchronous motors. *AIEE Journal*, 42, pp.1162-2268.

Kostko, J.K., 1923. Polyphase Reaction Synchronous Motors. *AIEE Journal*, pp.1162-68.

Krause, P.C., 1968. Methods of stabilising a reluctance synchronous machine. In *IEEE Trans. Power Apparatus and Systems, 87.*, 1968.

Krause, P.C. & Lipo, T.A., 1969. Analysis and Simplified Representations of Rectifier-Inverter Reluctance-Synchronous Motor Drives. In *IEEE Transactions on Power apparatus and Systems*., 1969.

Lawrenson, P.J., 1961. Magnetic Field of the End-Windings of Turbo Generators. In *Proc IEE 108A.*, 1961.

Lawrenson, P.J. & Agu, L.A., 1963. A new unexcited synchronous machine. In *IEE Proc. 110, (7).*, 1963.

Lawrenson, P.J. & Agu, L.A., 1964. Low inertia reluctance machines. In *IEE Proc.*, 1964.

Lawrenson, P.J. & Agu, L.A., 1964. Theory and Performance of Polyphase Machines. In *IEE Proc., 111 (8).*, 1964.

Lawrenson, P.J. & Bowes, S.R., 1971. Stability of reluctance machines. In *Proc. IEE, 118*. London, 1971.

Lawrenson, P.J. & Gupta, S.K., 1967. Developments in the Performance and Theory of segementa- rotor reluctance motors. In *IEE Proc. 114 (5).*, 1967.

Lawrenson, P.J. & Mathur, R.M., 1972. Asynchronous performance of reluctance machines allowing for irregular distributions of rotor conductors. In *Proceedings of the Institution of Electrical Engineers*., 1972.

Lin, C.Y., 1951. Characteristics of Reluctance Machines. *AIEE Journal*, 70(2), pp.1971-77.

Lin, C.Y., 1951. Characteristics of Reluctance Machines. *AIEE Journal*, pp.1971-77.

Lin, C.Y., 1952. Equivalent circuits of reluctance machine. In *Trans. AIEE Power Apparatus and Systems, 71 (1).*, 1952.

Lipo, T.A. & Krause, P.C., 1967. Stability analysis of a reluctance-synchronous machine. In *IEEE Trans. Power Apparatus and Systems.*, 1967.

Liwschitz, M., 1961. *Alternating Current Machines*. D. van Nostrand Co Inc.

Louw, G., 2010. *Experimental determination of the moment of inertia of electrical machines*. BTech Thesis. Cape Town: Cape Peninsula University of Technology.

M&M Electronics, 2012. Drive Panel. Paarl: M&M Electronics. p.7.

Moeller, F. & Vaske, P., 1976. *Elektrische Maschinen und Umformer: Teil 1 Aufbau, Wirkungsweise und Betriebsverhalten*. 1st ed. Vieweg & Teubner Verlag 12.

Motorelli Electric Motors, n.d. *Performance and Dimensional Data for Cast Iron Electric Motor Range*. Cape Town: Motorelli.

Nakata, Y. & Takahashi, N., 1982. Direct Finite Element Analysis of Flux and Current Distributions under Specified Conditions. In *IEEE Trans. Magnetics, vol 18:2.*, 1982.

Nam, H. *et al.*, 2004. Design to improve starting performance of line-start synchronous reluctance motor for household appliances. In *Industry Applications Conference 39th IAS Annual Meeting.*, 2004.

Nie, Y., Hu, Q. & Huang, Y., 2008. The Measurement and Prediction of Iron Loss Under Nonsinusoidal Voltage Waveform with Arbitrary Frequency. In Engineering, S.o.E., ed. *International Conference on Electrical Machines and Systems*. Nanjing, 2008. Southeast University.

Nie, Y., Hu, Q. & Huang, Y., 2008. The measurement and prediction of iron loss under voltage waveform with arbitrary frequency. In Eng, S.o.E., ed. *International Conference on Electrical Machines and Systems*. Wuhan, 2008. ICEMS.

Parasiliti, F., 1995. Optimisation analysis of synchronous reluctance motor design. *Electrical Machine and Drives*, 11-13 September. pp.276-80.

Preston, T.W., Timothy, M.A. & Sitzia, A.M., 2001. 3-Dimensional Evaluation of the End-Parameters of Large Solid Salient Pole Synchronous Machines. *ALSTOM Research and Technology Centre, UK*.

Rashad, E.E.M., 2005. Stability Limits of Saturated Interior Permanent Magnet Motors. In *International Conference on Power Electronics and Drives Systems*. Kuala Lumpur, 2005. Dept. of Electr. Technol., Buraydah Coll. of Technol.

Ray, W.F. *et al*., 1986. High-Performance Switched Reluctance Brushless Drives. In *IEEE Trans. on Industry Applications, vol IA-22*., 1986.

Reece, A.B.J. & Pramanick, A., 1965. Calculation of the End-Region of A.C. Machines. In *Proc IEE 112 No. 7*., 1965.

Rockwell Automation, 2012. Control Block Diagrams. In *Powerflex 755*. Rockwell Automation Publication. p.351.

Schuisky, W., 1960. *Beregnung Elektrischer Maschinen*. Wien Springer-Verlag.

Skvarenina, T.L., 2001. *The Power Electronics Handbook*. West Lafayette, Indiana, USA: CRC Press.

Smith, R.A., 2010. Torque ripple analysis of a raluctance synchronous machine using magnetic wedges. In Voss, E., ed. *14th Annual BTech Conference*. Cape Town, 2010. Cape Peninsula University of Technology.

Soong, W.L., 2008. BH Curve and Iron Loss Measurements for Magnetic Materials. In *Power Engineering Briefing Note Series*. University of Adelaide, Australia, 2008.

Talaat, M.E., 1951. Steady-state and transient synthesis of 3-phase reluctance motors. *AIEE Journal*, 70(2), pp.1963-70.

Talaat, M.E., 1951. Steady-state and Transient Synthesis of 3-phase reluctance motors. *AIEE Journal*, pp.1963-70.

Thompson, S.P., 1902. *Dynamo Electric Machinery*. New York: M. Strong.

Trickey, P.H., 1933. The non-excited synchronous motor. *Electric Journal*, pp.169-62.

Trickey, P.H., 1946. Performance calculation on polyphase reluctance motor. *AIEE Journal*, 65, pp.191-93.

Trickey, P.H., 1946. Performance Calculations on Polyphase reluctance motors. *AIEE Journal*, pp.191-93.

Umenei, A.E., Access Bus. Group, F.I.A.M.U., Melikhov, Y. & Jiles, D.C., 2011. Models for Extrapolation of Magnetization Data on Magnetic Cores to High Fields. *IEEE Transactions on Magnetics*, 47(12), pp.4707 - 4711.

Vasudevan, K., Rao, G.S. & Rao, P.S., 2012. *National Program on Technology Enhanced Learning*. [Online] (1) Available at: http://nptel.iitm.ac.in/courses/IIT-MADRAS/Electrical_Machines_II/pdf/2_6.pdf [Accessed 17 June 2011].

Wagner, W.E., 1993. Effects of harmonics on equipment. *IEEE Transactions on Power Delivery*, 8(2), pp.672-78.

Wakileh, G.J., 2003. Harmonics on rotating machines. *Electric Power Systems Research*, 66, pp.31-37.

Williamson, S., Flack, T.J. & Volschenk, A.F., 1995. Representation of skew in time-stepped two-dimensional finite-element models of electrical machines. In *IEEE Transactions on Industry Applications*., 1995.

Williamson, S. & Mueller, M.A., 1990. Induction Motor End-Winding Leakage Reactance Calculation using the Biot Savart Method, Taking Rotor Currents Into Account. In *Proc Int. Conf. Elec Machines*. Cambridge, 1990.

Yano *et al*, M., 1983. History of Power Electronics for Motor Drives in Japan. In *IPEC*. Tokyo, 1983.

Zhang, J., 2005. *Eliminating the switched position sensor in a switched reluctance motor drive actuator application*. 1st ed. Lexington, Kentucky, USA: University of Kentucky.

8. Appendices

Appendix A: Vector potentials in FE

One of the simplest forms of a FE solution involves first-order triangular elements in a two-dimensional field. These elements are sub-divided into triangular shapes across a specified region, with the points defining these shapes known as nodes.

Using complex mathematical equations programmed into the software, FE starts the simulation by approximating certain parameters, and as a result, determines the consequential values via a Newton-Raphson iterative method. The vector potentials are distributed over the interrelated elements to form continuous values across inter-elemental boundaries.
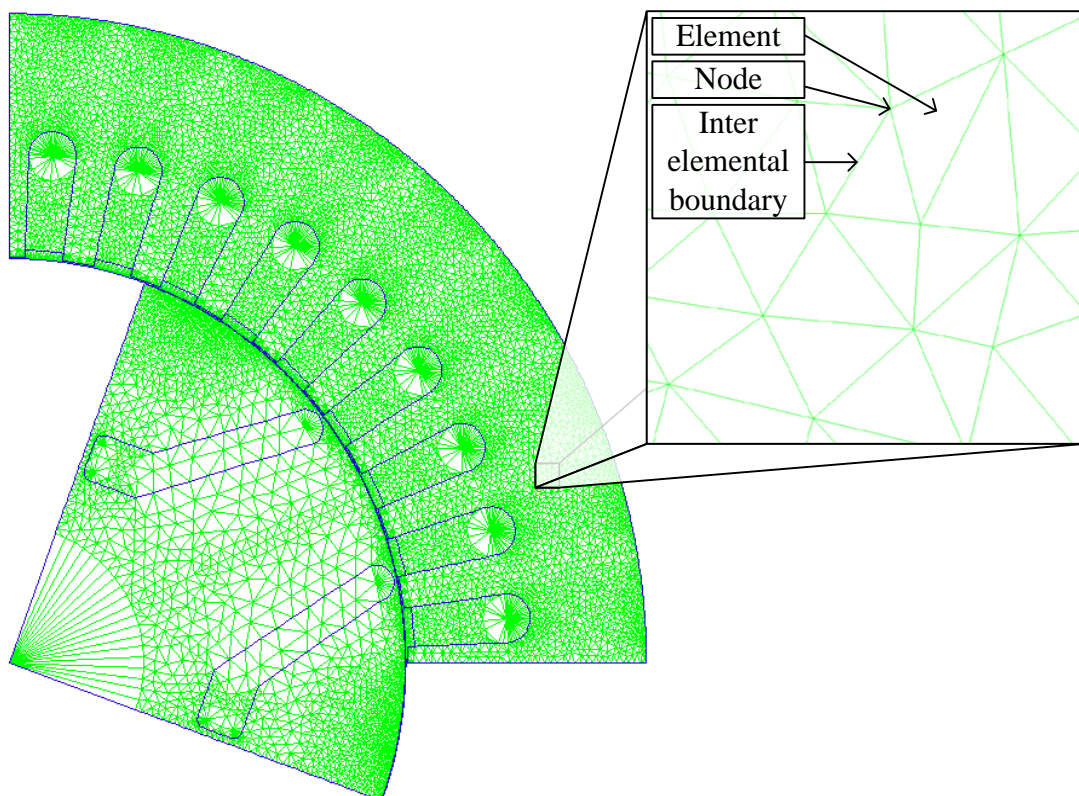
Fig. A.1 Representation of RSM with elements and nodes in FE

The nodal points on an element are expressed in the planar form and are functions of the x- and y-plane. The potentials between these nodal points vary linearly, giving it

the property of a first order element. The flux density and permeability inside each element remains constant.
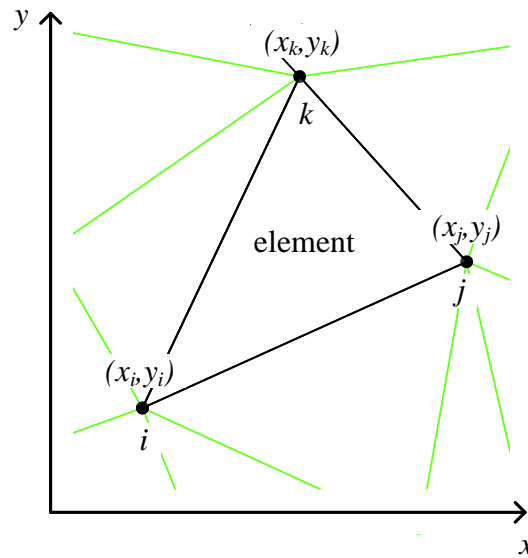
Fig. A.2 Elements and nodes in a Cartesian coordinate system

The expansion of the vector potential on the three individual nodes can be seen in eq. (A.1)

$$
\begin{aligned}
\bar{A}_i &= C_1 + C_2 x_i + C_3 y_i \\
\bar{A}_j &= C_1 + C_2 x_j + C_3 y_j \\
\bar{A}_k &= C_1 + C_2 x_k + C_3 y_k
\end{aligned}
\tag{A.1}
$$

The three unknowns, C_1, C_2, and C_3, are now solved in terms of geometry and potentials by using Kramer's rule:

$$
C_1 = \frac{\begin{vmatrix} \bar{A}_i & x_i & y_i \\ \bar{A}_j & x_j & y_j \\ \bar{A}_k & x_k & y_k \end{vmatrix}}{2\Delta} \qquad
C_2 = \frac{\begin{vmatrix} 1 & \bar{A}_i & y_i \\ 1 & \bar{A}_j & y_j \\ 1 & \bar{A}_k & y_k \end{vmatrix}}{2\Delta} \qquad
C_3 = \frac{\begin{vmatrix} 1 & x_i & \bar{A}_i \\ 1 & x_j & \bar{A}_j \\ 1 & x_k & \bar{A}_k \end{vmatrix}}{2\Delta}
\tag{A.2}
$$

Where Δ is the area of one element. The vector potential at any point on an element can now be calculated as

86

$$\vec{A} = N_i \vec{A}_i + N_j \vec{A}_j + N_k \vec{A}_k \tag{A.3}$$

where the coefficients, also known as shape functions, are defined as

$$
\begin{aligned}
N_i &= x_j y_k - x_k y_j + x\left(y_j - y_k\right) + y\left(x_k - x_j\right) \\
N_j &= x_k y_i - x_i y_k + x\left(y_k - y_i\right) + y\left(x_i - x_k\right) \\
N_k &= x_i y_j - x_j y_i + x\left(y_i - y_j\right) + y\left(x_j - x_i\right)
\end{aligned} \tag{A.4}
$$

As mentioned in Section 2.2, the vector potential $\vec{A}$ in this study is represented in a 2D Cartesian coordinate system where $\vec{A}$ is a vector in the z-plane ($\vec{A} = \vec{A}_x$). The flux linkage (per unit depth) is defined as the difference between two of these vector potentials. The closed path of a magnetic flux linkage λ_m can therefore be applied to Stoke's theorem to obtain

$$\lambda_m = \oint \vec{A}_z \cdot dl \tag{A.5}$$

The total flux linkage produced by the winding of a motor is calculated using the difference in the weighted average vector potential of the two sides of the winding. The average vector potential in a slot is calculated by

$$\vec{A}_{avg} = \left[\left(\sum_{m=1}^{M} \frac{\Delta_m}{\vec{a}_s} \frac{1}{3} \sum_{i=1}^{3} r_{mi} \vec{A}_{mi} \right) \middle/ \sum_{m=1}^{M} \Delta_m \right] \tag{A.6}$$

Where:

M	– Number of elements in one slot
m	– Element number
Δ_m	– Area of element
$\vec{a}_s$	– Area of slot
i	– Node number
r_{mi}	– Radius from centre of shaft to node i at element m
$\vec{A}_{mi}$	– Vector potential of node i at element m

Cast Iron Motors
Performance data
4 Pole – 1500 rpm synchronous speed 50Hz

| Motor type	Output (kW)	Full load speed (rpm)	INL 400V (A)	IFL 380V (A)	IFL 400V (A)	IFL 415V (A)	IST/IFL	Efficiency 100% FL	75% FL	50% FL	Power factor 100% FL	75% FL	50% FL	Full load torque (Nm)	TST/TFL	TPU/TFL	TM/TFL	M of I J (kgm²)	Noise level 1m dB(A)	Net weight (kg)
1L80I-4	0.55	1405	1.0	1.63	1.46	1.40	4.0	72.7	72.2	70.2	0.75	0.67	0.55	3.7	2.5	2.2	2.8	0.002	54	15
1L802-4	0.75	1415	1.3	2.07	1.96	1.89	4.5	72.6	72.3	70.5	0.76	0.66	0.56	5.1	2.3	2.1	2.7	0.002	59	16
1L90S-4	1.1	1406	1.6	2.73	2.60	2.50	4.2	76.5	76.1	74.9	0.80	0.69	0.56	7.5	2.4	2.2	3.2	0.0021	60	22
1L90L-4	1.5	1410	2.0	3.64	3.46	3.33	4.6	79.2	78.8	77.1	0.70	0.71	0.58	10.2	2.5	2.3	2.4	0.003	58	25
1L100L1-4	2.2	1400	2.5	4.97	4.72	4.55	5.2	81.1	80.6	79.7	0.83	0.73	0.6	14.9	2.6	2.0	3.0	0.007	62	33
1L100L2-4	3	1415	3.2	6.69	6.36	6.13	5.6	83.0	82.6	81.2	0.82	0.76	0.64	20.2	2.4	2.1	3.0	0.007	68	37
1L112M-4	4	1435	4.1	8.57	8.15	7.85	5.8	84.4	83.9	81.8	0.84	0.77	0.68	26.6	2.8	2.3	3.2	0.0095	70	43
1L132S-4	5.5	1455	4.3	11.6	11.0	10.6	6.5	86.6	86.1	84.8	0.83	0.77	0.68	36.1	2.2	2.1	3.1	0.0214	66	70
1L132M1-4	7.5	1448	5.0	15.1	14.3	13.0	6.8	87.9	87.3	85.3	0.86	0.81	0.72	49.5	2.6	2.3	3.2	0.0296	66	75
1L132M2-4	11	1451	7.7	21.9	20.8	20.0	6.1	88.0	88.4	87.0	0.86	0.81	0.73	72.4	2.3	2.0	2.9	0.075	70	87
1L160M-4	11	1460	7.9	22.3	21.2	20.4	6.8	89.1	88.1	87.1	0.84	0.82	0.76	72.0	2.5	2.0	2.9	0.075	69	123
1L160L-4	15	1462	11.0	29.7	28.2	27.2	7.2	90.5	89.3	88.0	0.85	0.82	0.75	98.0	2.5	2.1	3.2	0.092	68	144
1L180M-4	18.5	1466	12.0	35.4	33.6	32.4	6.9	90.3	89.7	88.2	0.88	0.84	0.74	120.6	2.2	2.0	3.0	0.130	72	182
1L180L-4	22	1472	15.0	41.6	39.5	38.1	6.9	91.3	90.8	88.6	0.88	0.85	0.76	142.8	2.3	1.9	3.3	0.158	74	190
1L200L-4	30	1475	17.0	55.6	52.8	50.0	6.3	92.1	91.5	88.8	0.89	0.86	0.81	194.3	2.2	1.8	2.9	0.262	77	270
1L225S-4	37	1480	23.0	68.3	64.9	62.6	7.2	92.4	91.8	90.0	0.89	0.87	0.78	238.0	2.5	1.6	2.8	0.406	80	318
1L225M-4	45	1472	26.0	82.8	78.7	75.9	6.5	92.7	92.1	90.0	0.89	0.86	0.8	292.1	2.3	1.8	3.2	0.469	80	351
1L250M1-4	55	1479	31.0	102	97.0	93.5	6.3	93.0	92.3	90.1	0.88	0.85	0.79	355.3	2.4	1.9	2.9	0.60	81	468
1L250M2-4	75	1479	34.0	136	129	124	6.2	94.1	93.8	91.9	0.89	0.85	0.83	484.5	2.2	1.8	3.2	0.86	80	554
1L280S-4	75	1485	35.6	135	128	124	5.8	93.7	93.2	91.5	0.90	0.89	0.85	482.6	2.2	1.8	3.1	1.12	83	562
1L280M1-4	90	1486	40.0	163	155	149	6.2	94.2	93.0	91.7	0.89	0.88	0.82	578.7	2.3	1.7	3.2	1.46	83	667
1L280M2-4	110	1478	51.2	196	186	179	6.2	94.8	94.3	92.2	0.90	0.88	0.83	711.1	2.5	2.3	2.0	2.68	82	750
1L315S-4	110	1483	52.5	197	187	180	5.8	95.3	94.6	92.6	0.89	0.89	0.87	708.7	2.2	1.8	2.8	3.11	85	1000
1L315M-4	132	1487	63.5	238	226	218	6.6	95.6	94.9	93.6	0.88	0.88	0.83	848.2	1.9	1.7	3.2	3.29	90	1100
1L315L1-4	160	1491	70.0	285	271	262	6.4	95.6	95.0	93.9	0.89	0.86	0.81	1025.4	2.3	1.8	3.2	3.79	89	1160
1L315L2-4	200	1488	86.0	356	338	326	5.6	95.8	95.0	94.0	0.89	0.87	0.78	1284.3	2.2	1.8	2.8	4.49	87	1270
1L355M-4	250	1485	102	432	410	395	6.1	95.5	94.7	93.2	0.90	0.89	0.87	1608.6	2.4	1.8	2.9	5.67	90	1698
1L355L-4	315	1489	115	544	517	498	5.9	95.6	95.5	94.3	0.92	0.89	0.87	2021.4	2.2	1.6	3.3	6.60	93	1848
1L355L2-4	365	1490	135	620	589	568	7	95.7	95.6	94.5	0.92	0.89	0.87	2275	2.4	1.8	2.6	7.50	95	2150

INL = no load current   IFL = full load current   IST = locked rotor current   TST = locked rotor torque   TPU = pull up torque   TM = maximum torque   TFL = full load torque
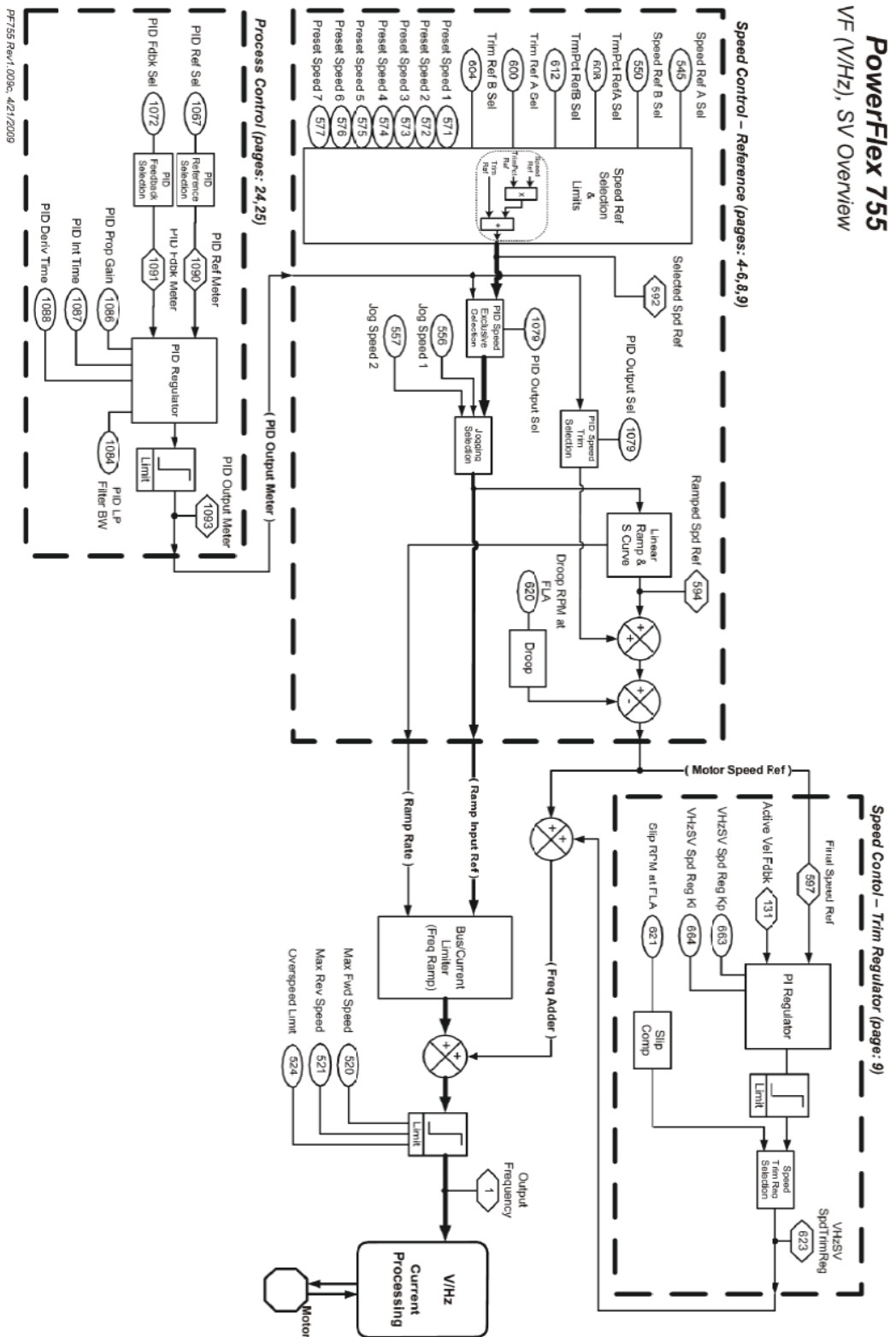
Appendix C: Test bench configuration (M&M Electronics, 2012)

C.1   Test bench schematic diagram
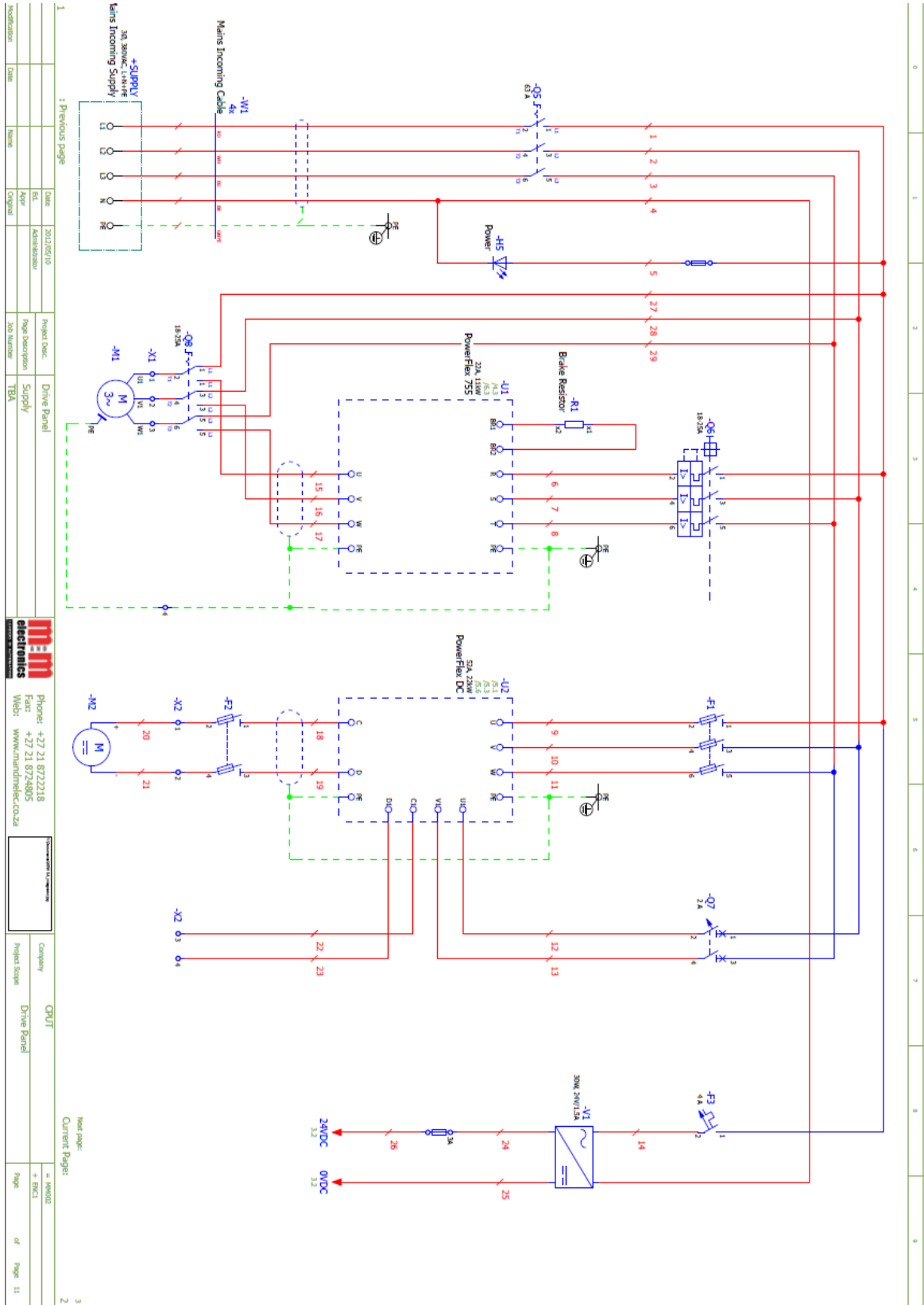
C.2 RSM sensorless vector drive block diagram (Rockwell Automation, 2012)

Appendix D: RSM lamination steel data (Cogent Power, 2011)

Typical data for SURA® M310-50A

T	W/kg at 50 Hz	VA/kg at 50 Hz	A/m at 50 Hz	W/kg at 100 Hz	W/kg at 200 Hz	W/kg at 400 Hz	W/kg at 1000 Hz	W/kg at 2500 Hz
0,1	0,03	0,07	33,3	0,05	0,12	0,34	1,62	6,31
0,2	0,08	0,19	43,9	0,20	0,50	1,36	5,63	21,8
0,3	0,17	0,33	51,2	0,40	1,04	2,83	11,5	45,9
0,4	0,27	0,50	57,7	0,66	1,73	4,75	19,5	80,2
0,5	0,40	0,69	64,2	0,97	2,56	7,14	29,7	128
0,6	0,53	0,91	71,2	1,32	3,54	10,0	42,6	193
0,7	0,68	1,16	79,1	1,72	4,67	13,5	58,4	279
0,8	0,85	1,45	88,4	2,16	5,96	17,5	77,8	390
0,9	1,03	1,79	100	2,65	7,42	22,1	101	526
1,0	1,23	2,21	116	3,19	9,07	27,4	130	695
1,1	1,45	2,75	139	3,78	10,9	33,6	163	
1,2	1,71	3,50	175	4,44	13,0	40,7		
1,3	2,00	4,80	251	5,22	15,3	48,6		
1,4	2,40	8,14	470	6,17	18,0	58,0		
1,5	2,83	20,4	1230	7,31	21,1	68,5		
1,6	3,25	55,7	3070					
1,7	3,57	125	6150					
1,8	3,86	239	10700					

Loss at 1.5 T , 50 Hz, W/kg	2,83
Loss at 1.0 T , 50 Hz, W/kg	1,23
Anisotropy of loss, %	10
Magnetic polarization at 50 Hz	
H = 2500 A/m, T	1,57
H = 5000 A/m, T	1,66
H = 10000 A/m, T	1,79
Coercivity (DC), A/m	40
Relative permeability at 1.5 T	970
Resistivity, µΩcm	52
Yield strength, N/mm²	385
Tensile strength, N/mm²	500
Young's modulus, RD, N/mm²	185 000
Young's modulus, TD, N/mm²	200 000
Hardness HV5 (VPN)	190

RD represents the rolling direction
TD represents the transverse direction
Values for yield strength (0.2 % proof strength)
and tensile strength are given for the rolling direction
Values for the transverse direction are approximately 5% higher

cogent
Surahammars Bruks AB

14

Appendix E: Law of Approach to Saturation

The extrapolation of *B-H* data is required to correctly simulate any magnetic material used in FE software. This condition has been set into place by the FE software designers in cases where the flux density might exceed 2T. This process makes use of values, usually taken from a material's datasheet or by own measurement and are usually given up to around 1.8 – 2.0T. After this point it becomes increasingly challenging to generate the required magnetic field, consequently affecting the measurement accuracy. In this study, the *B-H* data for the RSM's material (M310-50A) is given up to a maximum flux density of 1.8T, and is displayed in Table E.1 with its corresponding curve in Figure E.1. Referring to the last data point, it can be seen that it has not yet fully approached saturation. With the help of the engineers from the FE software, the subsequent data points were extrapolated up to 3T.

Table E.1 *B-H* data for M310-50A steel

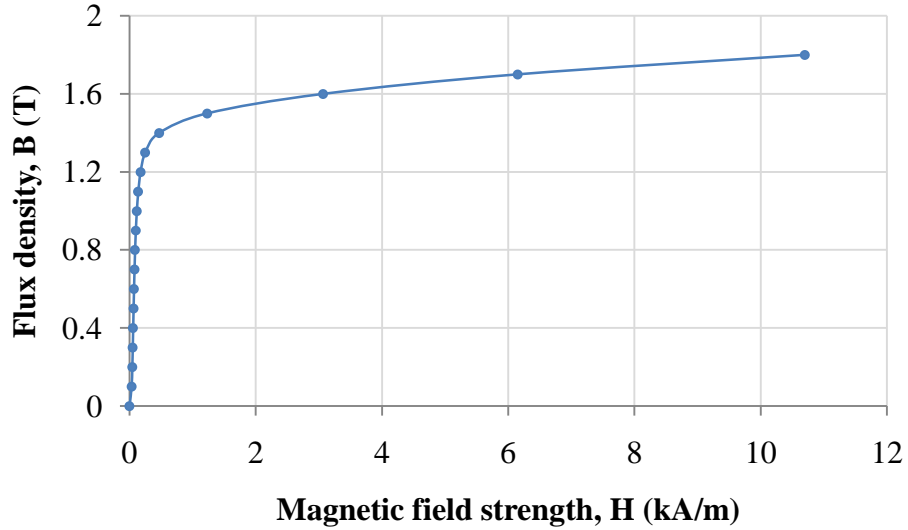| M310-50A	
B	H
0	0
0.1	33.3
0.2	43.9
0.3	51.2
0.4	57.5
0.5	64.2
0.6	71.2
0.7	79.1
0.8	88.4
0.9	100
1	116
1.1	139
1.2	175
1.3	251
1.4	470
1.5	1230
1.6	3070
1.7	6150
1.8	10700

Fig. E.1 *B-H* curve for M310-50A steel

According to Umenei, *et al.* (2011) a reliable technique of extrapolation was found to be a method called the Law of Approach to Saturation (LAS). Using eq. (E.1) and eq. (E.2),

$$B = \mu_0 \left(H + M_S - M_S \frac{b}{H^2} \right) \tag{E.1}$$

$$\frac{dB}{dH} = \mu_0 \left(1 + 2M_S \cdot \frac{b}{H^3} \right) \tag{E.2}$$

the LAS method continuously calculates each new data point by inserting the last data points of *B* and *H* into the equation, where M_S is the saturation magnetisation, μ_0 is the permeability of air, and *b* is a curve fitting coefficient. The extrapolated curve and data points are shown in Figure E.2.

Table E.2 Extrapolated *B-H* data for M310-50A steel

M310-50A (extrapolated)	
1.890407	33316
1.938272	71124
1.984912	127932
2.021316	165740
2.090644	231548

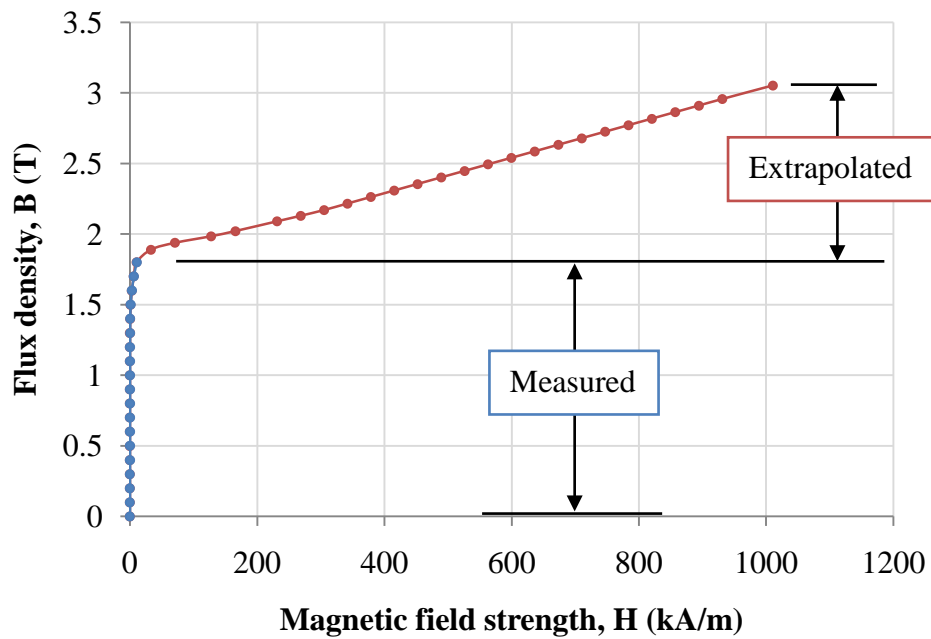|	
2.129539	268356
2.170219	305164
2.21649	341972
2.262756	378780
2.309018	415588
2.355279	452396
2.401538	489204
2.447796	526012
2.494053	562820
2.54031	599628
2.586566	636436
2.632822	673244
2.679078	710052
2.725334	746860
2.771589	783668
2.817844	820476
2.864099	857284
2.910354	894092
2.956609	930900
3.052864	1010477

Fig. E.2 *B-H* curve for M310-50A steel (extrapolated)